LUND UNIVERSITY

Model-Based Control of Gasoline Partially Premixed Combustion

Ingesson, Gabriel

2015

Document Version:
Publisher's PDF, also known as Version of record

Link to publication

Citation for published version (APA):
Ingesson, G. (2015). *Model-Based Control of Gasoline Partially Premixed Combustion*. [Licentiate Thesis, Department of Automatic Control]. Department of Automatic Control, Lund Institute of Technology, Lund University.

Total number of authors:
1

General rights
Unless other specific re-use rights are stated the following general rights apply:
Copyright and moral rights for the publications made accessible in the public portal are retained by the authors and/or other copyright owners and it is a condition of accessing publications that users recognise and abide by the legal requirements associated with these rights.
• Users may download and print one copy of any publication from the public portal for the purpose of private study or research.
• You may not further distribute the material or use it for any profit-making activity or commercial gain
• You may freely distribute the URL identifying the publication in the public portal

Read more about Creative commons licenses: https://creativecommons.org/licenses/

Take down policy
If you believe that this document breaches copyright please contact us providing details, and we will remove access to the work immediately and investigate your claim.

LUND UNIVERSITY

PO Box 117
221 00 Lund
+46 46-222 00 00

Model-Based Control of Gasoline Partially Premixed Combustion

Gabriel Ingesson

LUND
UNIVERSITY

Department of Automatic Control

Lic. Tech. Thesis
ISRN LUTFD2/TFRT--3268--SE
ISSN 0280–5316

Department of Automatic Control
Lund University
Box 118
SE-221 00 LUND
Sweden

© 2015 by Gabriel Ingesson. All rights reserved.
Printed in Sweden by Media-Tryck.
Lund 2015

Abstract

Partially Premixed Combustion (PPC) is an internal combustion engine concept that aims to yield low NO_x and soot emission levels together with high engine efficiency. PPC belongs to the class of low temperature combustion concepts where the ignition delay is prolonged in order to promote the air-fuel-mixture homogeneity in the combustion chamber at the start of combustion. A more homogeneous combustion process in combination with high exhaust-gas recirculation (EGR) ratios gives lower combustion temperatures and thus decreased NO_x and soot formation. The ignition delay is mainly controlled by temperature, gas-mixture composition, fuel type and fuel-injection timing. It has been shown that PPC run on gasoline fuel can provide sufficient ignition delays in conventional compression-ignition engines. The PPC concept differs from conventional direct-injection diesel combustion because of its increased sensitivity to intake conditions, its decreased combustion-phasing controllability and its high pressure-rise rates related to premixed combustion, this puts higher demands on the engine control system.

This thesis investigates model predictive control (MPC) of PPC with the use of in-cylinder pressure sensors. Online heat-release analysis is used for the detection of the combustion phasing and the ignition delay that function as combustion-feedback signals. It is shown that the heat-release analysis could be automatically calibrated using nonlinear estimation methods, the heat-release analysis is also a central part of a presented online pressure-prediction method which can be used for combustion-timing optimization.

Low-order autoignition models are studied and compared for the purpose of model-based control of the ignition-delay, the results show that simple mathematical models are sufficient when manipulating the intake-manifold conditions. The results also show that the relation between the injection timing and the ignition delay is not completely captured by these types of models when the injection timing is close to top-dead-center.

Simultaneous control of the ignition delay and the combustion phasing using a dual-path EGR system, thermal management and fuel injection timings is studied and a control design is presented and evaluated experimentally.

Closed-loop control of the pressure-rise rate using a pilot fuel injection is also studied and the multiple fuel-injection properties are characterized experimentally. Experiments show that the main-fuel injection controls the combustion timing and that the pilot-injection fuel could be used to decrease the main fuel injection ignition delay and thus the pressure-rise rate. The controllability of the pressure-rise rate was shown to be higher when the pilot injection was located close to the main-fuel injection. A pressure-rise-rate controller is presented and evaluated experimentally.

All experiments presented in this thesis were conducted on a Scania D13 production engine with a modified gas-exchange system, the fuel used was a mixture of 80 % gasoline and 20 % N-heptane (by volume).

Acknowledgments

I would like to thank my supervisor, Prof. Rolf Johansson, for his consistent guidance, for sharing his knowledge on scientific work, and for setting high standards in the project. My co-supervisor Prof. Per Tunestål has been very helpful with discussions and suggestions on theoretical and practical matters related to both combustion engines and control. Prof. Bo Bernhardsson is acknowledged for proofreading and improving the articles that this thesis was based on.

The major part of this work was done in collaboration with my colleague, Lianhao Yin. His knowledge about, and experience with laboratory work and programming made it possible for us to set up the test rig and do the experiments presented in the thesis. The technicians at the Division of Combustion Engines were helpful in keeping everything running and re-building the engine when necessary, special thanks go to Tomas Lindén, Mats Bengtsson and Tommy Petersen. Scania is acknowledged for supplying the engine used in this work, I am also grateful to Dr. Ola Stenlåås for taking a great interest in our project and for giving constructive feedback on our progress. This project was funded by KCFP, PPC Control (Swedish Energy Administration: Project no. 22485–1), the author is also a member of the LCCC Linnaeus Center and the eLLIIT Excellence Center at Lund University.

The Department of Automatic Control provides a great atmosphere, both socially and professionally, office 2112A has always been a place for interesting discussions. Finally, I would like to thank Desiré, my family and my friends for their encouragement and support.

Gabriel

Contents

1. Introduction and Motivation **9**
- 1.1 The Internal Combustion Engine . . . 9
- 1.2 The Demand for Cleaner Exhaust . . . 9
- 1.3 Low Temperature Combustion Concepts . . . 9
- 1.4 Control . . . 11
- 1.5 Outline of the Thesis . . . 12
- 1.6 Publications . . . 13
- 1.7 Other Publications . . . 13

2. Modeling for Control and Estimation **14**
- 2.1 Heat-Release Analysis . . . 14
- 2.2 Load Definitions . . . 17
- 2.3 Ignition Delay . . . 18
- 2.4 Gas System . . . 20
- 2.5 Model Validation . . . 21

3. Control and Estimation Methods **23**
- 3.1 Control . . . 23
- 3.2 State-Estimation Methods . . . 25

4. Experimental Setup **29**

5. Online Heat-Release-Model Calibration **32**
- 5.1 Introduction . . . 32
- 5.2 Problem Formulation . . . 33
- 5.3 Observability . . . 35
- 5.4 Filter Configuration . . . 35
- 5.5 Simulation Results . . . 36
- 5.6 Sensitivity to Model-Parameter Errors . . . 40
- 5.7 Experimental Results . . . 41
- 5.8 Summary . . . 43

6. Ignition-Delay Model Evaluation **46**
- 6.1 Introduction . . . 46

6.2 Ignition-Delay Experiments 47
6.3 Parameter Identification and Model Evaluation 48
6.4 Model-Evaluation Results 51
6.5 Linearization for Control Purposes 55
6.6 Discussion 57

7. Simultaneous Control of Ignition Delay and Combustion Phasing 59
7.1 Introduction 59
7.2 Modeling 59
7.3 MPC 62
7.4 Results 64
7.5 Discussion and Conclusions 70

8. Pressure Prediction and Efficiency Optimization using Heat-Release Analysis 74
8.1 Introduction 74
8.2 The Combustion-Timing Controller 75
8.3 Results 78
8.4 Discussion 89
8.5 Conclusions 91

9. Combustion Control Using Multiple Fuel Injections 92
9.1 Introduction 92
9.2 Experimental Characterization 94
9.3 Controller Design 105
9.4 Controller Evaluation 107
9.5 Discussion and Conclusions 109

10. Conclusions and Future Work 112
10.1 Conclusions 112
10.2 Future Work 112

Bibliography 114

1

Introduction and Motivation

1.1 The Internal Combustion Engine

Ever since the internal combustion engine was introduced during the later half of the 19th century it has been the most common source of power for vehicle propulsion by far. In 2010, the world's total vehicle population was estimated to be above 1 billion and with a mean vehicle-production rate of 75 million vehicles per year for the last 10 years, 2 billion vehicles is believed to be reached in the years to come [Sperling and Gordon, 2009; International Organization of Motor Vehicle Manufacturers, 2014]. While the internal combustion engine has been and is a cornerstone of modern civilization it is also an emitter of toxic emissions and greenhouse gases.

1.2 The Demand for Cleaner Exhaust

The emission legislations for vehicle internal combustion engines have become more and more stringent ever since [Haagen-Smit, 1952], linked the smog problems in the Los Angeles Basin to the air pollutions originating from the automotive combustion engines. The European NO_x and soot particles (PM) emission limits (Euro I-Euro VI) for heavy-duty engines during the past 20 years are presented in Fig. 1.1. In 2004, the transportation sector contributed to 13 % of the global greenhouse-gas emissions [IPCC, 2007] and in Europe, the goal is to reduce the CO_2 emission levels for passenger cars by 18 % by 2015 and 40 % by 2021 [EU, 2009]. The increasingly stringent emission regulations is today one of the main driving factors for internal combustion engine research.

1.3 Low Temperature Combustion Concepts

During the past decades, new advanced combustion concepts have been investigated in the search for lower emission levels and higher engine efficiency.

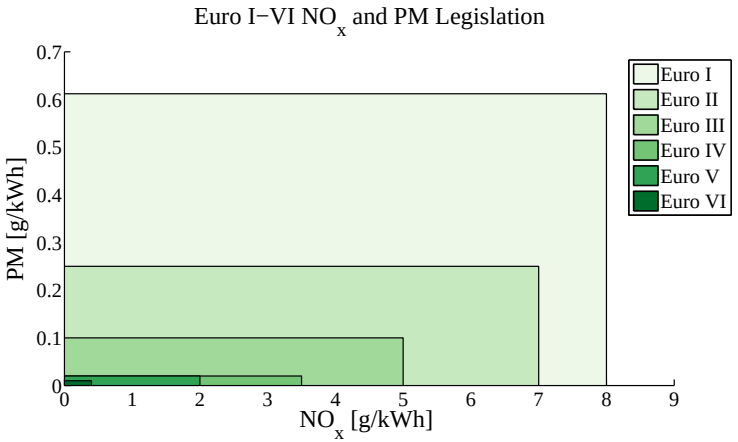

Figure 1.1 Euro I-VI emission legislation for heavy-duty engines [EU, 2007].

Low temperature combustion is a class of concepts which uses high ratios of exhaust-gas recirculation (EGR), early fuel-injection timings and fuels with higher octane numbers in order to prolong the auto-ignition reaction processes. This enhances fuel- and air mixing and gives more homogeneous mixtures before the start of combustion. Homogeneous combustion has less soot formation and since the cylinder mixture is diluted with EGR and is locally leaner, lower in-cylinder temperatures are obtained, yielding lower NO_x emission levels [Musculus, 2006] and reduced heat transfer to the cylinder walls [Fridriksson et al., 2001], which increases the thermodynamic efficiency.

Homogeneous charge compression ignition (HCCI) is a LTC concept where a diluted homogeneous charge is inducted and ignited by compression, it was first studied in two-stroke engines [Onishi et al., 1979; Ishibashi and Asai, 1979] and was later shown to yield low emission levels in combination with high efficiencies in the low-load operating regions of four-stroke engines [Epping et al., 2002]. A challenge with the HCCI concept is the combustion-timing sensitivity and controllability. Since the combustion event is mainly controlled by chemical autoignition kinetics, as opposed to the conventional spray-driven compression-ignition concept, the combustion timing could only be controlled by varying the temperature and mixture composition during the compression stroke. Therefore, alternative techniques for HCCI combustion-timing control are necessary, examples of such techniques are variable-valve timing [Agrell et al., 2003; Bengtsson et al., 2006c], variable compression ratio [Haraldsson et al., 2002] and dual-fuel operation [Olsson et al., 2001]. HCCI was also shown to have a limited operating range due to violent combustion rates at high-load operation [Olsson et al., 2004].

LTC can also be obtained by modifying the conventional direct-injection compression-ignition diesel-engine concept, for which the ignition delay could be prolonged by injecting the fuel earlier during the compression stroke when the cylinder mixture is cooler as investigated by [Takeda et al., 1995], or by injecting the fuel later during the expansion stroke [Kimura et al., 1999]. It was shown in [Akihama et al., 2001] that a high EGR ratio also could be a key component when prolonging the ignition delay. With direct fuel injection, the combustion timing is more easily controlled compared to HCCI if the ignition delay is sufficiently short. In [Noehre et al. 2006], difficulties related to obtaining sufficient ignition delay with diesel fuels at high-load conditions were investigated. The gasoline partially premixed combustion (PPC) concept was introduced by [Hildingsson, Kalghatgi et al., 2006], a concept where gasoline is directly injected into a compression-ignition engine. With the use of EGR ratios around 50 %, lean air-to-fuel ratios and pilot fuel injections that control the combustion rates, [Manente, 2010a] showed that it was possible to achieve gross indicated efficiencies between 52 and 55 % from idle to 26 bar gross indicated mean effective pressure while keeping NO_x emissions below 0.40 g/kWh with filter smoke numbers (FSN) below 0.30. As PPC lies somewhere in between HCCI and conventional compression-ignition combustion in terms of combustion controllability and homogeneity, hopefully, the best properties of these two concepts could be combined with PPC.

1.4 Control

Control theory is about making systems behave in a desired way, in the case of the internal combustion engine, this is about obtaining durable and reliable performance while fulfilling constraints on efficiency, pollutant and noise-emission levels at a price that is competitive for mass production. The low temperature combustion concepts have in common that they are more sensitive to temperature and mixture conditions compared to conventional compression-ignition engines, this puts higher demands upon engine controller design where the right conditions have to be set more accurately for satisfactorily performance.

The work presented in this thesis handles the uncertainty in PPC with the use of feedback. Control problems related to the gasoline partially premixed combustion concept, such as ignition-delay control, efficiency optimization and the assurance of acceptable pressure-rise rates are studied. The controllers presented all predict engine behavior based on model and sensor information in order to set the desired operating conditions. Model-based control has the benefit of incorporating a priori physical and/or data-based system knowledge in the controller design, if a component or quantity of the controlled system changes, a model-based controller can be adapted more easily. Models for control need to be compatible with the real-time constraints of the engine, the models studied

in the thesis are therefore of lower complexity compared to those used for engine simulation. The model-calibration procedures used for controller design are also presented in the thesis. Another defining feature of the work presented in this thesis is the use of in-cylinder pressure sensors and high computational power, something that is not available in the commercial vehicles of today, but might be available in the vehicles of tomorrow.

1.5 Outline of the Thesis

The thesis starts with two introductory chapters that introduce the used models, control principle and estimation methods. The research contributions are then presented in the following five chapters.

Chapter 2 presents the heat-release model used for in-cylinder pressure prediction and combustion-timing detection, low-order ignition-delay models and a simplistic model of the intake manifold and the gas-system stationary behavior.

The principles of model linearization and model predictive control are presented in Chapter 3, these principles are used together in the controller design in the following chapters. This chapter also introduces the estimation methods used for EGR-ratio estimation and on-line calibration of the heat-release model presented in Chapter 2.

Chapter 4 gives a description of the setup that was used in the experimental work. Engine specifications, sensors, actuators and control system layout are presented. In Chapter 5, an extended Kalman filter and a particle filter are used for on-line calibration of cylinder-wall temperature, the top-dead-center offset and a convective heat-transfer coefficient for accurate heat-release analysis. Evaluation results from simulation and experimental data are presented.

The three different ignition-delay models presented in Chapter 2 are evaluated in Chapter 6. Engine data are used to calibrate the models, and a comparison of model-prediction performance and computational complexity is presented together with the model-calibration procedure.

In Chapter 7, an ignition-delay model is used for model predictive control of the ignition delay and the combustion phasing using the actuators in the gas-exchange system and the fuel-injection system jointly.

A model-based single-injection pressure-prediction method is presented in Chapter 8, the method is also incorporated as a part of an optimal-control scheme. The prediction and controller performance are evaluated experimentally.

In Chapter 9, pressure-rise rate control using a pilot-fuel injection is studied. Experimental data with various pilot-fuel injection configurations are presented together with a suggested controller design which is also evaluated experimentally.

Finally, conclusions and future work are presented in Chapter 10.

1.6 Publications

The thesis is based on the following publications:

Ingesson, G., Yin, L., Johansson, R., and Tunestål, P. (2015). "Simultaneous Control of Combustion Timing and Ignition Delay in Multi-Cylinder Partially Premixed Combustion," SAE Int. J. Engines 8(5).

Ingesson, G., Yin, L., Johansson, R., and Tunestål, P. (2015). "A Model-Based Injection-Timing Strategy for Combustion-Timing Control," SAE Int. J. Engines 8(3).

Ingesson, G., Yin, L., Johansson, R., and Tunestål, P. (2016). "Automatic Calibration of a Heat-Release Model Using Nonlinear Estimation Methods", submitted to the SAE World Congress.

Ingesson, G., Yin, L., Johansson, R., and Tunestål, P. (2016). "A Double-Injection Control Strategy For Partially Premixed Combustion", submitted to the IFAC Symposium on Advances in Automotive Control, June 20-23, 2016, Kolmården, Sweden

Ingesson, G., Yin, L., Johansson, R., and Tunestål, P. (2016). "An Investigation on Ignition-Delay Modeling For Control", submitted to the International Journal of Powertrains.

1.7 Other Publications

Yin, L., Ingesson, G., Shamun, S., Tunestål, P. et al. (2015). "Sensitivity Analysis of Partially Premixed Combustion (PPC) for Control Purposes," SAE Technical Paper 2015-01-0884.

2

Modeling for Control and Estimation

Models that aim to capture the engine behavior are applied in this thesis both for controller design and for the estimation of unmeasured quantities such as combustion timing and ignition delay. These models are presented in this chapter. The model used for heat-release analysis is introduced in the first section, it was both used for estimating the ignition delay and the combustion phasing in Chapters 6-9 and for in-cylinder pressure prediction in Chapter 8. Automatic calibration of this model using nonlinear estimation is considered in Chapter 5. In the following sections the ignition-delay models that were calibrated and compared in Chapter 6 and used for control in Chapter 7 are presented together with the gas-system model that was used for control and estimation in Chapter 7.

2.1 Heat-Release Analysis

Analyzing the measured in-cylinder pressure signal is probably one of the most common ways of trying to understand the processes occurring inside the combustion chamber. In order to better understand the physical processes behind the pressure variations, models which relate volume change, combustion heat release, heat transfer, gas composition, temperature and mass flows to the in-cylinder pressure are necessary parts of the analysis. This kind of model-based pressure-signal processing is also known as heat-release analysis.

A class of simpler models builds upon the first law of thermodynamics and the ideal gas law in order to model the cylinder gases as a system of one or more homogeneous zones without spatial resolution that exchange work and heat with their boundaries. These models are popular both because of their simplicity but also for their ability to predict measured pressure data. One of the earlier models of this class was presented by [Rassweiler and Withrow, 1938], they divided the pressure change as the sum of the effects from the polytropic volume change and the combustion process in order to study the mass-fraction burnt. In [Matekunas

et al., 2000] this quantity was instead studied by computing the ratio of fired to motored pressure curves.

A very popular and slightly more detailed model was presented by [Gatowski, 1984], here a model of heat transfer, thermodynamic properties and mass flow to and from crevice volumes was also included. A simplified Gatowski model was used in the work presented in this thesis, a description of this model is now given.

The Cylinder-Pressure Equation

By treating the in-cylinder gas during the closed part of the cycle as a thermodynamic system with the combustion chamber as its boundary and applying the ideal-gas state equation together with the first law of thermodynamics, the following differential equation for the in-cylinder pressure p with the crank angle θ as the independent variable can be derived assuming constant engine speed [Heywood, 1988],

$$\frac{dp}{d\theta} = -\frac{\gamma}{V}\frac{dV}{d\theta}p + \frac{\gamma-1}{V}\left(\frac{dQ_c}{d\theta} - \frac{dQ_{ht}}{d\theta}\right). \tag{2.1}$$

The right hand side of Eq. (2.1) relates the pressure change to the cylinder volume V, the combustion heat-release rate $dQ_c/d\theta$, the heat-transfer rate $dQ_{ht}/d\theta$ and the ratio of specific heats $\gamma = c_p/c_v$. More detailed models that also take into account crevice effects, radiation, boundary layers and multiple cylinder zones as presented in [Heywood, 1988] were not considered here. By solving Eq. (2.1) for $dQ_c/d\theta$,

$$\frac{dQ_c}{d\theta} = \frac{\gamma}{\gamma-1}p\frac{dV}{d\theta} + \frac{1}{\gamma-1}V\frac{dp}{d\theta} + \frac{dQ_{ht}}{d\theta}, \tag{2.2}$$

$dQ_c/d\theta$ can be computed and analyzed. The fraction of 10% burnt, θ_{10}, which, in this work, is considered to be the start of combustion and the fraction of 50% burnt, θ_{50}, which is considered to be the combustion timing, can be obtained from the accumulated heat release Q_c and the relation

$$x = 100\frac{Q_c(\theta_x)}{\max\limits_{\theta} Q_c(\theta)}. \tag{2.3}$$

Pressure Sensor Model

The in-cylinder pressure was measured with piezo-electric sensors. This measurement technique has high cut-off frequency, good linearity and handling of the tough environment inside the combustion chamber. The signal given by these sensors is usually given on the form

$$p_{\text{meas}} = kp + \Delta p, \tag{2.4}$$

where p_{meas} is the measured in-cylinder pressure signal, p the actual pressure, k and Δp are the sensor conversion factor and offset. Methods for determining

k and Δp are presented by [Randolph, 1990]. In this work, k is known from sensor calibration and Δp is determined by referencing the cylinder pressure at inlet valve closing (IVC) to the measured intake-manifold pressure p_{in}. The measured pressure signal might also be corrupted by current leakage and thermal shock [Johansson, 2006], compensation for such phenomena was not carried out. High-frequency noise in p_{meas} that usually occurs during the combustion event was in this work attenuated using a zero-phase digital filter.

Cylinder Geometry

The cylinder volume V was modelled as a crank-sliding mechanism on the form

$$V = V_c + \frac{V_d}{2}\left(R - \cos(\frac{\pi}{180}\theta) + 1 - \sqrt{R^2 - \sin^2(\frac{\pi}{180}\theta)}\right) \tag{2.5}$$

where V_d, V_c are displacement and clearance volume, R is the ratio of the connecting rod to crankshaft length. Usually, there is an unknown top-dead-center (TDC) crank-angle offset $\theta_{\Delta\text{TDC}}$, between the assumed volume curve and true volume curve, an offset which has previously been shown to greatly degrade the quality of the model in Eq. (2.1) [Amann, 1985]. Online estimation of $\theta_{\Delta\text{TDC}}$ is considered in Chapter 5.

Ratio of Specific Heats

The ratio of specific heats $\gamma = c_p/c_v$ has been shown to have a great impact on the model-output error of Eq. (2.1), [Klein, 2004]. Physically, it is determined by the composition and the temperature, T, of the in-cylinder gases. In this work γ was modelled in one of two different ways:

- By the use of NASA specific-heat polynomials [Heywood, 1988], the in-cylinder gas temperature and composition. The temperature, T, was approximated from measured intake conditions at inlet-valve closing

  $$T = \frac{pVT_{\text{IVC}}}{p_{\text{IVC}}V_{\text{IVC}}} \tag{2.6}$$

  and the gas composition during compression and expansion was given from the measured EGR and air-to-fuel ratio. The gas composition is non-trivial to determine during combustion, it was therefore chosen as an interpolation between the unburnt- and burnt-gas composition. The species considered were N_2, O_2, CO_2, and H_2O.

- By assuming the relation for adiabatic compression

  $$pV^\gamma = C \tag{2.7}$$

  during the compression stroke and then estimating γ and the constant C from p and V with the use of least-squares minimization as presented in [Tunestål, 2001].

Heat-Transfer Model

The convective heat-transfer rate was modeled using Newton's law of cooling

$$\frac{dQ_{ht}}{d\theta} = \frac{h_c A}{60 N_{\text{speed}}}(T - T_w), \tag{2.8}$$

with wall-surface temperature T_w, combustion-chamber area A, engine speed in rpm N_{speed} and the convection coefficient h_c with the empirical expression

$$h_c = 3.26 B^{0.2} p^{0.8} T^{-0.55} \omega^{0.8}, \tag{2.9}$$

derived from a Nusselt-Reynolds relation as presented by [Woschni, 1967]. Here, B is the cylinder bore and ω the mean cylinder-gas velocity, given by

$$\omega = C_1 S_p + C_2 \frac{V T_{\text{IVC}}}{p_{\text{IVC}} V_{\text{IVC}}}(p - p_m), \tag{2.10}$$

where C_1 and C_2 are engine dependent empirical parameters, S_p is the mean piston speed and p_m is the assumed motored pressure curve, alternatives to this model are presented in the works of [Annand, 1963] and [Hohenberger, 1979]. The problem of estimating the parameter C_2 is considered in Chapter 5.

Cylinder-Wall Temperature

The cylinder-wall temperature T_w is physically determined by the heat transfer from the in cylinder gases, and the heat transfer to the engine coolant with temperature T_c. The cylinder wall and piston head is here modeled as a single mass with conductive coefficient k_c, thickness L_c, mass and specific heat m_c and c_p. Assuming that the wall is in steady state and that the outer wall surface has fixed temperature T_c gives the dynamical equation for T_w

$$\frac{dT_w}{d\theta} = -\frac{2A(h_c + k_c/L_c)}{60 N_{\text{speed}} m_c c_p} T_w + \frac{2Ah_c}{m_c c_p 60 N_{\text{speed}}}(T + T_c), \tag{2.11}$$

or on more compact form

$$\frac{dT_w}{d\theta} = A_w(\theta) T_w + B_w(\theta)(T + T_c), \tag{2.12}$$

this model was previously presented in [Roelle, et al., 2006; Widd, et al., 2008,2012]. During the intake (exhaust) stroke T was assumed to take a constant temperature equal to the measured intake (exhaust) temperature.

2.2 Load Definitions

The measured in-cylinder pressure was also used to compute the gross and net indicated mean effective pressures, p_{IMEPg}, p_{IMEPn}, measures of the engine's ca-

pacity to do work, defined accordingly

$$p_{\text{IMEPg}} = \frac{1}{V_d}\int_{\text{IVC}}^{\text{EVO}} p dV, \tag{2.13}$$

$$p_{\text{IMEPn}} = \frac{1}{V_d}\oint p dV, \tag{2.14}$$

where the first integral is taken over the closed part of the cycle and the second is taken over the complete cycle. The gross mean effective pressure p_{IMEPg} is more commonly defined as

$$p_{\text{IMEPg}} = \frac{1}{V_d}\int_{BDC}^{BDC} p dV, \tag{2.15}$$

where BDC denotes bottom dead center and the integral is taken over the compression and expansion strokes, the difference between the two definitions is determined by the engine valve timings and the manifold pressures.

2.3 Ignition Delay

The ignition delay, commonly defined as the time interval between the start of injection and the start of combustion in a direct-injection combustion engine depends on physical processes such as fuel atomization, vaporization and the mixing of the fuel and air in the cylinder, it also depends on the chemical processes of pre-combustion reactions [Heywood, 1988]. The ignition delay is a key variable in PPC where it gives the fuel more time to mix with the gas mixture before the start of combustion. Here, the ignition delay τ is defined as the time in milliseconds between the crank angle of the start of fuel injection θ_{SOI} and the crank angle of 10 % heat released θ_{10},

$$\tau = \frac{\theta_{10} - \theta_{\text{SOI}}}{0.006 N_{\text{speed}}}. \tag{2.16}$$

Where θ_{SOI} is defined as the timing of the injector-current pulse timing plus an additional injector time delay.

Assuming that the chemically controlled part of τ, the auto-ignition time, gives most contribution to the τ variability, models that correlate τ with the cylinder-gas mixture state and composition were studied. As the ignition delay gets longer the relative importance of the chemically controlled part increases, however the opposite also holds, thus for short ignition delays the physical factors become more important, this would decrease the performance of these types of models [Heywood, 1988].

Detailed reaction mechanisms for larger hydrocarbons consist of thousands of species and tens of thousands of reactions [Lu, (2009)]. The model complexity can be reduced by removing or lumping reactions of less importance, or by

building empirical models that uses just enough species and reactions to represent experimental data. A widespread example of the latter is a global reaction mechanism using only five representative species and eight reactions that was developed by [Halstead et al, 1975, 1977] to model two-stage ignition in a rapid compression machine.

The empirical modeling approach was adopted in this work where three different low-order models (M1, M2 and M3) with increasing complexity were considered.

M1

The first model is given by the following expression

$$\tau = Ae^{E_a/R\bar{T}}(\overline{[O_2]})^{\alpha}(\overline{[C_nH_m]})^{\beta}\bar{p}^{\gamma}S_p^{\delta}, \tag{2.17}$$

where E_a is an apparent activation energy, R is the universal gas constant, A, α, β, γ and δ are fuel dependent empirical parameters, $\bar{p}$ and $\bar{T}$ are the mean cylinder pressure and temperature between θ_{SOI} and θ_{10}, $\overline{[O_2]}$ and $\overline{[C_nH_m]}$ are the mean oxygen and global fuel concentration in the cylinder during the same time period assuming that all the fuel has been injected, finally, S_p is the mean piston speed.

The unknown model parameters ϑ_{M1} in this model are given by

$$\vartheta_{M1} = [A, E_a, \alpha, \beta, \gamma, \delta]^T. \tag{2.18}$$

Similar models were presented by [Heywood, 1988] and were used by [Kempinski and Rife, 1981] and also by [Donald and Eyzat, 1978] to parameterize the ignition delay for different fuels and engines.

M2

The second model is a crank-angle resolved extension of M1 where it is assumed that the combustion starts when the integral in Eq. (2.19) reaches the threshold value of 1

$$\int_{\theta_{SOI}}^{\theta_{SOI}+\tau} Ae^{-E_a/(RT)}[O_2]^{\alpha}[C_nH_m]^{\beta}p^{\gamma}S_p^{\delta}d\theta = 1. \tag{2.19}$$

The unknown model parameters ϑ_{M2} in this model are given by

$$\vartheta_{M2} = [A, E_a, \alpha, \beta, \gamma, \delta]^T. \tag{2.20}$$

This model was previously presented by [Thurns, 1996] and [Chmela et al., 2007] among others.

M3

The third model is a two-stage reaction model with empirically determined reaction rates as presented in [Westbrook and Dryer, 1981]. In the first reaction,

Eq. (2.21), the fuel C_nH_m is reacting with O_2 to form CO and C_nH_m. CO and O_2 are then turned into CO_2 in the second reaction, Eq. (2.22).

$$C_nH_m + (\frac{n}{2} + \frac{m}{4})O_2 \xrightarrow{k_1} nCO + \frac{m}{2}H_2O \tag{2.21}$$

$$CO + \frac{1}{2}O_2 \xrightarrow{k_2} CO_2 \tag{2.22}$$

The reaction rates are modeled using the differential equations

$$\frac{d[C_nH_m]}{dt} = -k_1[C_nH_m]^\beta[O_2]^\alpha, \tag{2.23}$$

$$\frac{d[O_2]}{dt} = -(\frac{n}{2} + \frac{m}{4})k_1[C_nH_m]^\beta[O_2]^\alpha - k_2[CO][O_2]^{1/2}, \tag{2.24}$$

$$\frac{d[CO]}{dt} = nk_1[C_nH_m]^\beta[O_2]^\alpha - k_2[CO][O_2]^{1/2}, \tag{2.25}$$

$$\frac{d[CO_2]}{dt} = k_2[CO][O_2]^{1/2}, \tag{2.26}$$

with initial conditions given by the cylinder oxygen concentration and injected fuel amount. The reaction-rate parameters k_i are empirical expressions on the form

$$k_i = A_i e^{-E_a^i/RT} S_p^{\delta_i}. \tag{2.27}$$

Finally, the heat-release rate of the reactions is computed from

$$\frac{dQ_c}{dt} = V(Q_1 k_1[C_nH_m]^\beta[O_2]^\alpha + k_2 Q_2[CO][O_2]^{1/2}), \tag{2.28}$$

where Q_1 and Q_2 are the lower heating value per mole of fuel and CO in Eqs. (2.21) and (2.22). The combustion is assumed to start when Q_c has reached 10 % of the expected total heat released Q_c^{tot}. The unknown model parameters ϑ_{M3} in this model are given by

$$\vartheta_{M3} = [A_1, A_2, E_a^1, E_a^2, \alpha, \beta, \delta_1, \delta_2]^T. \tag{2.29}$$

2.4 Gas System

The gas system configuration considered in this work is displayed in Fig. 4.1. Simple, static models determined from experimental data were used in order to to relate the changes in gas-system valve positions to changes in T_{IVC} and the oxygen concentration in the cylinder at IVC, $[O_2]_{\text{IVC}}$. In Fig. 2.1, T_{IVC} and $[O_2]_{\text{IVC}}$ are displayed as functions of the positions of the long and short-route EGR valves θ_{LR}, θ_{SR} and the positions of the hot-route valve θ_{Hot} prior to the intake manifold. The cool-path valve position θ_{Cool} were changed by setting

$$\theta_{\text{Cool}} = \cos^{-1}(1 - \cos(\theta_{\text{Hot}})) \tag{2.30}$$

in order to keep an approximately constant total valve-opening area. This approach was previously used by [Widd et al., 2009]. The oxygen concentration $[O_2]_{IVC}$ was computed according to

$$[O_2]_{IVC} = \chi_{O_2}^{air} \frac{120\dot{m}_{air}}{6M_{air}V_d N_{speed}} + \chi_{O2}^{ex} \frac{120\dot{m}_{EGR}}{6M_{ex}V_d N_{speed}} + \frac{m_{res}}{M_{ex}V_d}, \tag{2.31}$$

where $\dot{m}_{air}$ is the measured engine air flow, M_{air} , M_{ex}, $\chi_{O_2}^{air}$ and $\chi_{O_2}^{ex}$ are the molar masses and oxygen molar fractions of air and the exhaust gases, the latter was computed using exhaust λ sensor measurements. A Kalman filter [Kalman, 1960] was used to estimate the EGR mass flow $\dot{m}_{EGR}$ using the following dynamic model for the intake-manifold (IM) pressure

$$\frac{dp_{IM}}{dt} = \frac{RT_{IM}}{V_{IM}}(\dot{m}_{air} + \dot{m}_{EGR} - \dot{m}_{cyl}) + \frac{p_{IM}}{T_{IM}}\frac{dT_{IM}}{dt}, \tag{2.32}$$

by assuming that the mass flow to the cylinders $\dot{m}_{cyl}$ is given by

$$\dot{m}_{cyl} = \eta_{vol}\frac{6N_{speed}}{120}\frac{p_{IM}V_d}{RT_{IM}}, \tag{2.33}$$

where η_{vol} is the volumetric efficiency, and using the measured engine air flow $\dot{m}_{air}$, intake manifold pressure p_{IM} and temperature T_{IM}. A similar technique for estimating $\dot{m}_{EGR}$ is presented in [Lee, Park et al., 2013]. The residual-gas mass m_{EGR} was computed using the state in the exhaust manifold (EM) at exhaust valve opening (EVO),

$$m_{res} = \frac{p_{EM}V_{EVO}}{RT_{EM}}. \tag{2.34}$$

The approach of modeling the relation between the gas-system valve positions and the intake-manifold temperature and oxygen concentration presented above is of course an oversimplification. A more convincing model should include pressure differences over valves, turbocharger effects, flow temperatures and the influence of λ on the EGR composition. However, the simple approach introduced above seemed to work sufficiently well in the operating range investigated in the following chapters. Examples of more elaborate gas-system models can be found in [Guzzela and Onder, 2009].

2.5 Model Validation

Measures are needed in order to evaluate the model performance, a measure used in this thesis is the R^2 statistic which is defined as

$$R^2 = 1 - SS_{err}/SS_{tot}, \tag{2.35}$$

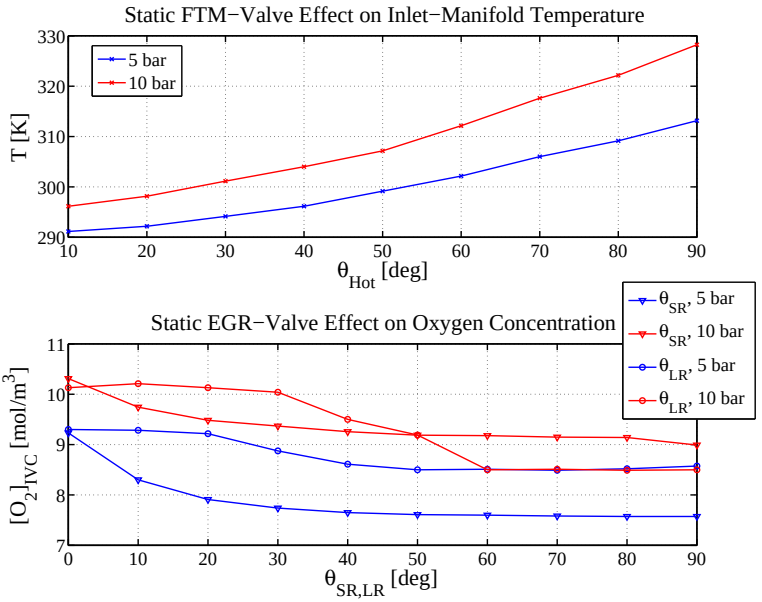

Figure 2.1 T_{IVC} and $[\mathrm{O}_2]_{\mathrm{IVC}}$ as functions of θ_{LR}, θ_{SR} and θ_{Hot} at two different loads at 1200 rpm. These experimentally obtained functions were used to model the relation between the gas-exchange valve positions and the intake manifold conditions. Note that the gain from the short-route EGR valve decreases with load, this is partly because of the decreased pressure difference between the exhaust and the intake due to the increased turbocharger boost.

[Casella and Berger, 2002], where SS_{err} is the sum-of-squares of the model error. SS_{tot} is the sum-of-squares of the sampled data to be predicted. The root-mean-square error (RMSE) was also used and is defined as the standard deviation of the difference between the observed data x and the model output $\hat{x}$,

$$\mathrm{RMSE}(\hat{x}) = \sqrt{E(\hat{x}-x)^2}. \tag{2.36}$$

3

Control and Estimation Methods

This chapter gives an overview of the control and the estimation methods used in the thesis.

3.1 Control

Linearization

The model-based controllers presented in Chapters 7, 8 and 9 all follow the principle of model predictive control which is an optimal-control design for linear systems. The combustion models presented in Chapter 2 are however nonlinear. In order to enable linear controller design, a linearization at the current operating point can be done. Given a nonlinear dicrete-time model on the form

$$\begin{aligned} x(k+1) &= f(x(k), u(k)), \\ y &= h(x(k)), \end{aligned} \tag{3.1}$$

a linear-model approximation

$$\begin{aligned} \Delta x(k+1) &= A\Delta x(k) + B\Delta u(k), \\ \Delta y(k) &= C\Delta x(k), \end{aligned} \tag{3.2}$$

is obtained from the partial derivatives

$$\begin{aligned} A &= \frac{\partial f(x(k), u(k))}{\partial x(k)}(x_0, u_0),\ B = \frac{\partial f(x(k), u(k))}{\partial u(k)}(x_0, u_0), \\ C &= \frac{\partial h(x(k), u(k))}{\partial x(k)}(x_0, u_0), \end{aligned} \tag{3.3}$$

where $\Delta x(k)$, $\Delta u(k)$ and $\Delta y(k)$ are deviations from the linearization point x_0, u_0, y_0. Linearization was used both in Chapter 7 in order to linearize the ignition-delay model and also in Chapters 5 and 8 to linearize the continuous-time heat-release model presented in Chapter 2. Since the linear approximation is only a good close to the point of linearization, the linearization procedure was always redone every engine cycle w.r.t. the current operating conditions.

Model Predictive Control

The following review is based on [Maciejowski, 2002].

Model predictive control (MPC) is a finite-horizon optimal-control principle where the future input sequence $U = \{u(k), ..., u(k+Hc)\}$ from sample k to $k+H_c$ is computed as the minimizer of the cost function J iteratively at every sample k

$$J = \sum_{i=k}^{k+H_p} \mathcal{Y}(i) + \sum_{i=k}^{k+H_c} \mathcal{U}(i) + \rho_\epsilon \epsilon^2. \tag{3.4}$$

The cost function J consists of output costs $\mathcal{Y}(i)$ over a prediction horizon H_p and input costs $\mathcal{U}(i)$ over the control horizon H_c respectively. The output cost at sample i, $\mathcal{Y}(i)$,

$$\mathcal{Y}(i) = \sum_{j=1}^{p} \omega_{y_j} (r_{y_j}(i) - y_j(i))^2, \tag{3.5}$$

is the sum of the squared set-point deviations $r_{y_j}(i) - y_j(i)$ for each output y_j with corresponding set point r_{y_j} scaled with the cost weight ω_{y_j}. The input cost at sample i, $\mathcal{U}(i)$,

$$\mathcal{U}(i) = \sum_{j=1}^{m} \omega_{u_j} u_j(i)^2 + \omega_{\Delta u_j} \Delta u_j(i)^2, \tag{3.6}$$

is the square sum of both absolute input values u_j and changes Δu_j with corresponding weights ω_{u_j}, $\omega_{\Delta u_j}$. The positive cost weights ω_x are controller-design parameters that determines the controller priorities. The minimization of J is done subject to the linear-system dynamics in Eq. (3.1), system initial condition $x(k) = x_0$ and input, output and state constraints over the horizons

$$\begin{aligned}
\epsilon\eta^{y}_{min} + y_{min} &\le y(i) \le y_{\max} + \epsilon\eta^{y}_{\max}, \\
\epsilon\eta^{x}_{min} + x_{min} &\le x(i) \le x_{\max} + \epsilon\eta^{x}_{\max}, \\
\epsilon\eta^{u}_{min} + u_{min} &\le u(i) \le u_{\max} + \epsilon\eta^{u}_{\max}, \\
\epsilon\eta^{\Delta u}_{min} + \Delta u_{min} &\le \Delta u(i) \le \Delta u_{\max} + \epsilon\eta^{\Delta u}_{\max},
\end{aligned} \tag{3.7}$$

where $\epsilon \ge 0$. The positive constant ϵ and the positive vectors η determines the costs for constraint violation, when $\eta = 0$ the corresponding constraint cannot be violated but when $\eta > 0$, the constraint (when $\eta = 0$) can be violated for an additional cost in J, $\eta > 0$ was used in Chapter 9 when the pressure-rise rate was controlled, this was done in order to ensure feasible solutions. Minimizing J subject

to the equality constraints imposed by the system dynamics and the inequality constraint in Eq. (3.7) is a quadratic-programming (QP) problem for which there exist sufficiently fast solvers for online computations. More details on the MPC implementation are presented in Chapter 7 and 9. Once the optimization problem is solved at cycle k, the first input $u^*(k)$ of the minimizing sequence U^* is actuated to the system and the procedure is repeated at the next sample $k+1$.

MPC, receding-horizon control or dynamic programming as it has also been called has previously been applied to a wide range of problems including chemical-process control [Maciejowski, 2002], supply-chain management [Cho, Thoney et al., 2003] and finance [Herbert, 2005]. MPC has also been used for controlling HCCI and PPC engines, examples are presented in [Bengtsson, Strandh et al., 2006a,b, 2007; Widd et al., 2009; Lewander et al., 2008].

The MPC framework was chosen in this work because of its ability to handle input and output constraints. The investigated control problems in this thesis have constraints on valve positions (Chapter 7), the maximum in-cylinder pressure level and in-cylinder pressure-rise rate, see Chapters 8, 9. With active constraints a MPC controller obtains nonlinear properties that are not obtainable with standard linear controller designs such as LQR or PID [Maciejowski, 2002]. The MPC design procedure is also handy when the system is large, as in Chapter 9, the tuning of the cost function weights ω_x is an intuitive way of setting the controller priorities. The MPC framework is also well suited for engine control since the control objective is not always of a regulating nature for instance when the piston work is to be maximized subject to cylinder pressure constraints, see Chapter 8.

3.2 State-Estimation Methods

Given the probabilistic formulation of a dynamic system with state x_k, measurement y_k and input u_k,

$$\begin{aligned} x_{k+1} &\sim p(x_{k+1}|x_k, u_k), \\ y_k &\sim p(y_k|x_k),\ x_0 \sim p(x_0), \end{aligned} \tag{3.8}$$

where $p(x|y)$ denotes the conditioned probability density function of x given y. The state-estimation problem amounts to estimate the state x_k given the measurement y_k or in other words to evaluate the probability density function of x_k given the observations y_k

$$p(x_k|y_k). \tag{3.9}$$

The Kalman Filter

For the case when the system in Eq. (3.8) is linear with additive Gaussian noise

$$\begin{aligned} x_{k+1} &= Ax_k + Bu_k + v_k \\ y_k &= Cx_k + e_k \end{aligned} \tag{3.10}$$

$v_k \sim N(0,Q), e_k \sim N(0,R)$, the estimation problem has an analytic solution and the famous Kalman Filter (KF) [Kalman, 1960] provides an algorithm for iteratively estimating x_k, see Algorithm 1. The Kalman filter was used in Chapter 9 for

Algorithm 1 Kalman Filter

1: Initialize $\hat{x}_0$ and P
2: **while** $k > 0$ **do**
3: $\hat{x}_{k|k-1} = A\hat{x}_{k-1|k-1} + Bu_{k-1}$
4: $P_{k|k-1} = AP_{k|k-1}A^T + Q$
5: $e_k = y_k - C\hat{x}_{k|k-1}$
6: $S_k = CP_{k|k-1}C^T + R$
7: $K_k = P_{k|k-1}C^T S_k^{-1}$
8: $\hat{x}_{k|k} = \hat{x}_{k|k-1} + K_k e_k$
9: $P_{k|k} = (I - K_k C)P_{k|k-1}$
10: **end while**

filtering the cycle-to-cycle variation of the pressure-rise rate and the combustion phasing and in Chapter 7 to estimate the oxygen concentration at IVC $[O_2]_{IVC}$. Unfortunately, if the system Eq. (3.8) is nonlinear on the form

$$\begin{aligned} x_{k+1} &= f(x_k, u_k) + v_k, \\ y_k &= h(x_k) + e_k, \end{aligned} \tag{3.11}$$

the Kalman Filter is not directly applicable for estimating x_k, fortunately, there are well-established methods for nonlinear estimation problems. The extended Kalman filter (EKF) and the particle filter (PF) are examples that were used in Chapter 5 for automatic calibration of the heat-release analysis model presented in Chapter 2.

The Extended Kalman Filter

The EKF provides an approximate solution to the estimation problem by linearizing Eq. (3.11) at the current estimate in order to apply the iterative KF procedure used for linear systems [Julier and Uhlmann, 2004]. The procedure is presented in Algorithm 2.

The Particle Filter

The PF is a sequential Monte Carlo sampling method that aims to approximate the conditional distribution, Eq. (3.9), numerically. The PF presented below was

Algorithm 2 Extended Kalman Filter

Initialize $\hat{x}_0$ and P
while $k > 0$ **do**
  $\hat{x}_{k|k-1} = f(\hat{x}_{k-1|k-1}|u_{k-1})$
  $P_{k|k-1} = A_{k-1}P_{k|k-1}A_{k-1}^T + Q_{k-1},\ A_{k-1} = \frac{\partial f}{\partial x}|_{\hat{x}_{k-1|k-1},u_{k-1}}$.
  $e_k = y_k - h(\hat{x}_{k|k-1})$
  $S_k = C_k P_{k|k-1} C_k^T + R_k,\ C_k = \frac{\partial h}{\partial x}|_{\hat{x}_{k|k-1},u_{k-1}}$
  $K_k = P_{k|k-1}C_k^T S_k^{-1}$
  $\hat{x}_{k|k} = \hat{x}_{k|k-1} + K_k e_k$
  $P_{k|k} = (I - K_k C_k)P_{k|k-1}$
end while

first introduced by [Gordon et al., 1993]. The particle filter consists of a set of N_p sampled particles x_k^i with corresponding weights ω^i, together they provide a point-mass distribution approximation

$$p(x_k|y_k) \approx \sum_{i=1}^{N_p} \omega_k^i \delta(x_k - x_k^i) \tag{3.12}$$

The PF performs the sampling procedure using a sequential Monte Carlo technique where particles are sequentially generated by sampling x_{k+1} given the old particles x_k^i using a proposal distribution $q(x_{k+1}|x_k^i)$. After each time step, the weights are updated in order to represent the desired probability density function in Eq. (3.9). When choosing $q(x_{k+1}|x_k^i) = p(x_{k+1}|x_k, u_k)$, the update rule for the weights becomes $\omega_{k+1}^i = \omega_k^i p(y_{k+1}|x_{k+1})$. To avoid particle depletion which means that only a few weights contributes to Eq. (3.12), the particles have to be resampled according to the weight distribution, this procedure puts more particles into areas of high probability and discards particles in regions of low probability. The resampling step is often done if the ratio between N_p and the number of effective particles N_{eff}

$$N_{\text{eff}} = \frac{1}{\sum_{i=1}^{N} (\omega^i)^2}. \tag{3.13}$$

becomes too low. This type of PF is called a bootstrap PF and is presented in Algorithm 3.

Algorithm 3 Particle Filter

1: Draw N_p particles, x_0^i from the initial distribution $p(x_0)$ and initial the weights $\omega_0^i = 1/N_p$.
2: **while** $k > 0$ **do**
3: Update the particles x_{k+1}^i by sampling $p(x_{k+1}|x_k^i, u_k)$
4: Update the weights according to $\omega_{k+1}^i = \omega_k^i p(y_{k+1}|x_{k+1})$ and normalize.
5: **if** $N_{\text{eff}} < x_{\text{frac}} N_p$ **then**
6: Draw new particles from the distribution defined by $\{\omega_k^i\}_{i=1..N_p}$.
7: Set the weights $\omega_k^i = 1/N_p$
8: **end if**
9: **end while**

4

Experimental Setup

Engine Specifications

A Scania D13 heavy-duty diesel engine with specifications shown in Table 4.1 was used in the experiments presented in the thesis. The engine speed was controlled with a 355 kW AC motor that worked both as an engine motor and brake. The engine had a modified gas-exchange system with water-cooled short and long-route EGR paths a fast thermal management system prior to the intake manifold and was boosted with a fixed-geometry turbocharger, see Fig 4.1.

Engine Control System, Sensors and Actuators

The entire engine control system was programmed with LabVIEW which is a graphical programming environment developed by National Instruments. The real-time system consisted of a NI PXIe-8135 embedded controller (2.3 GHz quad-core processor), NI PXI-7854/7854 R (Multifunction reconfigurable I/O with Virtex 5-LX110/LX30 FPGA). The FPGA was considered as a configurable hardware that worked as a flexible AO / DIO, it was also used for AD acquisition, triggered by the crank-angle encoder. The ADC sampled the analog signals with a 16-bit resolution. The user interface was run on a separate host PC with a Win-

Table 4.1 Engine Specifications

Total Displaced volume	12.74 dm^3
Number of Cylinders	6
Stroke	160 mm
Bore	130 mm
Connecting Rod	255 mm
Compression ratio	18:1
Number of Valves	4

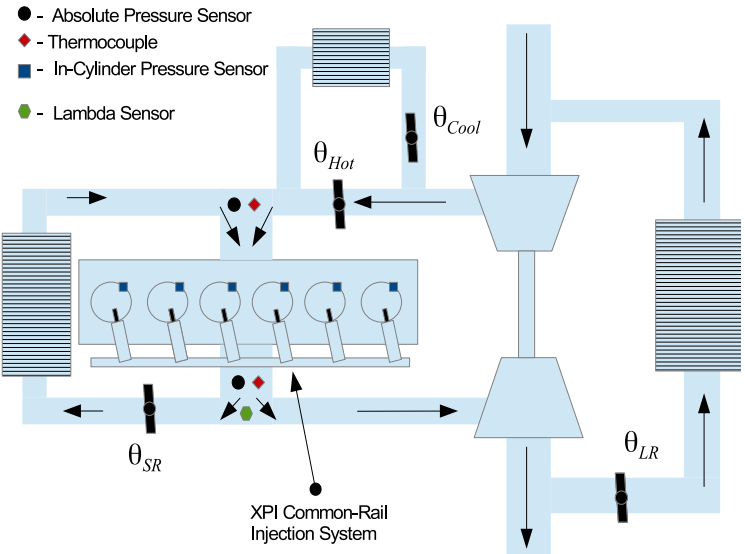

Figure 4.1 The Scania D13 gas-system setup, the valve angles θ_{Cool} and θ_{Hot} were used to control the inlet-manifold gas temperature while the valve angles θ_{SR} and θ_{LR} were used to dilute the intake air with EGR.

dows 7 operating system which communicated with the real-time system over TCP/IP.

Sensors The in-cylinder pressure was measured with water-cooled Kistler 7061B pressure sensors and was sampled with the Leine-Linde crank angle encoder pulse every 0.2 crank angle degree. Inlet- and exhaust manifold and pressures were measured with Keller PAA-23S absolute pressure sensors, temperatures were measured with K-type thermocouples. The NO_x and HC emission levels were measured with a Horiba measurement system (MEXA-9100E) while the soot levels were measured with an AVL micro soot-sensor measurement unit. The fuel- and air flow was measured by a mini CORI-FLOW M15 coriolis-effect mass-flow meter and a hot-film air-mass flow meter respectively, both were Bronkhorst High-Tech B.V products. A lambda sensor was located in the exhaust manifold for air-fuel ratio measurement.

Actuators The fuel-injection system was a production xtra high pressure injection (XPI) common-rail injection system for the Scania D13 engines. The actuators of the fuel-injection were the common-rail inlet-metering valve position and the injector current signals that determine fuel-injection timing, duration and distribution. The actuators in the gas-exchange system were the short and

long-route EGR valves θ_{SR} and θ_{LR} and the valves in the thermal management system θ_{Hot} and θ_{Cool}, see Fig. 4.1. The common-rail pressure, injection timings, durations and valve positions were controlled from the real-time system using Drivven drivers.

Real-Time Computation The real-time heat-release analysis and controller computations were run in LabVIEW MathScript RT Module nodes inside timed loops on the real-time system. All computations were done using floating point arithmetic. PID controllers were implemented using the LabVIEW PID advanced VI and QP problems were solved using the LabVIEW quadratic programming VI.

Fuel The fuel used in the experiments was a mix of 80 volume % gasoline and 20 volume % N-heptane. This ratio was chosen based on previous results done by [Manente, 2010c] which showed that an octane number of 80 could be used for a wide operating range.

5

Online Heat-Release-Model Calibration

5.1 Introduction

Simple heat-release models like the one introduced in Chapter 2 have proven to be important tools for engine diagnostics, research studies, control and simulation. These models all have a set of unknown parameters that have to be tuned for satisfactorily performance. The tuning of these parameters can be done manually using experience of how each component of the model should behave and how physical estimated heat release rates should look like, this is however a time-consuming work that has to be redone from time to time.

The development of automatic calibration methods has been an active research area for the past decades, where automatic methods for calibrating pressure sensor offset [Tunestål et al., 2001; Brunt and Pond, 1997], polytropic coefficients [Manente, et al., 2008; Randolph, 1990], volume-curve offset [Stas, 2004; Tunestål, 2001] and compression ratio [Klein et al., 2004] have been presented. In [Klein, 2008], an offline method for calibration of a large set of parameters simultaneously was presented and studied in detail. It was concluded by [Eriksson, 1998], that all model parameters might not be simultaneously identifiable, this indicates that a calibration problem involving a large set of parameters is not easily solved.

In this chapter, a calibration problem which considers a subset of the model parameters in the simplified Gatowski model, presented in Chapter 2, is formulated as a nonlinear estimation problem where unknown states in a dynamic system are to be estimated given a statistical physics-based model and sensor measurements. The estimation problem is then solved using the extended Kalman filter and the bootstrap particle filter presented in Chapter 3. These filters lend themselves nicely for real-time applications because of their sequential processing of measured data and the increased amount of available computational power in today's computers which makes these methods more viable. The

outline of this chapter is to first present the estimation-problem formulation and then filter performance results w.r.t. simulation and experimental data.

5.2 Problem Formulation

Given the heat-release model

$$\frac{dQ_c}{d\theta} = \frac{\gamma}{\gamma-1}p\frac{dV}{d\theta} + \frac{1}{\gamma-1}V\frac{dp}{d\theta} + \frac{dQ_{ht}}{d\theta}, \tag{5.1}$$

where γ is determined from NASA polynomials and $dQ_{ht}/d\theta$ is given by the Woschni heat-transfer model in Eqs. (2.8-2.10), let us consider the problem where the TDC offset $\theta_{\Delta TDC}$, the convective heat-transfer coefficient C_2 and the cylinder-wall temperature T_w are all unknown parameters to be estimated. The parameter C_2 was chosen because it was previously shown to be the more important heat-transfer-rate parameter, [Klein, 2008]. Now, if these parameters are set correctly, the accumulated heat release should be zero before the start of combustion and constant at the level given by the burnt fuel energy after the combustion. Measurement noise, model uncertainty and cycle-to-cycle variation will of course introduce stochastic errors to this assumption, therefore, the accumulated heat release given the correct parameters is modeled according to

$$Q_c(\theta) = \begin{cases} \epsilon_1 & \theta \leq \theta_{SOC}, \\ Q_{\text{tot}} + d + \epsilon_2 & \theta \geq \theta_{EOC}, \end{cases} \tag{5.2}$$

where $\epsilon_1 \sim N(0,\sigma_1^2)$ and $\epsilon_2 \sim N(0,\sigma_2^2)$ are i.i.d normally distributed noise processes, with standard deviations σ_i. The variable $d \sim N(0,\sigma_d^2)$ is a random offset accounting for variations in the injected fuel energy. A realization of the model output given the correct variables can be viewed in Fig. 5.1.

The Nonlinear State-Space Model with Gaussian Noise

In order to estimate the unknown model parameters C_2, $\theta_{\Delta TDC}$ and T_w on a cycle-to-cycle basis using a statistical framework, the parameters are assumed to be driven by a Gaussian-noise process v_k which represents their assumed un-

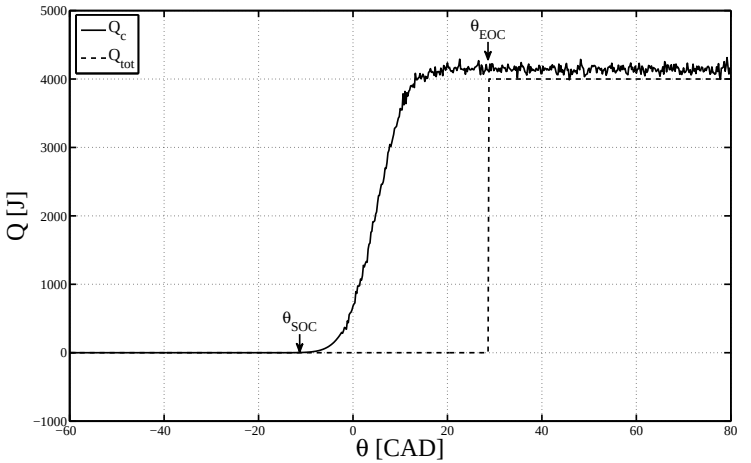

Figure 5.1 A realization of the statistical model in Eq. (5.2), the dashed line represents the expected accumulated heat release before and after combustion without the stochastic variations, the solid line represents an actual accumulated heat release with an offset d and noise ϵ_1, ϵ_2, here $\sigma_1^2 = 0, \sigma_2^2 = 2500$.

certainty over time, this gives the complete model

$$\begin{pmatrix} C_2^{k+1} \\ \theta_{\Delta TDC}^{k+1} \\ T_w^{k+1} \end{pmatrix} = \begin{pmatrix} 1 & 0 & 0 \\ 0 & 1 & 0 \\ 0 & 0 & \Phi \end{pmatrix} \begin{pmatrix} C_2^{k} \\ \theta_{\Delta TDC}^{k} \\ T_w^{k} \end{pmatrix} + \begin{pmatrix} 0 \\ 0 \\ \Gamma_1 T + \Gamma_2 T_c \end{pmatrix} + \nu_k \tag{5.3}$$

$$\frac{dQ_c}{d\theta} = \frac{\gamma}{\gamma - 1} p \frac{dV}{d\theta} + \frac{1}{\gamma - 1} V \frac{dp}{d\theta} + \frac{dQ_{ht}}{d\theta},$$

$$Q_c(\theta) = \begin{cases} \int dQ_c + \epsilon_1 & \theta \le \theta_{SOC}, \\ \int dQ_c & \theta_{SOC} \le \theta \le \theta_{EOC}, \\ Q_{\text{tot}} + d + \epsilon_2 & \theta \ge \theta_{EOC}, \end{cases}$$

where

$$\nu_k \sim N(0, \Sigma_1), \tag{5.4}$$

$$\Phi = e^{\oint A_w(\theta) d\theta}, \tag{5.5}$$

$$\Gamma_1 T + \Gamma_2 T_c = \oint e^{\int_{\theta_{BDC}}^{\vartheta} A_w(\vartheta) d\vartheta} B_w(\theta)(T + T_c) d\theta \tag{5.6}$$

here k denotes cycle index and the covariance matrix Σ_1 is a measure of the model uncertainty. An initial distribution is also assumed according to

$$\begin{pmatrix} C_2^0 & \theta_{\Delta TDC}^0 & T_w^0 \end{pmatrix}^T \sim N(\mu_0, \Sigma_0) \tag{5.7}$$

where μ_0 is an initial parameter guess with corresponding covariance Σ_0. The model in Eqs. (5.3-5.7) is now on the form

$$\begin{aligned} x_{k+1} &= f(x_k, u_k) + v_k, \\ y_k &= h(x_k) + e_k,\ x_0 = \mu_0 + e_0, \end{aligned} \tag{5.8}$$

which has been studied extensively in the context of nonlinear estimation theory where x_k is to be estimated given measurements y_k and the assumed model in Eq. (5.8).

5.3 Observability

Before trying to do state estimation given a system on the form Eq. (5.8) it is crucial to study the system observability which is a well-established concept in linear system theory that was introduced by [Kalman, 1959]. The observability is a measure of how well the system state x_k can be inferred by knowledge of the systems outputs y_k. In order to apply the concept of observability, to the system in Eqs. (5.3-5.7), a linearization (following the procedure in Chapter 3) was performed at the operating point presented in Table 5.1. This gave the linear system

$$\begin{aligned} \Delta x_{k+1} &= A\Delta x_k + B\Delta u_k, \\ \Delta y_k &= C\Delta x_k. \end{aligned} \tag{5.9}$$

Since A was found to be close to I_{3x3}, the observability could be studied by investigating C to see how sensitive Δy_k (Q_c) is to deviations in the state variables, Δx_k. A rescaled C is presented in Fig. 5.2. It can be seen that changes in $\theta_{\Delta TDC}$ has an asymmetric effect on Q_c around TDC, changes in C_2 determines the final accumulated level of Q_c together with T_w which also affects Q during the compression stroke. It is clear that the system is observable since the rows of C are linearly independent, however, positively correlated variations in C_2 and T_w are obviously less observable than negatively correlated ones. Similar results were presented in [Johansson, 2006].

5.4 Filter Configuration

In the EKF (see Algorithm 2), the $\partial f/\partial x$ and $\partial h/\partial x$ matrices were obtained through numerical differentiation of Eq. (5.3). The probability density functions

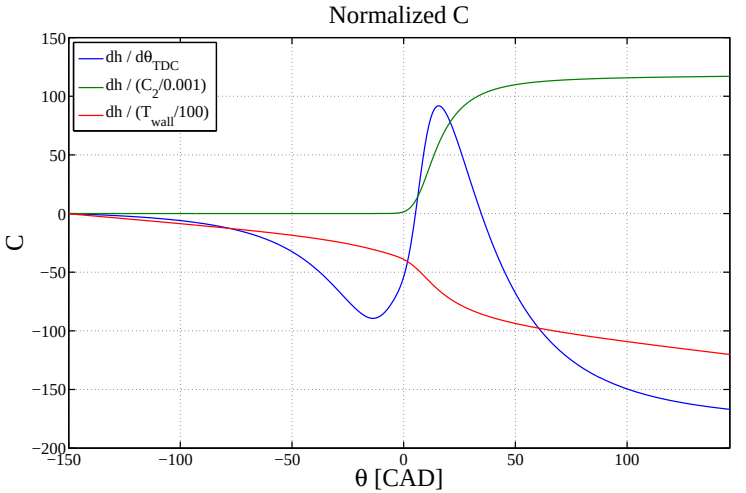

Figure 5.2 Computed C when linearizing Eqs. (5.3-5.7) around the operating point presented in Table 5.1. Clearly, the different states affect Q_c differently, $\theta_{\Delta TDC}$ affects Q_c asymmetrically around TDC while C_2 determines the accumulated heat release level together with T_w which also affects Q_c during the compression stroke.

$p(x_{k+1}|x_k^i, u_k)$ and $p(y_{k+1}|x_{k+1})$ are given directly by Eq. (5.3). The "measurement" or the expected Q_c given the correct parameter values is given by the deterministic part of Eq. (5.2). In order to reduce the computational costs, Eq. (5.2) was downsampled from a resolution of 0.2 CAD to 50 samples before and 50 samples after combustion. Computational times per iteration below 1 ms was obtained for the EKF with compiled Matlab code, in order to have comparable runtimes with the PF (see Algorithm 3), the number of particles N_p was here chosen to be 250 which gave runtimes below 5 ms. The particle number N_p is of course a trade-off between performance and computational complexity, this trade-off was not investigated here. The PF resampling was initiated when the number of effective particles N_{eff} was below $0.25N_p$.

5.5 Simulation Results

In order to evaluate the filters w.r.t. convergence and sensitivity to the statistical assumptions and model-parameter errors, the filters were tested against simulated pressure traces generated from the model

$$\frac{dp}{d\theta} = -\frac{\gamma}{V}\frac{dV}{d\theta}p + \frac{\gamma-1}{V}\left(\frac{dQ_c}{d\theta} - \frac{dQ_{ht}}{d\theta}\right), \; p(\theta_{\text{IVC}}) = p_0, \tag{5.10}$$

Table 5.1 Operating point for filter evaluation, the combustion rate $dQ_c/d\theta$ was chosen as a Gaussian function with a standard deviation of 5 CAD.

Boundary Conditions		Combustion Properties	
p_{in} [bar]	1.3	θ_{50} [CAD]	5
T_{in} [K]	303	θ_{DOC} [CAD]	20
λ [-]	2	$\frac{dQ_c/d\theta}{Q_{\text{tot}}}$ [-]	$N(5,5)$
r_{EGR} [-]	0	Q_{tot} [J]	4×10^3
T_{ex} [K]	400		
Cylinder Geometry		Heat Transfer Parameters	
r_c [-]	16	C_1 [-]	2.28
V_d [m^3]	2.1×10^3	C_2 [m/(sK)]	0.0032
B [mm]	130	T_w [K]	465
L [mm]	160	T_c [K]	333
IVC [CAD]	-151	$m_c c_p$ [J/K]	1150
EVC [CAD]	146	k_c [J/(mK)]	45
$\theta_{\Delta TDC}$ [CAD]	0	L_c [m]	0.025

using a Matlab ODE-solver (ode23s) with the conditions and parameter values presented in Table 5.1 and the following noise densities

$$\sigma_1 = 25,\ \sigma_2 = 25,\ \sigma_d = 100, \tag{5.11}$$

$$\Sigma_0 = \begin{pmatrix} 9/4 & 0 & 0 \\ 0 & 2.5\times10^{-7} & 0 \\ 0 & 0 & 625 \end{pmatrix},\ \Sigma_1 = \begin{pmatrix} 0.0625 & 0 & 0 \\ 0 & 1\times10^{-8} & 0 \\ 0 & 0 & 6.25 \end{pmatrix}.$$

Filter Convergence

In order to investigate the filter convergence, the EKF and the PF were initiated with the correct model parameters according to Table 5.1 apart from the incorrect initial filter states

$$x_0^1 = \left(1,\ 0.0095,\ 595\right)^T,\ x_0^2 = \left(-1,\ 0.002,\ 336\right)^T, \tag{5.12}$$

the correct state being

$$x^* = \left(0,\ 0.0032,\ 465\right)^T. \tag{5.13}$$

The results can be viewed in Fig. 5.3 where the mean convergence and standard deviation from 25 realizations are presented for the different initial conditions, x_0^1 (dashed) and x_0^2 (solid). Note that the cycle-axis scale is different for the two filters.

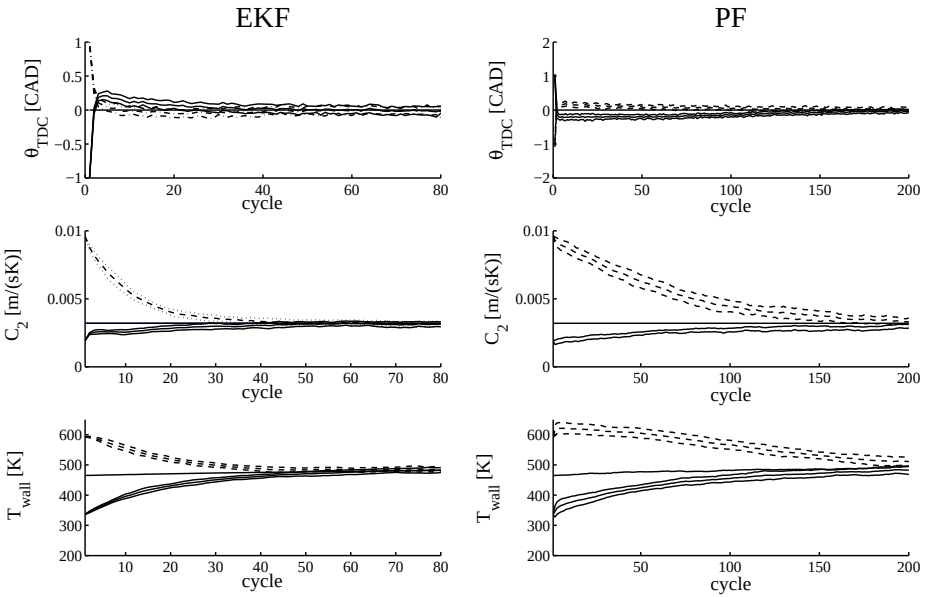

Figure 5.3 Filter convergence with the different initial conditions x_0^1 (dashed) and x_0^2 (solid), note the different cycle-axis for the different filters. It can be seen that the filters converge to the correct state and that the EKF has a higher convergence rate, it is believed that this is due to the directed search of the EKF. Also, note that $\theta_{\Delta TDC}$ changes quite rapidly initially, this indicates a relatively high model sensitivity to $\theta_{\Delta TDC}$ errors.

The sample RMSE (see Chapter 2) for the estimate $\hat{x}_k$, at cycle k,

$$\text{RMSE}(\hat{x}_k) = \sqrt{\frac{\sum_{i=1}^{N}(\hat{x}_k - x^*)^2}{N}}, \tag{5.14}$$

is displayed as the black lines in Fig. 5.4 for the 25 realizations. It can be seen that the filters converge to the correct state and that the EKF has a higher convergence rate, it is believed that this is due to the directed search of the EKF. The convergence rate of the PF could probably be improved by using more particles. Also note that $\theta_{\Delta TDC}$ changes quite rapidly initially, this indicates a relatively high model sensitivity to $\theta_{\Delta TDC}$ errors.

Model Noise Sensitivity

The convergence sensitivity to the assumed model noise was investigated by scaling the filter Σ_1 a factor of 16, the resulting RMSE is presented in as the red

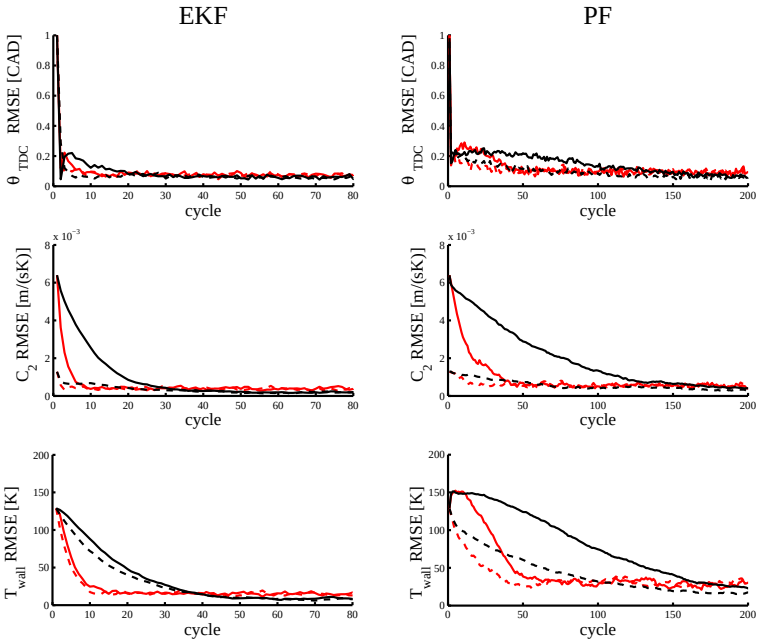

Figure 5.4 Filter RMSE when assuming the correct process noise (black) and an increased assumed process noise (red). An increased assumed process-noise level clearly increases the filter convergence-rate, but seems to increase the steady state RMSE.

lines in Fig. 5.4. The result shows that the increased assumed model noise level gives a higher convergence rate, but a slightly higher steady-state error.

Heat Release Noise Sensitivity

The assumed Q_c noise levels were also varied as σ_1, σ_2 and σ_d were all scaled a factor of 4. The resulting RMSE is shown as the red lines in Fig. 5.5 together with the standard-case RMSE in black. An increased assumed Q_c noise level clearly decreases the convergence rate. The sensitivity to the assumed σ_d was also tested, σ_d was set to 0 while σ_2 was set to $\sqrt{25^2+100^2}$, the result is shown in Fig 5.6 where convergence with the modified noise model is shown in red. Only assuming additive Gaussian noise before and after combustion clearly gives poor convergence when there is a variation in the injected fuel energy, the EKF oscillates greatly initially and also has higher steady-state RMSE.

The filters thus behaves according to standard Kalman-filter theory, an increased assumed model-noise level makes state changes more probable. In the

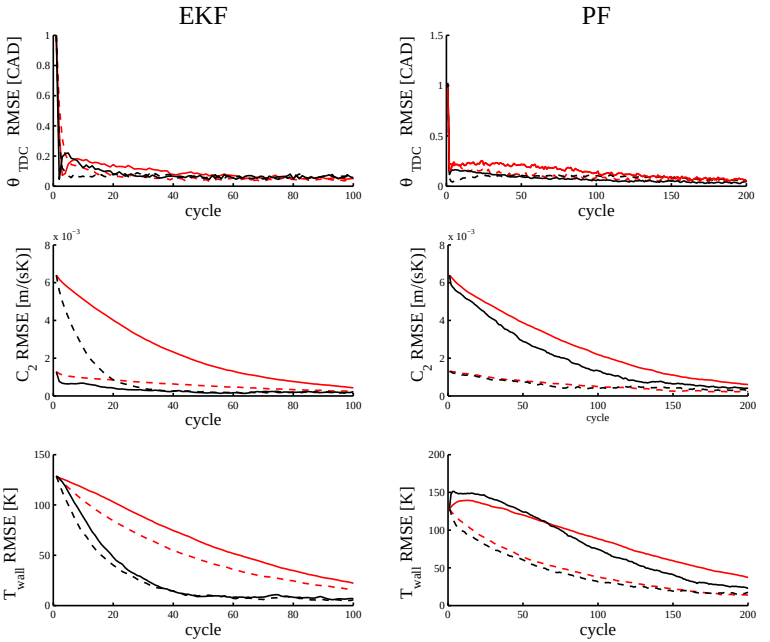

Figure 5.5 Filter RMSE when assuming the correct heat-release noise (black) and an increased assumed heat-release noise level (red), $16\Sigma_1$. An increased assumed heat-release noise level clearly decreases the filter-convergence rate.

EKF, the sensor equation is contributing more to the state estimate in relation to the model dynamics and in the particle filter a larger particle spread is made each sample which makes convergence faster. When the assumed heat-release noise is increased, the correction for heat-release deviation from the assumed correct shape is not as large since larger model errors are more likely. Having a noise model that incorporates a fluctuating injected-fuel energy level is also shown to be important since it then makes constant Q_c after combustion more probable, this makes the filters more robust to variations in the total injected fuel amount.

5.6 Sensitivity to Model-Parameter Errors

The filter sensitivity to erroneous model parameters was also investigated. The sensitivity was studied w.r.t. constant errors in p_{in}, T_{in}, λ, r_c, T_c and Q_{tot}. The stationary parameter-estimate biases due to model-parameter errors are presented in Table 5.2, together with the investigated parameter-error magnitude. The re-

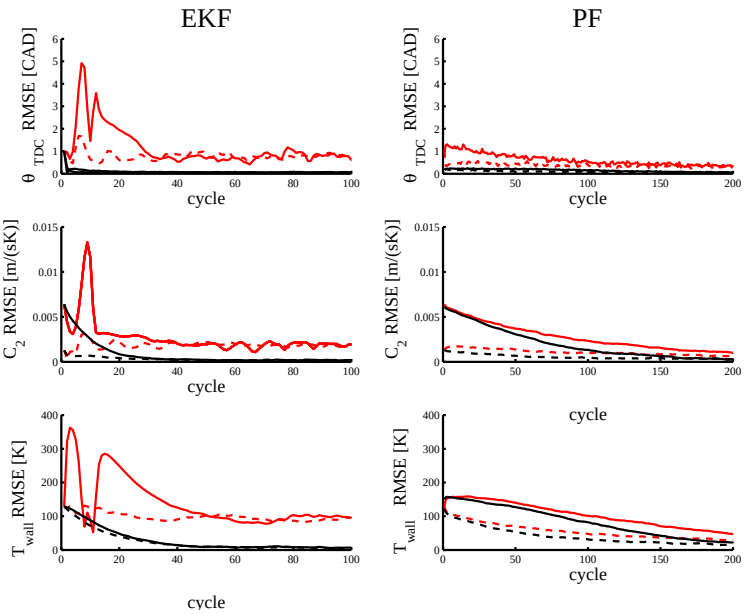

Figure 5.6 Filter RMSE when assuming the correct heat-release-noise level (black) and a modified heat-release-noise level (red) where $\sigma_d = 0$ and $\sigma_2 = \sqrt{25^2 + 100^2}$. Only assuming additive Gaussian noise on Q_c before and after combustion clearly gives poor convergence when there is a variation in the injected fuel energy, the EKF oscillates greatly initially and also has higher steady-state RMSE.

sults show that the filter estimates are very sensitive to errors in p_{in} and r_c and not as sensitive to errors in the other parameters. A positive error in p_{in} or r_c gives an increase in the assumed motored pressure p_m while T is decreased, both effects contribute to a decrease in $dQ_{ht}/d\theta$. The filter-parameter sensitivity could be decreased somewhat by increasing the assumed Q_c noise level. This is indicated by the numbers in parenthesis, they stationary parameter-estimate bias when the assumed Q_c noise standard deviation was scaled a factor of 4. Overall, the results indicate that the PF was less sensitive to model errors, compared to the EKF.

5.7 Experimental Results

The filters were tested against experimental data with a known $\theta_{\Delta TDC}$ of 1 CAD obtained from the operating point presented in Table 5.3. The filter convergence can be seen in Fig 5.7 when initiated at the states in Eq. (5.12) with the following

Table 5.2 Filter sensitivity to model-parameter errors. The filters are more sensitive to errors in p_{in} and r_c and not as sensitive to errors in the other parameters. The PF was overall less sensitive to model errors compared to the EKF. The filter-parameter sensitivity could be decreased somewhat by increasing the assumed Q_c noise levels which is indicated by the numbers in parenthesis, here, the assumed Q_c noise standard deviation was scaled a factor of 4. The units for $\theta_{\Delta TDC}$, C_2 and T_w are CAD, m/(sK) and K.

EKF	PF
p_{in} error, 1.3 ± 0.065 bar	
$\theta_{\Delta TDC} = 0 \pm 0.48$ (0.38)	$\theta_{\Delta TDC} = 0 \pm 0.3$ (0.33)
$C_2 = 0.0032 \pm 0.003$ (0.0024)	$C_2 = 0.0032 \pm 0.0014$ (0.0012)
$T_w = 497 \pm 198$ (151)	$T_w = 497 \pm 100$ (95)
T_{in} error, 303 ± 20 K	
$\theta_{\Delta TDC} = 0 \pm 0.17$ (0.14)	$\theta_{\Delta TDC} = 0 \pm 0.12$ (0.12)
$C_2 = 0.0032 \pm 0.0003$ (0.0001)	$C_2 = 0.0032 \pm 0.00015$ (0.0001)
$T_w = 497 \pm 65$ (45)	$T_w = 497 \pm 40$ (25)
λ error, 2 ± 0.2	
$\theta_{\Delta TDC} = 0 \pm 0.07$ (0.09)	$\theta_{\Delta TDC} = 0 \pm 0.05$ (0.07)
$C_2 = 0.0032 \pm 0.00045$ (0.0004)	$C_2 = 0.0032 \pm 0.0004$ (0.0003)
$T_w = 497 \pm 12$ (10)	$T_w = 497 \pm 7.5$ (7.5)
r_c error, 1.6 ± 0.8	
$\theta_{\Delta TDC} = 0 \pm 0.65$ (0.55)	$\theta_{\Delta TDC} = 0 \pm 0.5$ (0.51)
$C_2 = 0.0032 \pm 0.003$ (0.003)	$C_2 = 0.0032 \pm 0.0017$ (0.0012)
$T_w = 497 \pm 179$ (138)	$T_w = 497 \pm 90$ (70)
T_c error, 333 ± 20 K	
$\theta_{\Delta TDC} = 0 \pm 0.01$ (0.0)	$\theta_{\Delta TDC} = 0 \pm 0.02$ (0.025)
$C_2 = 0.0032 \pm 0.00005$ (0)	$C_2 = 0.0032 \pm 0$ (0.0001)
$T_w = 497 \pm 7$ (4)	$T_w = 497 \pm 9$ (10)
Q_{tot} error, $4 \times 10^3 \pm 200$ J	
$\theta_{\Delta TDC} = 0 \pm 0.15$ (0.1)	$\theta_{\Delta TDC} = 0 \pm 0.13$ (0.12)
$C_2 = 0.0032 \pm 0.001$ (0.0011)	$C_2 = 0.0032 \pm 0.0012$ (0.0013)
$T_w = 497 \pm 30$ (17)	$T_w = 497 \pm 0$ (7)

Table 5.3 Operating point for experimenal evaluation.

N_{speed} [rpm]	1200	Inlet temperature [C]	40
p_{IMEPn} [bar]	10	λ [-]	1.8
Rail pressure [bar]	800	Injected fuel energy [J/cycle]	4680

manually tuned noise model

$$\sigma_1 = 100,\ \sigma_2 = 100,\ \sigma_d = 400, \tag{5.15}$$

$$\Sigma_0 = \begin{pmatrix} 9/4 & 0 & 0 \\ 0 & 2.5\times10^{-7} & 0 \\ 0 & 0 & 625 \end{pmatrix},\ \Sigma_1 = \begin{pmatrix} 0.0625 & 0 & 0 \\ 0 & 1\times10^{-8} & 0 \\ 0 & 0 & 0.1 \end{pmatrix}. \tag{5.16}$$

The chosen noise model gave an acceptable trade-off between convergence rate and steady-state estimate variance. The T_w noise level was here set low so that T_w would follow the dynamical model whilst $\theta_{\Delta TDC}$ and C_2 could be set in order to adjust for a probable Q_c output. The initial Q_c output (black, dashed) is presented in Fig. 5.8 together with the final filter Q_c outputs (red, black) and the known Q_c^{tot} level (blue), computed from fuel-flow measurements. The filters converged at the same rate in around 200 cycles, and managed to detect a significant top-dead-center offset. The filters converged to slightly different final values as can be seen in Fig. 5.7 where the EKF converges to a slightly higher C_2 value. The PF converged closer to the estimated final Q_c value, see Fig. 5.8.

5.8 Summary

The EKF and the PF both seem to be feasible options for online estimation of the studied heat-release model parameters. The simulation results show that both filters were consistent in converging to the correct state. The relation between the assumed model and heat-release noise levels determined the convergence rate and the steady state RMSE, these could be viewed as filter tuning parameters. Assuming a noise model with a variation on the accumulated heat release showed to be crucial when there is a known variation in the total burnt fuel energy, see Fig. 5.6.

The filter model-error sensitivity analysis presented in Table 5.2 indicated that the filters were more sensitive to errors on pressure-sensor offset and compression ratio than to other parameter errors and that the sensitivity was dependent on the assumed noise model.

The filters also showed consistent convergence from different initial states with experimental data and manually tuned filter parameters, see Figs. 5.7 and 5.8.

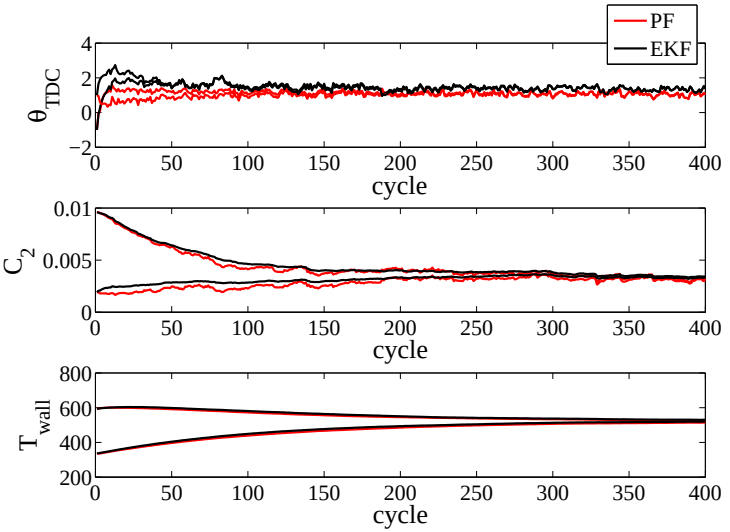

Figure 5.7 Filter convergence with 400 cycles of experimental data from the operating point presented in Table 5.3, the EKF (black) and the PF (red) have comparable performance but do converge to slightly different states estimates. Both filters manage to detect a significant top-dead-center offset of approximately 1 CAD.

For the choice of 250 particles the PF is slower than the EKF (see 5.3), but was less sensitive to model-parameter errors and with comparable RMSE in stationarity. The PF performance can of course be improved by increasing the particle amount, however 250 particles were chosen here so that the filters would have similar computation times. A deeper analysis of the trade-off between the number of particles, the resampling criterion and the PF performance was not carried out and is considered to be future work. The investigation presented in this chapter should rather be viewed as a feasibility check than a fair comparison between the filters.

It would of course be straightforward to extend this framework for the estimation of additional model parameters. Additional sensor information, for instance wall-temperature measurements could be included. The statistical model for Q_c could also be further developed, for instance by making monotonic Q_c more probable or by testing more realistic heat-release noise models, that could be obtained from experimental heat-release data.

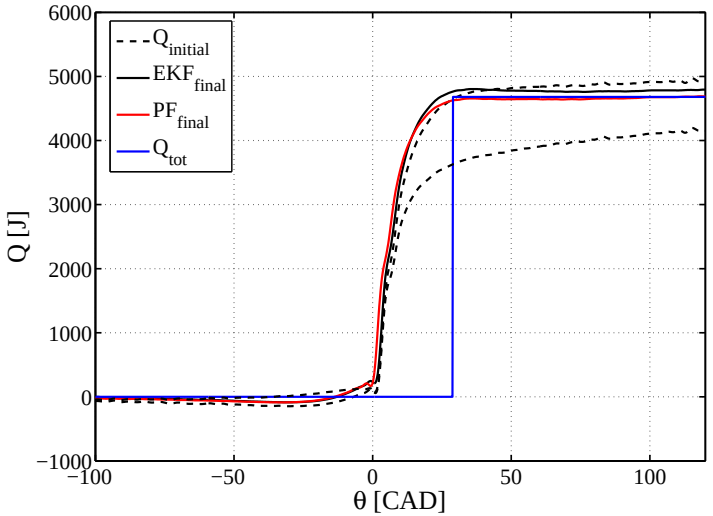

Figure 5.8 Filter Q_c-output convergence, from the cycles presented in Fig. 5.7, the EKF (black) and the PF (red) converges to slightly different accumulated heat-release levels from the initial Q_c outputs (black, dashed). The blue line indicates the estimated true Q_c level after combustion, computed from fuel flow measurements.

6

Ignition-Delay Model Evaluation

6.1 Introduction

Since the ignition delay, τ, is an important quantity in low temperature combustion concepts it is of interest to investigate its behavior from a controller-design perspective. By the use of an in-cylinder pressure sensor, the ignition delay could be controlled in closed-loop. In order to design model-based controllers for this purpose, accurate models of the ignition-delay behavior are needed, however, there is also a need for models with complexity suitable for real-time computations, with easily measurable quantities as inputs. In this chapter, the three different low-order physics-based correlation models M1, M2 and M3,

$$M1: \tau = Ae^{E_a/R\bar{T}}\overline{[O_2]}^{\alpha}\overline{[C_nH_m]}^{\beta}\bar{p}^{\gamma}S_p^{\delta}, \tag{6.1}$$

$$M2: \int_{\theta_{SOI}}^{\theta_{SOI}+\tau} Ae^{-E_a/RT}[O_2]^{\alpha}[C_nH_m]^{\beta}p^{\gamma}S_p^{\gamma}d\theta = 1, \tag{6.2}$$

$$M3: \begin{cases} \dfrac{d[C_nH_m]}{dt} & = -k_1[C_nH_m]^{\beta}[O_2]^{\alpha}, \\ \dfrac{d[O_2]}{dt} & = -(\dfrac{n}{2}+\dfrac{m}{4})k_1[C_nH_m]^{\beta}[O_2]^{\alpha} - k_2[CO][O_2]^{1/2}, \\ \dfrac{d[CO]}{dt} & = nk_1[C_nH_m]^{\beta}[O_2]^{\alpha} - k_2[CO][O_2]^{1/2}, \\ \dfrac{d[CO_2]}{dt} & = k_2[CO][O_2]^{1/2}, \\ k_i & = A_i e^{-E_a^i/RT}S_p^{\delta_i}, \\ \dfrac{dQ_c}{dt} & = V(Q_1k_1[C_nH_m]^{\beta}[O_2]^{\alpha} + k_2Q_2[CO][O_2]^{1/2}), \end{cases} \tag{6.3}$$

Table 6.1 Operating points used for model calibration and evaluation.

	L1S1	L2S1	L1S2	L2S2
Engine Speed [rpm]	1200	1200	1500	1500
p_{IMEPg} [bar]	5	10	5	10
Intake Temperature [C]	20-40	22-60	22-50	38-85
Cylinder [O_2] at IVC [mol/m^3]	7.5 – 9.5	9.5 – 11.5	7.5 – 10	8.5-13
Injection Timing [CAD]	-25 - (-5)	-10 - 2	-25 - 5	-15 – 0

that were presented in Chapter 2 are evaluated for the purpose of model-based τ controller design. Assuming that variations in the chemically controlled part of τ, the auto-ignition time, gives rise to the variability in τ, the models relate the cylinder-gas temperature T, pressure p, cylinder-gas composition and N_{speed} to τ. The evaluation is done by studying how well the models, when calibrated, could predict experimental τ behavior when injection timing, inlet temperature and oxygen concentration were varied in the lower load and speed range of the engine. The complexity of linearizing the different models for linear controller design is also investigated. The purpose of the evaluation of these models was to understand what level of model complexity is needed for good predictability of experimental data and if increased model complexity yields significant improvement that would allow for better model-based controller performance.

6.2 Ignition-Delay Experiments

Ignition-delay experiments were conducted at four operating points given from the possible combinations of p_{IMEPg} at 5, 10 bar and N_{speed} at 1200, 1500 rpm, see Table 6.1. A suitable injection timing was found at each operating point with no EGR and both thermal-management valves open at 45 degrees each. Let us denote these conditions the initial setting for each operating point. To investigate the ignition-delay response to different engine inputs, the injection timing, the thermal-management valves and the EGR valves were each changed manually in steps over the whole accessible range around the initial setting during a total of 12000 cycles at each operating point. The thermal-management valve angles θ_{Hot} and θ_{Cool} were changed by setting

$$\theta_{\text{Cool}} = \cos^{-1}(1 - \cos(\theta_{\text{Hot}})), \tag{6.4}$$

the inlet temperature was then changed by varying θ_{Hot} in order to keep an approximately constant total valve-opening area. The long-route EGR was used to change the EGR level at the higher load operating points while the short-route EGR was used at the lower load operating points. The resulting engine data can

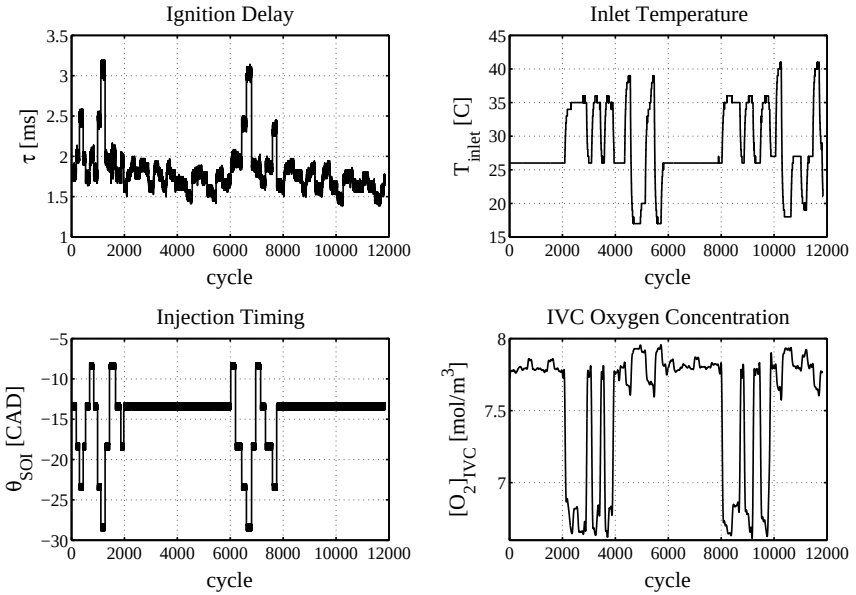

Figure 6.1 Experiment data at operating point L1S1, top left: τ [ms], top right: T_{inlet} [C], bottom left: θ_{SOI} [CAD ATDC] and bottom right: $[O_2]_{\text{IVC}}$ [mol/m^3].

be viewed in Figs. 6.1-6.4 where the inlet temperature T_{inlet}, cylinder oxygen concentration at IVC $[O_2]_{\text{IVC}}$, injection timing θ_{SOI} and τ for one of the six cylinders are plotted.

Half of the cycles τ^{ID} were then used for model calibration and the other half τ^{VAL} for model validation, this approach of evaluating model performance is called cross validation [Geisser, 1993].

6.3 Parameter Identification and Model Evaluation

In order to identify suitable model parameters ϑ_{M1-3}, a sum-of-squares model-error cost function $J_{Mx}(\tau^{\text{ID}}, \vartheta_{Mx})$ was minimized for each model with respect to the model parameters ϑ_{M1-3} given the identification data set τ^{ID}.

The procedures used for finding the minimizer ϑ^*_{Mx} for the different models are now presented.

Model 1

If logarithms are applied to both sides of Eq. (6.1), the problem of minimizing

$$J_{M1}(\vartheta_{M1}) = ||\ln(\tau^{\text{ID}}) - \ln(\tau^{M1})||_2^2 \tag{6.5}$$

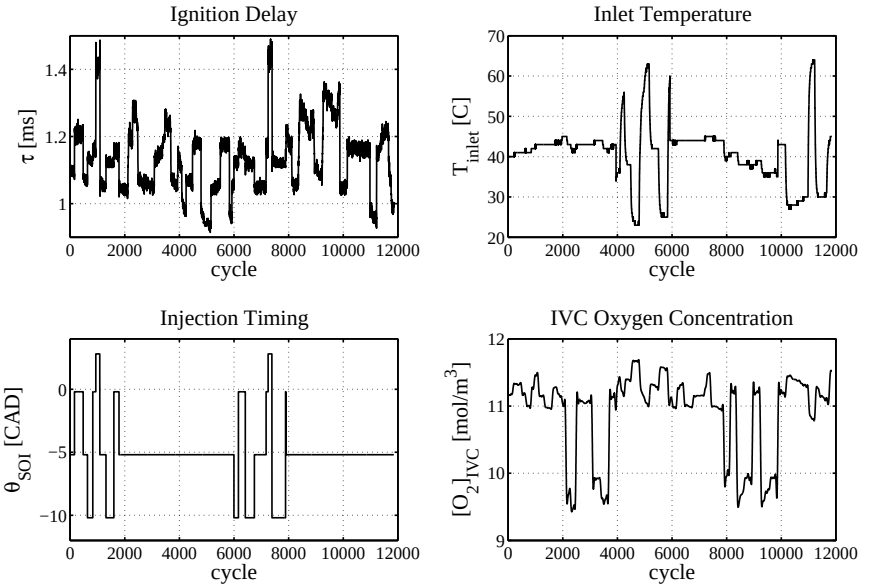

Figure 6.2 Experiment data at operating point L2S1.

w.r.t. ϑ_{M1} is on linear regression form. By introducing the parameters $y = \ln(\tau^{M1})$ and Φ,

$$\Phi = \begin{pmatrix} 1 & \frac{1}{R\bar{T}_1} & \ln(\overline{[\mathrm{O_2}]}_1) & \ln(\overline{[\mathrm{C_nH_m}]}_1) & \ln(\bar{p}_1) & \ln(\bar{S}_{p_1}) \\ \vdots & \vdots & \vdots & \vdots & \vdots & \vdots \\ 1 & \frac{1}{R\bar{T}_N} & \ln(\overline{[\mathrm{O_2}]}_N) & \ln(\overline{[\mathrm{C_nH_m}]}_N) & \ln(\bar{p}_N) & \ln(\bar{S}_{p_N}) \end{pmatrix} \tag{6.6}$$

the minimizer $\vartheta^* = \begin{pmatrix} \ln(A^*) & E_a^* & \alpha^* & \beta^* & \gamma^* & \delta^* \end{pmatrix}^T$ of $J_{M1}(\vartheta_{M1})$ is given by

$$\vartheta^* = (\Phi^T\Phi)^{-1}\Phi^T y. \tag{6.7}$$

The theory of solving linear-regression problems in the least-squares sense is described in more detailed in [Johansson, 1993].

Model 2

For the second model, the parameters were found by minimizing

$$J_{M2}(\vartheta_{M2}) = \sum_i \Big(\int_{\theta_{\mathrm{SOI}}}^{\theta_{\mathrm{SOI}}+\tau^{\mathrm{ID}}} A e^{-E_a/(RT_i)} [\mathrm{O_2}]_i^{\alpha} [\mathrm{C_nH_m}]_i^{\beta} p_i^{\gamma} \bar{S}_{p_i}^{\delta} \, dt - 1 \Big)^2 \tag{6.8}$$

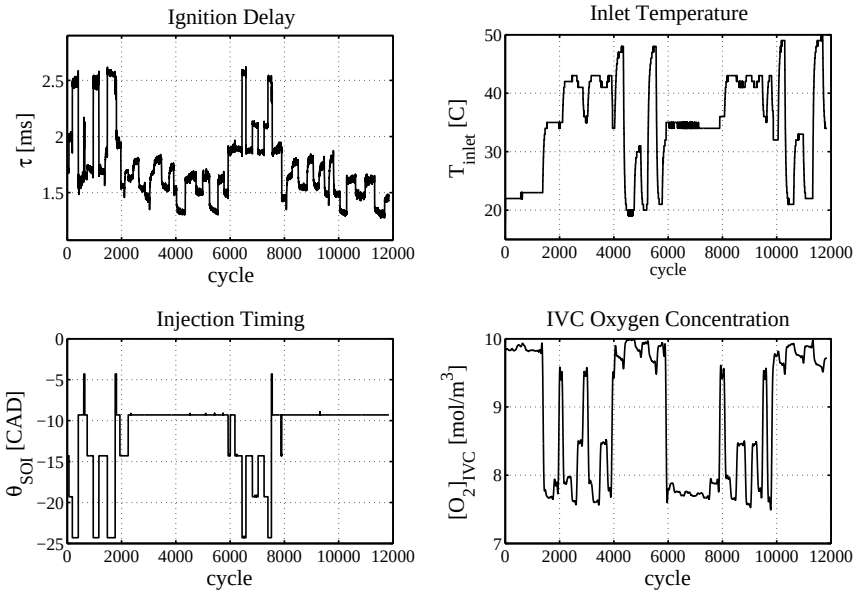

Figure 6.3 Experiment data at operating point L1S2.

where i is the cycle index. This problem is not of linear regression type and there is no closed form expression for the minimizer, therefore, one has to rely on numerical optimization algorithms. Here J_{M2} was solved using Matlab's Optimization Toolbox and the lsqcurvefit function which minimizes J_{M2} by evaluating the model output for arbitrary model parameters and then applies a trust-region-reflective least-squares algorithm [Coleman, 1996]. In order to avoid local minima, the optimization procedure was restarted with different initial parameters.

Model 3

The reaction-rate parameters of the third model were found using the same numerical procedure as for M2. In order to identify the model parameters, the system of chemical reactions was simulated by approximating the derivatives in Eq. (6.3) using the forward-Euler method with a sufficiently small step size h, in this work $h = 0.01$ ms was used. The model parameters were then found by minimizing

$$J_{M3}(\vartheta_{M3}) = \sum_i (Q_{c,i}^{M3}(\theta_{10}^{\mathrm{ID}}) - 0.1 Q_{c,i}^{\mathrm{tot}})^2. \tag{6.9}$$

Where $Q_c^{M3}(\theta_{10,i}^{\mathrm{ID}})$ is the model output heat released at $\theta_{10}^{\mathrm{ID}}$, and $Q_{c,i}^{\mathrm{tot}}$ is the estimated total heat released at cycle i, computed from the measured engine fuel-mass flow.

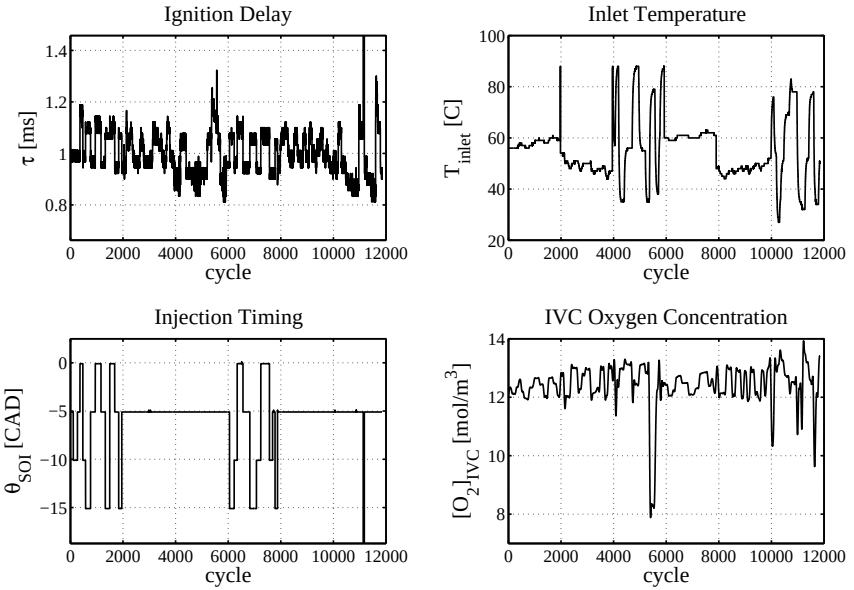

Figure 6.4 Experiment data at operating point L2S2, note the unintentionally early θ_{SOI} after cycle 11000, it was decided to be keep these cycles in the τ^{VAL} data set.

6.4 Model-Evaluation Results

Evaluation Procedure

The above presented models were evaluated by how well they could explain the variation in the validation-data set, τ^{VAL}, in two different ways:

- The models were evaluated by how well they could predict the ignition delay in each operating point separately, i.e., by how well a model calibrated by identification data from an operating point could predict data from the same operating point. During the model calibration the speed dependence were removed from the models ($\delta = 0$), the load dependence was also removed by setting $\beta = 0$ in M1-2 and $\beta = 1$ in M3. M1 and M2 were investigated with and without the pressure dependence, i.e with γ free and = 0.

- The models were evaluated by how well they could predict the ignition-delay behavior for all operating points, i.e, by how well a model calibrated by data from the complete identification data set could predict data from all operating points in the validation-data set. Now β and δ were set as free parameters in the parameter-identification procedure.

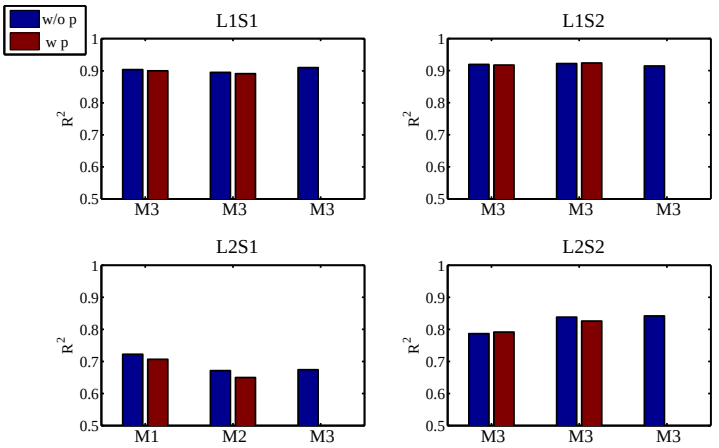

Figure 6.5 Model R^2 w.r.t. validation data, for M1, M2 and M3 for each operating point. Including p in the M1 and M2 does not give any improvement. Increasing model complexity from M1 to M2 and M3 does not necessarily yield higher R^2. It can also be seen that the R^2 scores are overall lower at the higher load operating points.

The reason for evaluating the models in these two ways was to investigate if there is an incentive for using multiple models with fewer parameters instead of having one model with more parameters that covers all operating points. The model performance was evaluated by using the R^2 statistic

$$R^2 = 1 - SS_{\text{err}}/SS_{\text{tot}}, \tag{6.10}$$

where SS_{err} is the sum-of-squares of the model τ output error, SS_{tot} is the sum-of-squares of the sampled data that is to be predicted, the ignition delay in the validation-data set τ^{VAL}. Since the model application is linear-model-based controller design, the models are to be linearized at any given engine operating point. It is thus more important for the models to predict the τ variation magnitude rather than the τ absolute value, therefore, the mean value of the predicted τ and τ^{VAL} was subtracted before computing R^2.

Individual Operating Points

The R^2 scores for each model when trained and validated for every operating point individually are presented in Figure 6.5, the red and blue bars indicate R^2 when p was included and excluded from M1 and M2. It can be seen that including p does not improve the model performance, it rather decreases the performance slightly. Increasing model complexity from M1 to M2 increases performance at L1S2 and L2S2 but not at L2S1 and L1S1. Going from M2 to M3 improves

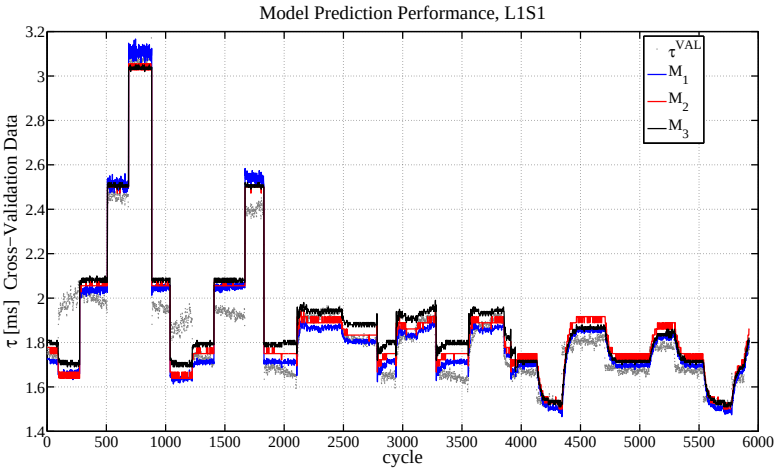

Figure 6.6 Model-predicted ignition delays together with τ^{VAL} from operating point L1S1. It can be seen that the models do not follow the data well after cycle 200 and 1000. M1 has overall comparable performance with M2 and M3.

model performance in all operating points but L1S2. It can also be seen that the R^2 scores are overall lower at the higher load operating points. For a more qualitative analysis, the model outputs are displayed together with τ^{VAL} in Figs. 6.6-6.9 where the grey dots are τ^{VAL} and the blue, red and black lines are model outputs from M1, M2 and M3, without pressure dependence in M1 and M2. In Fig. 6.6, the model outputs do not follow τ^{VAL} well around cycles 200 and 1100, this is when the injection timing is being retarded (see Fig. 6.3, cycles 6000, 6900), the same behavior is found in Fig. 6.7 from cycle 1 to 800, in Fig. 6.8, cycle 200 and Fig. 6.9, cycles 500, 1500. As the injection timing is delayed, closer to top-dead center, the estimated cylinder-gas temperature during τ increases which causes the models to predict a decreased τ, however τ^{VAL} instead starts to increase. This is a result of model incapability of anticipating the point where a retarded θ_{50} starts to give an increased τ, a similar model error can be seen in Fig. 6.2, cycle 1400 where a positive θ_{SOI} gave a much increased τ. The models are overall better at predicting τ^{VAL} during variations in T_{IVC}, $[\mathrm{O_2}]_{\mathrm{IVC}}$ and θ_{SOI} for early θ_{SOI}. The similar model ouputs in Figs. 6.6-6.9 indicate that controller designs based on the different models would yield comparable performance.

All operating points

Then, the models were calibrated by the complete identification-data set in order to see how well one model could predict the overall τ behavior. Now β and δ were set free in the parameter identification procedure for model M1-2, β and δ_1 were

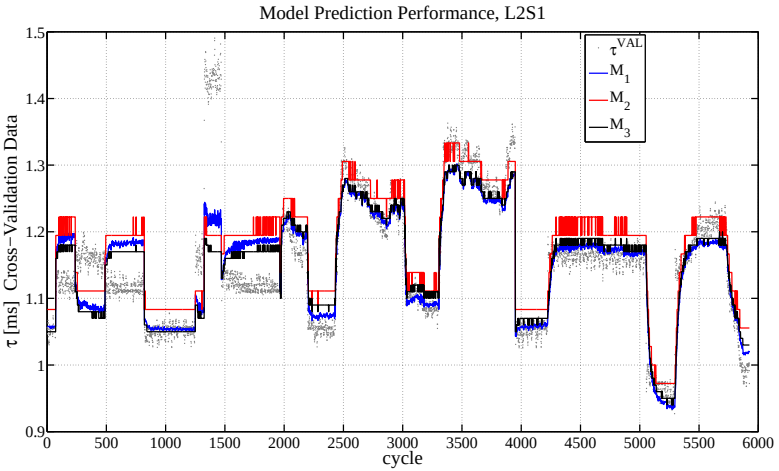

Figure 6.7 Model-predicted ignition delays together with τ^{VAL} from operating point L2S1.

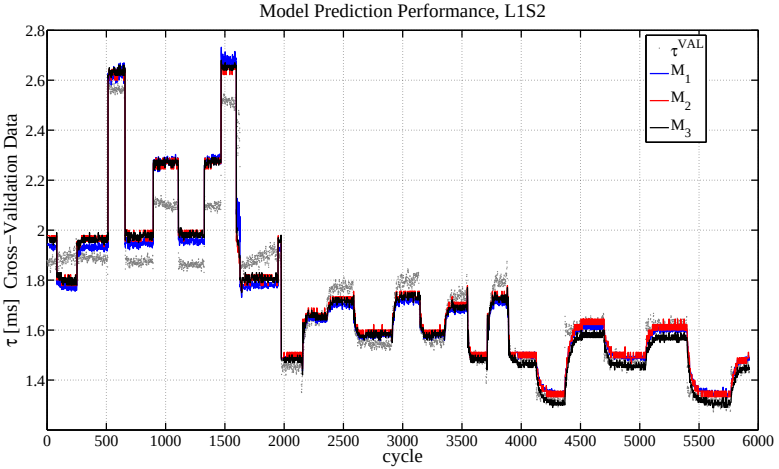

Figure 6.8 Model-predicted ignition delays together with τ^{VAL} from operating point L1S2.

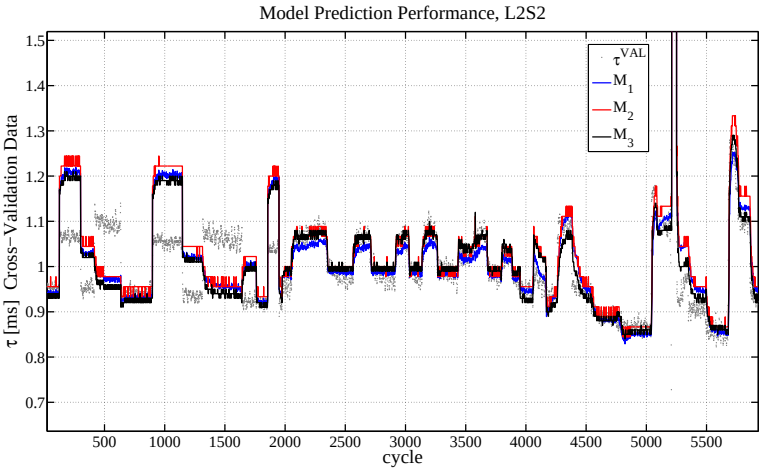

Figure 6.9 Model-predicted ignition delays together with τ^{VAL} from operating point L2S2.

set free in the parameter identification for M3. In Fig. 6.10, R^2 is presented for the various different models, the blue bars represent R^2 without p dependence in the model and the red bars with p dependence in M1-2. The yellow bars represent R^2 when using the individual operating point models presented in the previous section. Increased prediction performance can be obtained by switching between the different models instead of using one model for all operating points. In Fig. 6.11, the model-predicted τ is presented together with τ^{VAL}, it can be seen that M1 has comparable performance with M2 and M3.

6.5 Linearization for Control Purposes

For the purpose of using these models in model-based controller algorithms, it is of interest to linearize them w.r.t. to the system inputs T_{IVC}, $[\mathrm{O_2}]_{\mathrm{IVC}}$ and θ_{SOI} at an arbitrary operating point

$$X^0 = \begin{pmatrix} T^0_{\mathrm{IVC}} & [\mathrm{O_2}]^0_{\mathrm{IVC}} & \theta^0_{\mathrm{SOI}} \end{pmatrix}^T. \tag{6.11}$$

This yields a linear cycle-to-cycle model on the form

$$\tau_{k+1} = \tau_k + \frac{\partial \tau(X^0)}{\partial T_{\mathrm{IVC}}} \Delta T_{\mathrm{IVC}_k} + \frac{\partial \tau(X^0)}{\partial [\mathrm{O_2}]_{\mathrm{IVC}}} \Delta [\mathrm{O_2}]_{\mathrm{IVC}_k} + \frac{\partial \tau(X^0)}{\partial \Delta_{\mathrm{SOI}}} \Delta \theta_{\mathrm{SOI}_k}, \tag{6.12}$$

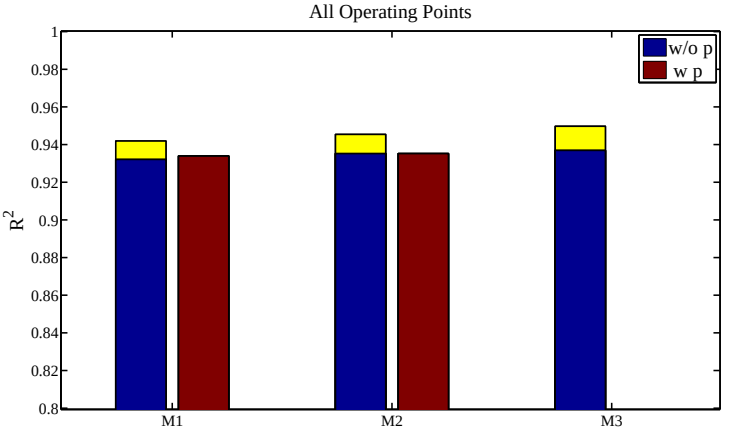

Figure 6.10 Model R^2 w.r.t. validation data. The yellow top indicates the R^2 increase when using the individual operation-point models on the complete identification-data set. Here, there is a slight improvement using p in M1-M2. Increasing the model complexity from M1 to M2 and M3 increases performance, also using individual operating point models gives an increased performance.

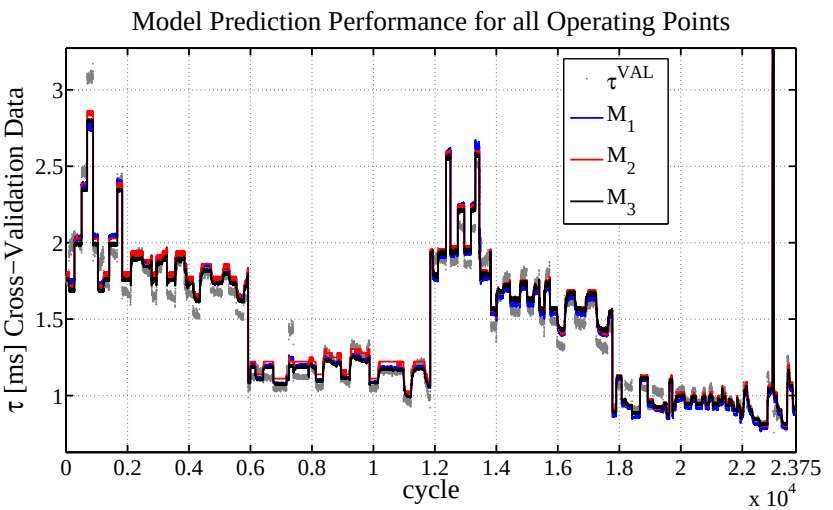

Figure 6.11 Model-predicted ignition delays together τ^{VAL} all operating points.

Table 6.2 Estimated complexity in arithmetic operations where addition, subtraction and multiplication are all considered to be one operation. N is the number of samples between θ_{SOI} and θ_{10}, τ/h is the ratio of the ignition delay and the step size used in the forward-Euler approximation, from the authors experience h should be smaller than 0.05 ms. * = number of operations assuming a crank angle resolution of 0.2 CAD, and 10 CAD ignition delay. ** = using ($\tau/h = 300$).

Model	Arithmetic Operations	Example
M1	$7N$	$(750)^*$
M2	$43N$	$(2150)^*$
M3	$105\tau/h$	$(31500)^{**}$

where Δ is the forward-shift operator. The linearization of M1, M2 and M3 could be carried out by approximating the partial derivatives numerically

$$\frac{\partial\tau(X^0)}{\partial X_k} \approx \frac{\tau(X^0 + \Delta X_k) - \tau(X^0)}{\Delta X_k}. \tag{6.13}$$

The computational complexity of Eg. (6.13) in terms of arithmetic operations for the different models are presented in Table 6.2. Addition, subtraction, multiplication and taking powers are here all considered to be one operation. In Table 6.2, N is the number of samples between θ_{SOI} and θ_{10}, τ/h is the ratio of the ignition delay and the step size h used in the forward-Euler approximation while simulating M3, from the author's experience h should be smaller than 0.05 ms. The values in Table 6.2 are by no means proved to be the most efficient implementation of Eq. (6.13), nevertheless, they originate from the author's implementation used in this work. The results show that M1 and M2 are superior in terms of complexity, at least if Eq. (6.13) should be computed every cycle in a controller algorithm.

6.6 Discussion

The models could not accurately detect the point when delaying θ_{SOI} close to TDC started to give an increased τ. If this was caused by errors in the estimated cylinder-gas state, errors in the heat-release analysis or by the fact that the models were too simple to capture the τ variation is not known. The models performed better when θ_{SOI} was varied earlier in the compression stroke and when T_{IVC} and $[O_2]_{IVC}$ were varied. This implies that it will be easier to obtain good model-based controller performance when controlling τ using T_{IVC}, $[O_2]_{IVC}$ and early θ_{SOI} when using these types of models. When comparing model performance, the results were unambiguous, in some cases it was worthwhile to increase model complexity (see L1S1, L2S2, Fig. 8.10). When studying Figs. 6.6-6.9, it could be seen that the model performance did not differ significantly in most

cases. When taking into account for the computational cost of linearization, M1 is superior to M2 and M3 (see Table 6.2). The fact that M1 also has an explicit expression (Eq. (6.7)) for calibration, this model seems to be the best choice for model-based controller design among the three investigated models.

When studying performance for all operating points simultaneously (see Fig. 6.11), the model performance increased with complexity, it was also clear that it was more beneficial to use four different models with one model for each operating point rather than having one global model.

Effects from cylinder-wall temperature, fuel vaporization, atomization and fuel-spray interaction with the combustion chamber walls were not included in these models. If carefully modelled, these effects could probably improve model performance where the above presented models fail, however, information from these effects were not easily accessible from the sensors available and therefore it would have been difficult to validate the assumptions of these effects.

7

Simultaneous Control of Ignition Delay and Combustion Phasing

7.1 Introduction

In low temperature combustion concepts such as partially premixed combustion, the ignition delay τ (Eq. 2.16) should be large enough in order to ensure sufficient fuel and air mixing before the start of combustion. It is also necessary that the combustion timing θ_{50} (Eq. 2.3) is sufficiently well phased for high thermal efficiency. Since the ignition delay and combustion timing are intimately coupled, the decoupling of these two quantities gives rise to an interesting multiple input, multiple output control problem where the control of the air system and the fuel injection system have to be combined. In a multi-cylinder engine this problem becomes underdetermined or uncontrollable with more outputs than inputs. In this chapter a model-based cycle-to-cycle closed-loop controller of the ignition delay and the combustion phasing is presented and experimentally evaluated. The controller design is based on the principle of model predictive control (MPC) which is a suitable design for multiple input/output systems with actuator constraints. Ignition delay and combustion phasing were extracted from cooled in-cylinder pressure sensors and controlled by manipulating injection timings, gas mixture temperature and exhaust-gas recirculation (EGR) ratio using a dual EGR-path system and a fast thermal-management (FTM) system, see Fig. 4.1.

7.2 Modeling

A physics based-correlation model was used to model the ignition-delay behavior whilst a calibrated static model was used to model the gains from the gas-system valve positions to the intake-manifold composition and temperature.

This section covers the description of these models and how they were used for controller design.

Ignition-Delay Model

The model M1, without the p dependence, presented in Chapter 2 was used to model τ,

$$\tau = Ae^{E_a/R\bar{T}}\overline{[O_2]}^{\alpha}, \tag{7.1}$$

where T was computed using the adiabatic compression relation

$$T = T_{IVC}(\frac{V_{IVC}}{V})^{\gamma-1}, \tag{7.2}$$

with γ given from Eq. (2.7). The oxygen concentration was computed as follows

$$[O_2] = \frac{[O_2]_{IVC}}{V} V_{IVC}, \tag{7.3}$$

where $[O_2]_{IVC}$ is the in-cylinder gas concentration at inlet-valve closing, consisting of oxygen coming from the air-mass flow, the EGR-mass flow and the residual gases, see Eq. (2.31). This gives the expression for τ, assuming constant engine speed

$$\tau = A\exp(\frac{E_a}{R\dfrac{\int_{\theta_{SOI}}^{\theta_{SOI}+\tau} T_{IVC}\left(\dfrac{V_{IVC}}{V(\theta)}\right)^{\gamma-1} d\theta}{\int_{\theta_{SOI}}^{\theta_{SOI}+\tau} d\theta}})\left(\frac{\int_{\theta_{SOI}}^{\theta_{SOI}+\tau} \dfrac{[O_2]_{IVC}}{V(\theta)} V_{IVC} d\theta}{\int_{\theta_{SOI}}^{\theta_{SOI}+\tau} d\theta}\right)^{\alpha}. \tag{7.4}$$

Model parameters for this model were found using the procedure presented in Chapter 6 at the operating points in Table 6.1.

Differentiation and Linearization Since Eq. (7.4) is an implicit relation in τ, the partial derivatives of τ with respect to θ_{SOI}, T_{IVC} and $[O_2]_{IVC}$ were approximated numerically while keeping τ in the right hand side of Eq. (7.4) constant

$$\begin{aligned}
\frac{d\tau}{d\theta_{SOI}} &\approx \frac{\tau(\theta_{SOI}+\Delta\theta_{SOI}/2)-\tau(\theta_{SOI}-\Delta\theta_{SOI}/2)}{\Delta\theta_{SOI}},\\
\frac{d\tau}{dT_{IVC}} &\approx \frac{\tau(T_{IVC}+\Delta T_{IVC}/2)-\tau(T_{IVC}-\Delta T_{IVC}/2)}{\Delta T_{IVC}},\\
\frac{d\tau}{d[O_2]_{IVC}} &\approx \frac{\tau([O_2]_{IVC}+\Delta[O_2]_{IVC}/2)-\tau([O_2]_{IVC}-\Delta[O_2]_{IVC}/2)}{\Delta[O_2]_{IVC}}.
\end{aligned} \tag{7.5}$$

The partial derivatives in Eq. (7.5) makes it possible to approximate the cycle-to-cycle relation from changes ΔT_{IVC}, $\Delta\theta_{SOI}$, $\Delta[O_2]_{IVC}$ to changes in τ and θ_{50} with

the linear system of equations

$$\tau_i^{k+1} = \tau_i^k + \begin{pmatrix} \frac{d\tau_i}{d\theta_{\mathrm{SOI}}^i} & \frac{d\tau_i}{dT_{\mathrm{IVC}}} & \frac{d\tau_i}{d[\mathrm{O_2}]_{\mathrm{IVC}}} \end{pmatrix}^T \begin{pmatrix} \Delta\theta_{\mathrm{SOI}_i}^k \\ \Delta T_{\mathrm{IVC}}^k \\ \Delta[\mathrm{O_2}]_{\mathrm{IVC}}^k \end{pmatrix}, \tag{7.6}$$

$$\theta_{50_i}^{k+1} = \theta_{50_i}^k + \Delta\theta_{\mathrm{SOI}_i}^k + \frac{d\theta}{dt} \begin{pmatrix} \frac{d\tau_i}{d\theta_{\mathrm{SOI}}^i} & \frac{d\tau_i}{dT_{\mathrm{IVC}}} & \frac{d\tau_i}{d[\mathrm{O_2}]_{\mathrm{IVC}}} \end{pmatrix}^T \begin{pmatrix} \Delta\theta_{\mathrm{SOI}_i}^k \\ \Delta T_{\mathrm{IVC}}^k \\ \Delta[\mathrm{O_2}]_{\mathrm{IVC}}^k \end{pmatrix},$$

where k is the cycle index and i the cylinder index, $d\theta/dt$ is crank angles per millisecond at the current engine speed and is needed here since τ and θ_{50} have different units.

Gas-System Model

The partial derivatives $dT_{\mathrm{IVC}}/d\theta_{\mathrm{Hot}}$, $d[\mathrm{O_2}]_{\mathrm{IVC}}/d\theta_{\mathrm{LR}}$ and $d[\mathrm{O_2}]_{\mathrm{IVC}}/d\theta_{\mathrm{SR}}$ are then estimated from the slopes in Fig. 2.1, from this the relation between the gas-system valve positions and system outputs τ and θ_{50} can be established and the cycle-to-cycle model can be rewritten according to

$$\tau_i^{k+1} = \tau_i^k + \begin{pmatrix} \frac{d\tau_i}{d\theta_{\mathrm{SOI}}^i} & \frac{d\tau_i}{d\theta_{\mathrm{Hot}}} & \frac{d\tau_i}{d\theta_{\mathrm{SR}}} & \frac{d\tau_i}{d\theta_{\mathrm{LR}}} \end{pmatrix}^T \begin{pmatrix} \Delta\theta_{\mathrm{SOI}i}^k \\ \Delta\theta_{\mathrm{Hot}}^k, \\ \Delta\theta_{\mathrm{SR}}^k \\ \Delta\theta_{\mathrm{LR}}^k \end{pmatrix}, \tag{7.7}$$

$$\theta_{50i}^{k+1} = \theta_{50i}^k + \begin{pmatrix} \frac{d\theta_{50i}}{d\theta_{\mathrm{SOI}i}} & \frac{d\theta_{50i}}{d\theta_{\mathrm{Hot}}} & \frac{d\theta_{50i}}{d\theta_{\mathrm{SR}}} & \frac{d\theta_{50i}}{d\theta_{\mathrm{LR}}} \end{pmatrix}^T \begin{pmatrix} \Delta\theta_{\mathrm{SOI}i}^k \\ \Delta\theta_{\mathrm{Hot}}^k \\ \Delta\theta_{\mathrm{SR}}^k \\ \Delta\theta_{\mathrm{LR}}^k \end{pmatrix}.$$

The complete linear state-space model can be written on more compact form

$$\begin{pmatrix} \theta_{50}^{k+1} \\ \tau^{k+1} \end{pmatrix} = A \begin{pmatrix} \theta_{50}^k \\ \tau^k \end{pmatrix} + B \begin{pmatrix} \Delta\theta_{\mathrm{SOI}}^k \\ \Delta\theta_{\mathrm{Hot}}^k \\ \Delta\theta_{\mathrm{SR}}^k \\ \Delta\theta_{\mathrm{LR}}^k \end{pmatrix} \tag{7.8}$$

where

$$\begin{pmatrix} \theta_{50}^{k+1} \\ \tau^{k+1} \end{pmatrix} = \begin{pmatrix} \theta_{50,1}^{k} & \dots & \theta_{50,6}^{k} & \tau_{1}^{k} & \dots & \tau_{6}^{k} \end{pmatrix}^{T}, \tag{7.9}$$

$$\Delta\theta_{\mathrm{SOI}}^{k} = \begin{pmatrix} \Delta\theta_{\mathrm{SOI},1}^{k} & \dots & \Delta\theta_{\mathrm{SOI},6}^{k} \end{pmatrix}^{T}, \tag{7.10}$$

$$B = \begin{pmatrix} \frac{d\theta_{50,1}}{d\theta_{\mathrm{SOI},1}} & \cdots & 0 & \frac{d\theta_{50,1}}{d\theta_{\mathrm{Hot}}} & \frac{d\theta_{50,1}}{d\theta_{\mathrm{SR}}} & \frac{d\theta_{50,1}}{d\theta_{\mathrm{LR}}} \\ \vdots & \ddots & \vdots & \vdots & \vdots & \vdots \\ 0 & \cdots & \frac{d\theta_{50,6}}{d\theta_{\mathrm{SOI},6}} & \frac{d\theta_{50,6}}{d\theta_{\mathrm{Hot}}} & \frac{d\theta_{50,6}}{d\theta_{\mathrm{SR}}} & \frac{d\theta_{50,6}}{d\theta_{\mathrm{LR}}} \\ \frac{d\tau_1}{d\theta_{\mathrm{SOI},1}} & \dots & 0 & \frac{d\tau_1}{d\theta_{\mathrm{Hot}}} & \frac{d\tau_1}{d\theta_{\mathrm{SR}}} & \frac{d\tau_1}{d\theta_{\mathrm{LR}}} \\ \vdots & \ddots & \vdots & \vdots & \vdots & \vdots \\ 0 & \cdots & \frac{d\tau_6}{d\theta_{\mathrm{SOI},6}} & \frac{d\tau_6}{d\theta_{\mathrm{Hot}}} & \frac{d\tau_6}{d\theta_{\mathrm{SR}}} & \frac{d\tau_6}{d\theta_{\mathrm{LR}}} \end{pmatrix}, \tag{7.11}$$

$$A = I_{12x12}. \tag{7.12}$$

The rank of the controllability matrix of this linear system is not full, (this is easily realized since A is the identity matrix) which means that all outputs cannot be controlled independently. The control strategy used here was to let θ_{50} be controlled accurately with θ_{SOI} while the mean τ was controlled with θ_{Hot}, θ_{SR}, θ_{LR}, of course, the reversed approach also could be chosen.

7.3 MPC

Since the system in Eq. (7.8) is linear with multiple inputs and outputs with interaction and input constraints, the MPC framework was chosen, see Chapter 3 for a brief description. For this control problem, the cost function J was defined accordingly

$$\begin{aligned} J = &\sum_{k=1}^{H_p} \omega_1 ||r_{\theta 50}(k) - \theta_{50}(k)||_2^2 + \omega_2 ||r_{\tau}(k) - \tau(k)||_2^2 \\ &+ \sum_{k \epsilon k_{H_c}} \omega_3 ||\Delta\theta_{\mathrm{SOI}}(k)||_2^2 + \omega_4 \Delta\theta_{\mathrm{Hot}}(k)^2 + \omega_5 \Delta\theta_{\mathrm{SR}}(k)^2 \\ &+ \omega_6 \Delta\theta_{\mathrm{LR}}(k)^2 + \omega_7 \theta_{\mathrm{SR}}(k)^2 + \omega_8 \theta_{\mathrm{LR}}(k)^2, \end{aligned} \tag{7.13}$$

where the k is the cycle index, and $||\cdot||_2$ is the Euclidian norm in $\mathbb{R}^6$.

Table 7.1 The chosen MPC weights and constraints.

ω_1	ω_2	ω_3	ω_4
10^2	10^4	0.1	10^{-2}
ω_5	ω_6	ω_7	ω_8
600	400	3000	3000
$3 \leq \theta_{SR} \leq 40$	$20 \leq \theta_{LR} \leq 50$	$5 \leq \theta_{Hot} \leq 85$	$-40 \leq \theta_{SOI} \leq 10$

The two terms in the first sum penalize θ_{50} and τ set-point tracking error where $r_{\theta 50}$ and r_τ are the set points. The first four terms in the second sum penalize control action and the last two terms penalize the absolute value of θ_{SR} and θ_{LR}. Since the EGR-valve opening area decreases the turbine enthalpy and therefore decreases gas-exchange efficiency, it could be worthwhile to penalize the absolute EGR-valve positions, ω_i are all positive cost weights which decide the controller priorities.

The minimization of Eq. (7.13) is done subject to the modeled system dynamics in Eq. (7.8) and the absolute constraints on the inputs

$$l_b \leq \begin{pmatrix} \theta_{SOI} \\ \theta_{Hot} \\ \theta_{SR} \\ \theta_{LR} \end{pmatrix} \leq u_b. \tag{7.14}$$

MPC Design and Implementation

In order for the controller to overlook the slowest time constants of the gas system H_p was set equal to 50 cycles. The inputs were allowed to change unequidistantly at samples $k \in k_{Hc}$ over the control horizon in order to decrease the number of variables in the optimization problem, thus allowing for shorter computation times, see Fig. 7.1. The relation between the weights ω_{1-2} and ω_{3-6} determines the trade-off between θ_{50} and τ tracking performance and controller sensitivity to cycle-to-cycle variation and model error. The weights ω_{4-6} determine how fast the valve positions are allowed to change. Since there are physical limitations in their change rates and how fast they affect the intake gas state, these weights have to be chosen accordingly. Choosing ω_{7-8} is a trade-off between the ability to supply EGR for an increased ignition delay and gas-exchange efficiency. Choosing the input bounds l_b and u_b for the EGR valve positions was an interesting problem, in order to stay in the high-gain region, the bounds were chosen so that the $[O_2]_{IVC}$ slope was non-zero (see Figure 2.1), the other bounds was chosen to fulfill physical limits. The chosen weights and constraints are presented in Table 7.1. Minimizing Eq. (7.13) subject to the constraints in Eqs. (7.14-7.8) is a quadratic program (QP) and was solved in LabVIEW using the built-in QP active-set solver

VI. In order to shorten the computational time, the solver was allowed to use the previous solution and active set as initial guess. Early termination was also used in order to allow the solver to finish within 50 ms, these are well known methods for speeding up MPC execution [Wang and Boyd, 2010]. Average computational time for differentiating Eq. (7.4) and constructing the QP matrices was 10 ms while it took 25 ms on average to solve the QP. This was done every two engine revolutions after the pressure traces of the latest cycle for each cylinder were sampled. Solution trajectories with the weights in Table 7.1 are presented in Fig. 7.1. The dashed black lines in the upper part of Fig. 7.1 are the set points r_τ and $r_{\theta_{50}}$. The cylinder numbers are indicated in the legend below the figure, cylinder 1 being the leftmost cylinder in Fig. 4.1.

7.4 Results

Experimental results at stationary conditions and during load and speed changes are presented in this section. At stationary conditions, θ_{50} and τ were set to track set-point step changes. During load and speed changes the controller objective was to maintain constant θ_{50} and τ according to a predefined set point. The load was changed by varying the injection durations while keeping the common-rail pressure constant at 800 bar. During the load changes, p_{IMEPn} and the common-rail pressure level were controlled using PID controllers and pre-calibrated feed-forward signals. Engine-speed ramps were performed by changing the engine-brake motor-speed set point.

Set Point Tracking

In Fig. 7.2, system inputs and outputs are displayed during 1500 cycles when step changes in $r_{\theta_{50}}$ were made. The weights (see Table 7.1) were set so that the tracking of θ_{50} was done by changing the injection timings, τ was then controlled by the gas system in the mean sense. When the combustion phasing is retarded around cycle 950, τ is decreased due to increased temperature at θ_{SOI}. This forces the hot valve to close while the EGR valves open, the controller tries to find the lowest possible θ_{SR} in stationarity for higher turbine enthalpy. A zoom-in around cycle 950 can be seen in Fig. 7.3. In Fig. 7.4, system inputs and outputs are displayed during 2000 cycles for which step changes in r_τ were made. The tracking of r_τ were done by varying the EGR and FTM valve positions. When r_τ increases, the EGR valves and the cool FTM valve open. The short-route EGR valve opens too much initially which gives a slight overshoot in the mean τ. A zoom-in around cycle 550 is presented in Fig. 7.5, here it can be seen that the injection timings are varied to keep θ_{50} constant and it is kept within 0.6 CAD deviation while τ reaches its new set point after 50 cycles.

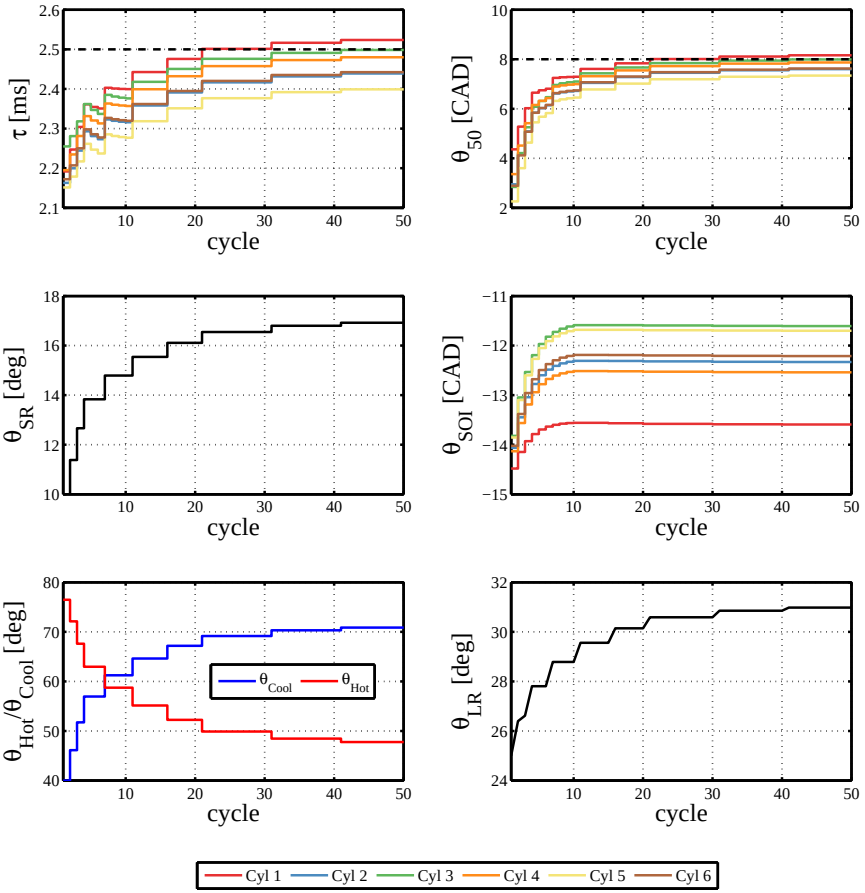

Figure 7.1 Solution trajectories using the weights in 7.1. The inputs are allowed to change at predefined cycle indices over H_c. The weights were chosen to prioritize the combustion-phasing tracking, while letting the slower gas system control the mean ignition delay. Note that the grid over which the injection timings are allowed to change is denser initially than for the gas system valves, this is because the control action of the injection timings is much faster than for the valve positions.

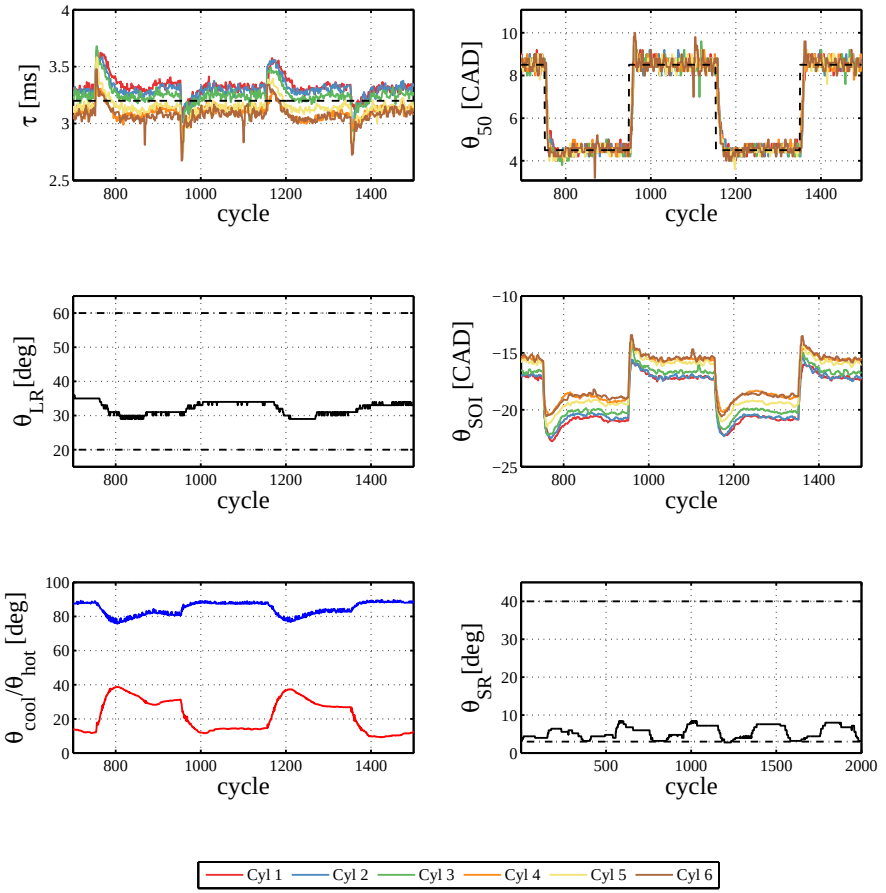

Figure 7.2 System inputs and outputs during 1500 cycles when steps in $r_{\theta_{50}}$ were made. θ_{Hot} is plotted in red and θ_{Cool} in blue, the black dashed lines in the upper graphs are the θ_{50} and τ set points while the dash-dotted lines are $\theta_{\text{LR}}/\theta_{\text{SR}}$ constraints. The weights were set so that the tracking of θ_{50} was done by changing the injection timings, the mean τ was then controlled by the gas system.

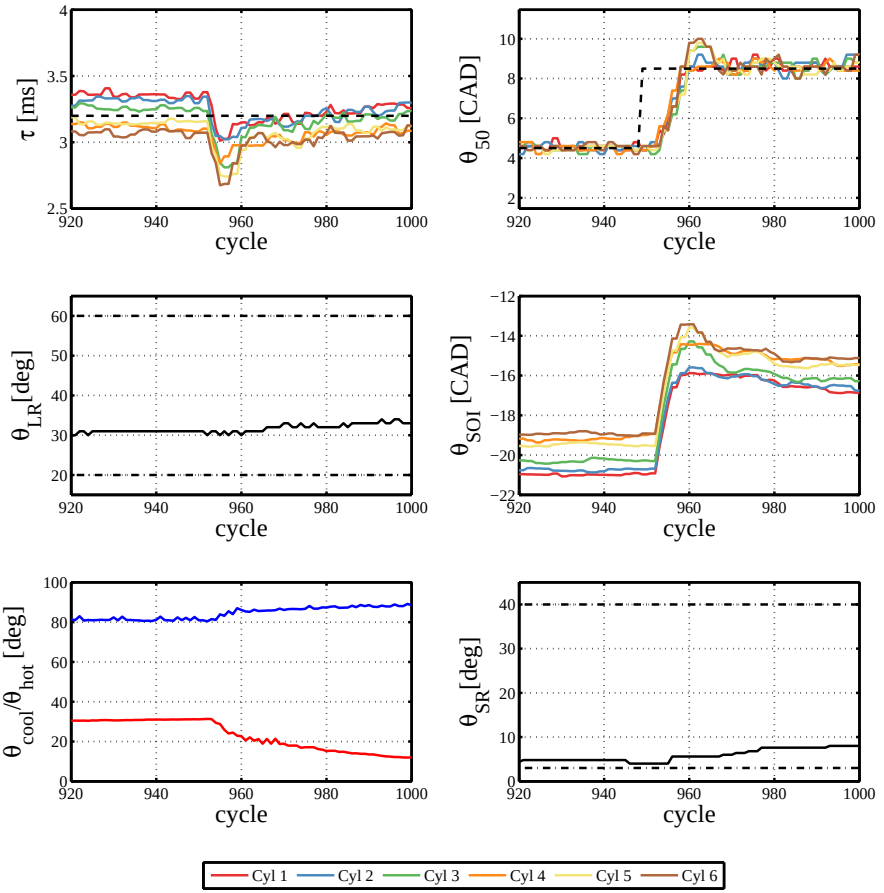

Figure 7.3 A zoom in around cycle 960 in Fig. 7.2, θ_{50} reaches its new set point after 5 cycles, there is also an internal delay from the set point to the controller of about 5 cycles. The gas system manages to adjust for the τ decrease in 60 cycles.

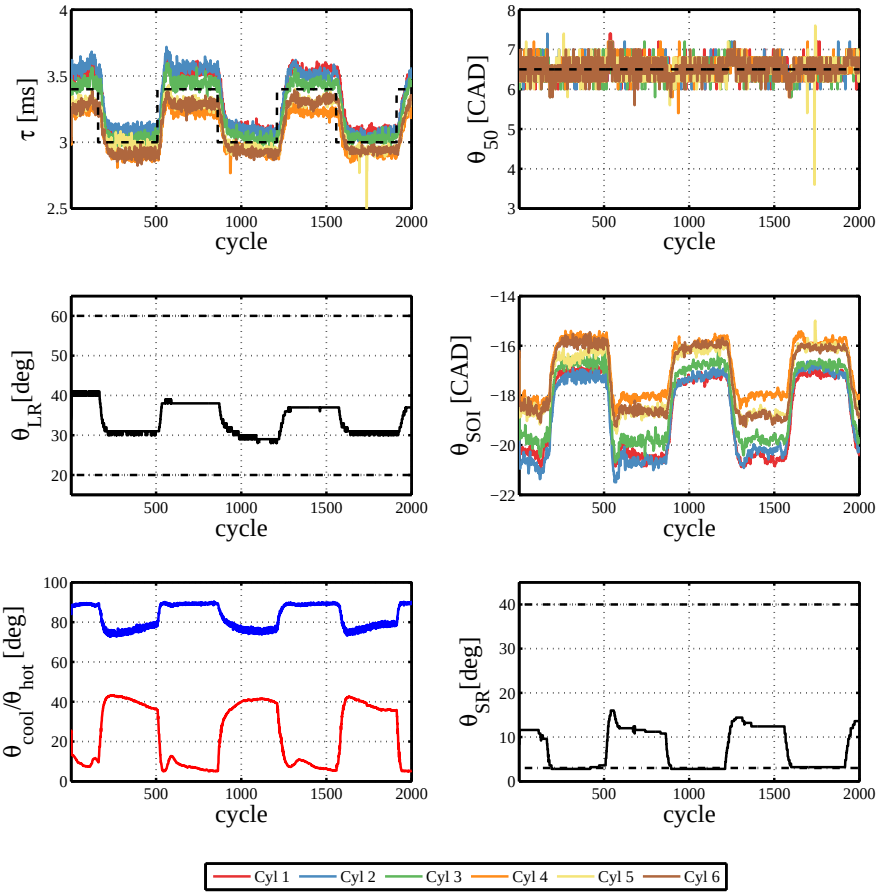

Figure 7.4 System inputs and outputs during 2000 cycles for which steps in r_τ are made. The tracking of r_τ were done by varying the EGR and FTM valve positions while the injection timings are varied to keep θ_{50} constant. Around cycle 1750 the ignition delay of cylinder 5 is suddenly shortened 0.5 ms for 2 cycles without any preceding changes in the actuating signals, the reason for this sudden change is unknown.

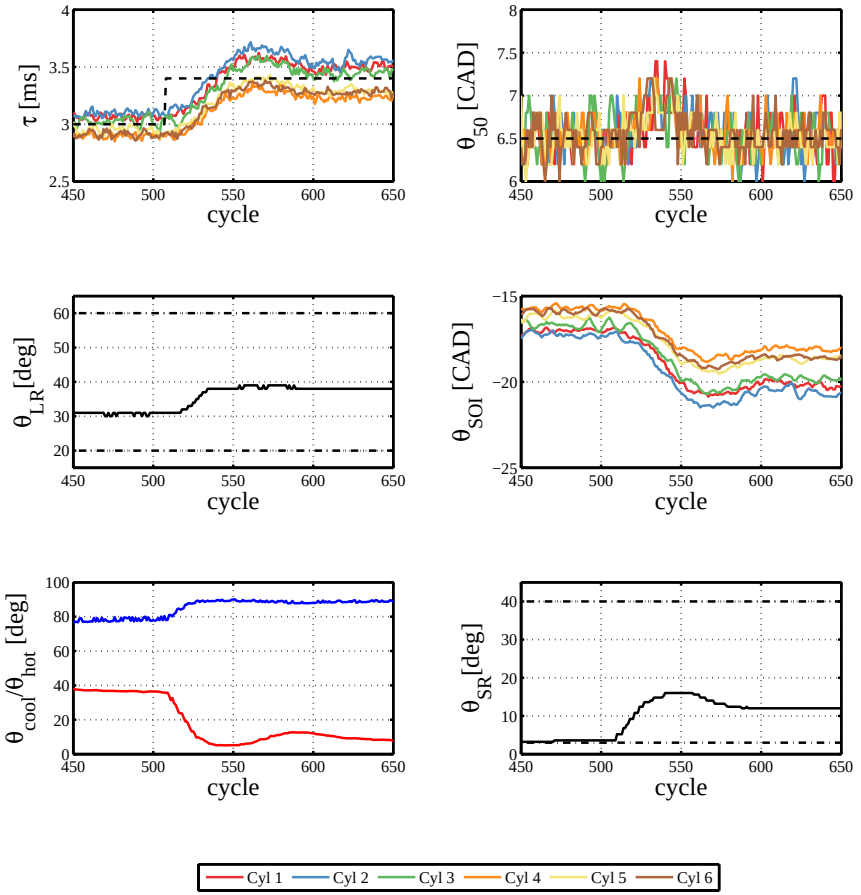

Figure 7.5 A zoom in around cycle 550 in Fig. 7.4, τ reaches its new set point after 50 cycles. The injection timings kept θ_{50} within 0.6 CAD during the step.

Load Step Changes

In Fig. 7.6, system inputs and outputs are displayed during 1000 cycles for which steps between 6 and 10 bar in $r_{p_{\mathrm{IMEPn}}}$ are made, p_{IMEPn} reaches its new set point in 20 cycles after every step change. As p_{IMEPn} is increased, τ is decreased due to increased cylinder temperatures and richer cylinder mixtures [Heywood, 1988], this forces the EGR valves to open. The FTM system is limited to the cold-flow upper limit during the experiment for the higher p_{IMEPn} values, θ_{SOI} manages to keep θ_{50} within 1 CAD deviation.

Speed Ramp Changes

In Figure 7.7, system inputs and outputs are displayed during 2000 cycles for which the engine speed was varied between 1200 and 1500 rpm. As the speed is increased, τ decreases, probably due to increased cylinder-gas turbulence levels [Heywood, 1988], this forces the EGR valves to open. The FTM system is limited to the cold-flow limit during the higher speeds, θ_{SOI} manages to keep θ_{50} within 1 CAD deviation from the set-point value.

7.5 Discussion and Conclusions

The controller was successful in tracking τ and θ_{50} set points both during stationary conditions and load and speed variations. It was found that the MPC tuning procedure was a trade-off between speed and sensitivity to model-errors and cycle-to-cycle variation. If the control action weights were to be decreased, the control action would increase but it was then more likely that the system outputs would overshoot during set-point changes, something that is probably caused by insufficient model prediction performance. In this work, the controller was tuned to give slow but reliable performance, the slow behavior can be seen in Fig. 7.4 where the gas system slowly increases τ.

The gas-system model used in this work was limited since only the static relation between valve positions and the inlet manifold gas state in a small operating range was included in the model. A dynamic model of the valve actuators and the gas system which includes turbocharger effects could give the controller information on how fast the control action would affect the system behavior which in turn could yield better performance. Incorporating a more detailed physics-based gas-system model into this controller framework is considered to be future work. The MPC framework yielded a simple way of prioritizing system output behavior, it also took system interaction effects into account. Input constraints and the cost of using EGR was also incorporated in the controller. Comparable controller performance could probably be obtained by using decentralized controllers for instance by letting θ_{50} be controller by the injection timings locally and then let the mean τ be controlled by the gas-system valve positions, similar to what was presented in [Karlsson et al., 2008]. This would demand less on-

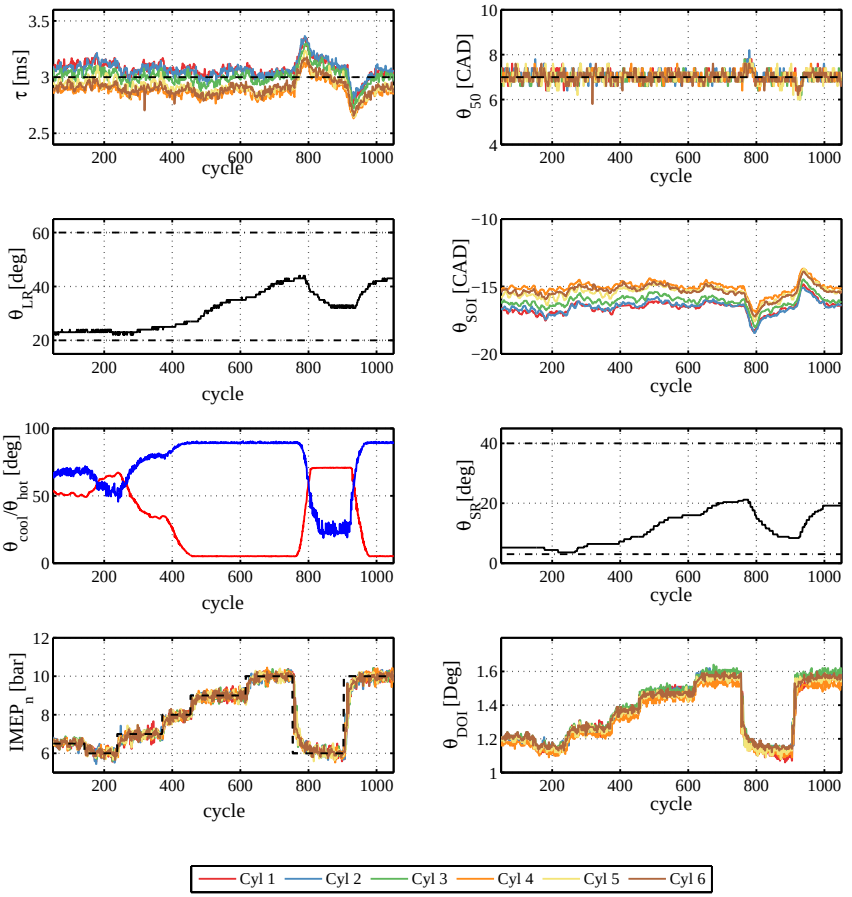

Figure 7.6 System inputs and outputs during 1000 cycles for which steps in $r_{p_{\mathrm{IMEPn}}}$ are made. In addition to the signals displayed in the previous figures, p_{IMEPn} is plotted together with its set point in the lower left figure, the injection durations θ_{DOI} are presented in the lower right figure.

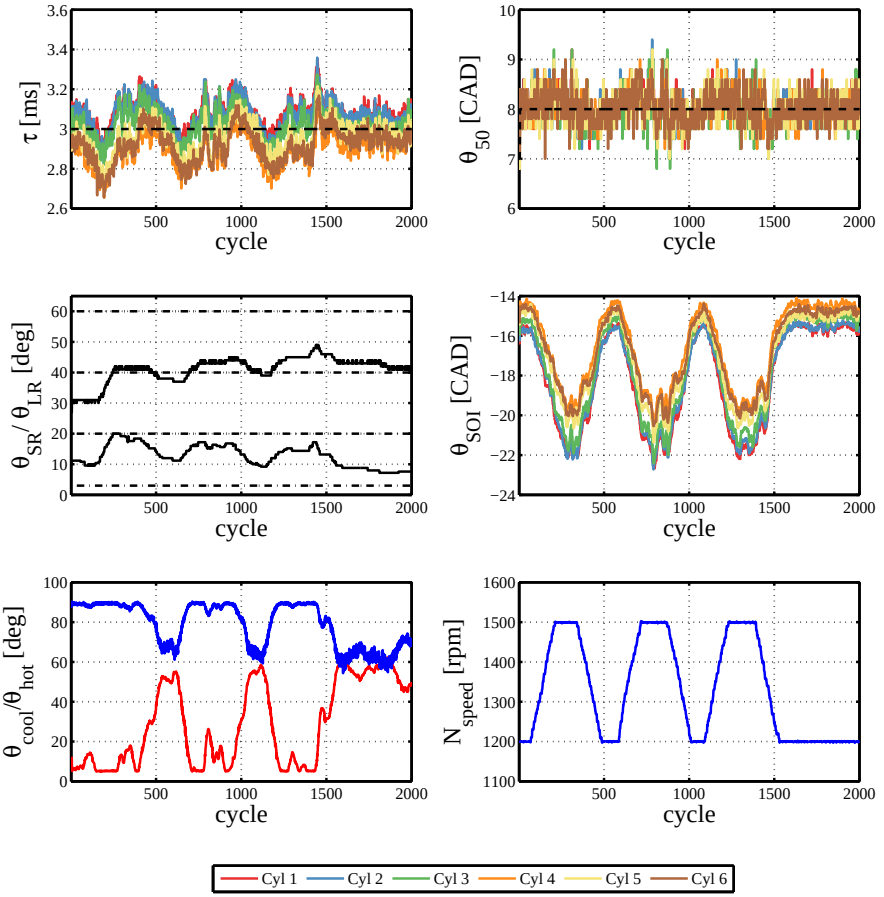

Figure 7.7 System inputs and outputs are displayed during 2000 cycles for which the engine speed is being varied. Both EGR-valve positions are now plotted together in the mid-left figure.

line computations, however, the framework presented here is more general. The model could also be extended to cover load control by means of injected fuel amount and its effect on τ, then, this would also be included in the prediction to yield better performance during load transients. The MPC framework could of course also be extended to cover high-level performance measures such as emission levels and efficiency instead of set-point tracking, this would however an extended engine model with more states.

A sufficient ignition delay was here considered to be a marker for a low temperature combustion mode with favorable emission properties. In future work this controller design will be evaluated with emission measurements to conclude that this hypothesis holds or if supplementary control actions need to be taken in order to fulfill emission constraints.

8

Pressure Prediction and Efficiency Optimization using Heat-Release Analysis

8.1 Introduction

During the compression and expansion strokes, the in-cylinder pressure changes with crank angle as a result of volume change, combustion and heat transfer. Both the combustion rate and phasing relative to top-dead center (TDC) affects the in-cylinder pressure and in turn the engine-work output [Heywood, 1988]. Ideally, the combustion phasing should be set to minimize the specific fuel consumption such that constraints on cylinder pressure, noise and emissions are fulfilled. Assuming that such a combustion phasing exists, it would vary with operating conditions, moreover, the injection timing for ideal combustion timing would also vary with operating conditions [Kiencke and Nielsen, 2012; Eriksson and Nielsen, 2014]. Traditionally, the way to decide injection timing is to experimentally calibrate the most favorable injection timing for each operating point and then use this setting in open-loop operation. This might however be sensitive to drift, especially in more sensitive combustion modes as shown by [Olsson et al., 2000], the approach also demands extensive experimental work. Combustion-timing closed-loop control strategies could be divided into two subgroups, those that aim to control the combustion timing to follow a predefined combustion-timing set point. Or those that aim to optimize engine performance subject to the combustion timing. Examples of the former were investigated by [Bengtsson et al., 2004], where quantities such as crank angle for 50 % heat released, θ_{50}, crank angle for maximum pressure and crank angle for maximum heat-release rate among others were used as feedback signals that indicate combustion timing. Closed-loop tracking of θ_{50} was obtained using physics-based auto-ignition models in [Blom et al., 2008; Widd et al., 2008; Shaver et al., 2004] and [Willems et al. 2010], to mention a few. [Nakayama et al., 2008] designed

a model-based feed-forward set-point controller. However, the problem of deciding the optimal combustion-timing set point still remains unsolved by using these controllers alone. In [Karlsson et al., 2010] it was showed that dynamical black-box models that relate injection timing to indicated mean effective pressure, max pressure derivative and NO_x emissions could be identified and used for model predictive control in order to minimize the specific fuel consumption subject to emission and pressure constraints. An extremum-seeking controller was designed by [Lewander, Widd et al. 2012] to find the combustion timing for the lowest specific fuel consumption with the use of θ_{50} feedback control in a CI engine, similar controllers were investigated by [Hellström et al 2013], and [Killingsworth et al. 2009] in SI and HCCI engines respectively.

This chapter presents a model-based cycle-to-cycle combustion-timing controller that aims to maximize the gross indicated mean effective pressure subject to cylinder-pressure constraints.

8.2 The Combustion-Timing Controller

The controller computation of the injection timing for the next engine cycle, given the current-cycle cylinder pressure can be summarized in three steps.

I Estimation of the heat-release rate of the current cycle, using Eq. (2.2).

II Prediction of the cylinder pressure due to a crank angle shifts of the estimated heat release rate.

III Computation of a shift in injection timing by solving an optimization problem based on the predicted cylinder pressure obtained in step II.

Steps II and III are presented in the following sections.

Pressure Prediction

After estimating $dQ_c/d\theta$ using Eq. (2.2), the objective is to predict the pressure change due to a change in the combustion timing. It is assumed that the pressure change due to a change in combustion timing in the next cycle is equivalent to the effect of a static crank-angle shift of the heat-release rate in the current cycle $dQ_c^0/d\theta$. This assumption relies on weak cycle-to-cycle dynamics of the combustion event and that the heat-release rate shape is not changing too much with smaller changes in combustion timing. First, $dQ_c^0/d\theta$ is shifted back and forth with crank angle $\Delta\theta$

$$\begin{aligned} \frac{dQ_c^+}{d\theta} &= \frac{dQ_c^0(\theta+\Delta\theta)}{d\theta}, \\ \frac{dQ_c^-}{d\theta} &= \frac{dQ_c^0(\theta-\Delta\theta)}{d\theta}. \end{aligned} \tag{8.1}$$

Pressure traces p^+ and p^- corresponding to $dQ_c^+/d\theta$ and $dQ_c^-/d\theta$ are then computed by first linearizing Eq. (8.2) w.r.t. p at the current cycle pressure p^0, heat-release rate $dQ_c^0/d\theta$ and T_w

$$\frac{dp}{d\theta} = -\frac{\gamma}{V}\frac{dV}{d\theta}p + \frac{\gamma-1}{V}\left(\frac{dQ_c}{d\theta} - h_c A\left(\frac{pVT_{\mathrm{IVC}}}{p_{\mathrm{IVC}}V_{\mathrm{IVC}}} - T_w\right)\right). \tag{8.2}$$

here γ was computed using Eq. (2.7). Denoting the nonlinear term in the heat transfer model

$$\mu(p,\theta) = (\gamma-1)\frac{h_c A T_{\mathrm{IVC}}}{p_{\mathrm{IVC}}V_{\mathrm{IVC}}}p, \tag{8.3}$$

the linearized system is given by Eq. (8.4) where Δp is the first order deviation from p^0

$$\frac{d\Delta p}{d\theta} = -\frac{\gamma}{V}\frac{dV}{d\theta} + \frac{d\mu(p^0,\theta)}{dp}\Delta p + \frac{\gamma-1}{V}\frac{d\Delta Q_c}{d\theta}, \tag{8.4}$$

p^+ and p^- are then given by $\Delta p + p^0$ where Δp is computed with Eq. (8.4) where

$$\begin{aligned}\frac{d\Delta Q_c}{d\theta} &= \frac{dQ_c^+}{d\theta} - \frac{dQ_c^0}{d\theta},\\ \frac{d\Delta Q_c}{d\theta} &= \frac{dQ_c^-}{d\theta} - \frac{dQ_c^0}{d\theta}.\end{aligned} \tag{8.5}$$

The reason for linearizing the system is that Δp is given by the expression

$$\Delta p(\theta) = \int_{\theta_{\mathrm{IVC}}}^{\theta} \Phi(\theta,\vartheta)\Gamma(\vartheta)\frac{d\Delta Q_c(\vartheta)}{d\vartheta}d\vartheta \tag{8.6}$$

where

$$\begin{aligned}\Phi(\theta,\vartheta) &= \exp\left(-\int_{\vartheta}^{\theta}\frac{d\mu(p^0,\tau)}{dp}d\tau\right)\left(\frac{V(\vartheta)}{V(\theta)}\right)^{\gamma},\\ \Gamma(\vartheta) &= \frac{\gamma-1}{V(\vartheta)},\end{aligned} \tag{8.7}$$

which makes Δp cheap to compute.

Injection-Timing Shift Optimization

With the computed predicted pressures p^+ and p^-, quantities such as indicated gross mean effective pressure p_{IMEPg} (from now on denoted p_{IMEP}, for ease of notation), max pressure $p_{\max}$ and max pressure derivative $dp_{\max}$ can be predicted

Algorithm 4 Controller Algorithm

1: **while** $k > 0$ **do**
2: Estimate $dQ_c^0/d\theta$ using the measured p^0 at cycle k and Eq. (2.2).
3: Shift $dQ_c^0/d\theta$ according to to Eq. (8.1).
4: Compute p^+ and p^- using Eq. (8.6).
5: Compute the gradients in Eq. (8.9), and solve Eq. (8.11).
6: Set $\theta_{\mathrm{SOI}}^{k+1} = \theta_{\mathrm{SOI}}^{k} + \Delta\theta_{\mathrm{SOI}}^{*}$.
7: **end while**

$$
\begin{aligned}
p^+_{\mathrm{IMEP}} &= 1/V_d \int_{V_{\mathrm{IVC}}}^{V_{\mathrm{EVO}}} p^+ dV, \\
p^-_{\mathrm{IMEP}} &= 1/V_d \int_{V_{\mathrm{IVC}}}^{V_{\mathrm{EVO}}} p^- dV, \\
p^+_{\mathrm{max}} &= \max_{\theta} p^+, \\
p^-_{\mathrm{max}} &= \max_{\theta} p^-, \\
dp^+_{\mathrm{max}} &= \max_{\theta} dp^+, \\
dp^-_{\mathrm{max}} &= \max_{\theta} dp^-.
\end{aligned}
\tag{8.8}
$$

Moreover, the estimated derivatives of these quantities with respect to the combustion timing crank angle shift $\Delta\theta$ can be computed

$$
\begin{aligned}
\frac{dp_{\mathrm{IMEP}}}{d\Delta\theta} &= \frac{p^+_{\mathrm{IMEP}} - p^-_{\mathrm{IMEP}}}{2\Delta\theta}, \\
\frac{dp_{\mathrm{max}}}{d\Delta\theta} &= \frac{p^+_{\mathrm{max}} - p^-_{\mathrm{max}}}{2\Delta\theta}, \\
\frac{d(dp_{\mathrm{max}})}{d\Delta\theta} &= \frac{dp^+_{\mathrm{max}} - dp^-_{\mathrm{max}}}{2\Delta\theta}.
\end{aligned}
\tag{8.9}
$$

With the gradients in Eq. (8.9) a simple prediction model for p_{IMEP}, p_{max} and dp_{max} in the next cycle with respect to $\Delta\theta$ is given by

$$
\begin{pmatrix} p_{\mathrm{IMEP}} \\ p_{\mathrm{max}} \\ dp_{\mathrm{max}} \end{pmatrix} = \begin{pmatrix} p^0_{\mathrm{IMEP}} \\ p^0_{\mathrm{max}} \\ dp^0_{\mathrm{max}} \end{pmatrix} + \begin{pmatrix} \frac{dp_{\mathrm{IMEP}}}{d\Delta\theta} \\ \frac{dp_{\mathrm{max}}}{d\Delta\theta} \\ \frac{d(dp_{\mathrm{max}})}{d\Delta\theta} \end{pmatrix} \Delta\theta. \tag{8.10}
$$

With this model, an optimization problem for finding the wanted $\Delta\theta$ can be formulated

$$\begin{aligned} &\underset{\Delta\theta}{\text{minimize}} && -p_{\text{IMEP}} + \beta(\Delta\theta)^2 \\ &\text{subject to:} && \begin{pmatrix} p_{\text{IMEP}} \\ p_{\max} \\ dp_{\max} \end{pmatrix} = \begin{pmatrix} p^0_{\text{IMEP}} \\ p^0_{\max} \\ dp^0_{\max} \end{pmatrix} + \begin{pmatrix} \frac{dp_{\text{IMEP}}}{d\Delta\theta} \\ \frac{dp_{\max}}{d\Delta\theta} \\ \frac{d(dp_{\max})}{d\Delta\theta} \end{pmatrix} \Delta\theta, \\ & && \begin{pmatrix} p_{\max} \\ dp_{\max} \\ |\Delta\theta| \end{pmatrix} \leq \begin{pmatrix} l_{p_{\max}} \\ l_{dp_{\max}} \\ l_{\Delta\theta} \end{pmatrix}, \end{aligned} \tag{8.11}$$

where β is a positive cost weight for changing the combustion timing and $l_{p_{\max}}$, $l_{dp_{\max}}$ and $l_{\Delta\theta}$ are upper limits on $p_{\max}$, $dp_{\max}$ and the absolute value of $\Delta\theta$. Now by solving Eq. (8.11), an optimal combustion-timing shift can be computed. The solution to Eq. (8.11) without the boundary constraints is given by

$$\Delta\theta^* = \frac{1}{2\beta}\frac{dp_{\text{IMEP}}}{d\Delta\theta}, \tag{8.12}$$

the changes $\Delta\theta_{l_{p_{\max}}}$ and $\Delta\theta_{l_{dp_{\max}}}$ that will reach the constraint boundaries $l_{p_{\max}}$ and $l_{dp_{\max}}$ are computed as

$$\begin{aligned} \Delta\theta_{l_{p_{\max}}} &= \frac{l_{p_{\max}} - p^0_{\max}}{dp_{\max}/d\Delta\theta}, \\ \Delta\theta_{l_{dp_{\max}}} &= \frac{l_{dp_{\max}} - dp^0_{\max}}{d(dp_{\max})/d\Delta\theta}. \end{aligned} \tag{8.13}$$

If one assumes that both $p_{\max}$ and $dp_{\max}$ are monotonically decreasing with $\Delta\theta$ (which was normally the case for the experiments done by the authors when $\theta_{50} > 0$), the solution to Eq. (8.11), $\Delta\theta^*$, is simply the largest value among $\Delta\theta^*$, $\Delta\theta_{l_{p_{\max}}}$ and $\Delta\theta_{l_{dp_{\max}}}$, saturated within the limits of $l_{\Delta\theta}$. The optimization problem can be rephrased as a problem in $\Delta\theta_{\text{SOI}}$ if $\Delta\theta/\Delta\theta_{\text{SOI}}$ is known, in this work it was assumed to be equal to 1. Now all the steps of the controller algorithm have been defined and are summarized in Algorithm 4.

8.3 Results

Open-loop Experiments

In order to investigate the pressure response to combustion timing and evaluate the pressure-prediction method, θ_{SOI} with a single injection was swept for three

Table 8.1 The data used in the prediction- and controller evaluation were obtained from the operating points presented in this table.

Operating Points	1	2	3
Engine Speed [rpm]	1200	1200	1500
Injection Duration [ms]	10	16	10
Injection Pressure [bar]	800	800	800
Inlet Pressure [bar]	1.1	1.35-1.4	1.16
Inlet Temperature [°C]	29-31	40-43	34
λ [-]	2.93	1.72	3.33
EGR Ratio [-]	0	0	0

different speed/load combinations. Each sweep consisted of 2000 cycles where θ_{SOI} was incremented in steps of one from approximately -25 to 5 CAD ATDC. The investigated operation points are presented in Table 8.1.

Thermodynamic Efficiency In Figs. 8.1-8.3, the estimated thermodynamic efficiency η_{th}

$$\eta_{th} = \frac{V_d p_{\text{IMEP}g}}{\max(Q_c)}. \tag{8.14}$$

is plotted against θ_{50} for the three operating points. In the figures, '+' are the sampled data points, the solid red line is the estimated η_{th} sample mean as a function of θ_{50} and the solid black lines are showing the estimated two sample standard deviation distance from η_{th}. These lines were obtained by assuming a Gaussian process regression model using the GPML toolbox, see [Rasmussen and Williams, 2006]. The reason for studying η_{th} instead of p_{IMEP_g} is to compensate for variations in rail pressure and for assumed variations in injected fuel mass due variation in the difference between the injector pressure and in-cylinder pressure with θ_{SOI}. Another reason was that the fuel flow was not measured during the experiments due to limitations of the test rig at the time of the experiment, this is another reason for studying the estimated η_{th}. The heat-transfer model used was given by

$$\begin{aligned} \frac{dQ_{ht}}{d\theta} &= \frac{h_c A}{60 N_{\text{speed}}}(T - T_w), \\ h_c &= \alpha B^{0.2} p^{0.8} T^{-0.55} \omega^{0.8}, \end{aligned} \tag{8.15}$$

and α was tuned to give a flat Q_c before and after the combustion event, with a reasonable magnitude in Q_{ht}, this gave $C_1 = 1, C_2 = 0.06$ and $\alpha = 5$. In Figs 8.1-8.3, it can be seen that as the combustion timing was advanced, the estimated thermodynamic efficiency increased, and then after a certain θ_{50} it started to decrease. This happened more clearly for the lower loads in Figs. 8.1 and 8.3 where

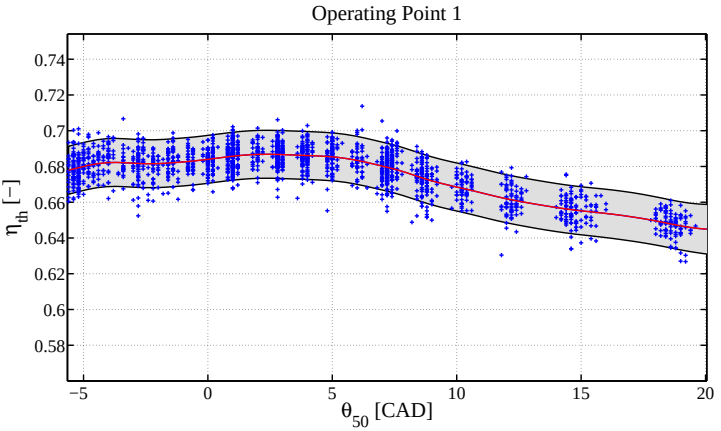

Figure 8.1 Estimated thermodynamic efficiency against combustion timing with 10 ms injection duration at 1200 rpm, '+' are the sampled data points, the solid red line is the estimated η_{th} sample mean as a function of θ_{50} and the solid black lines are showing the estimated two sample standard deviation distance from the mean η_{th}.

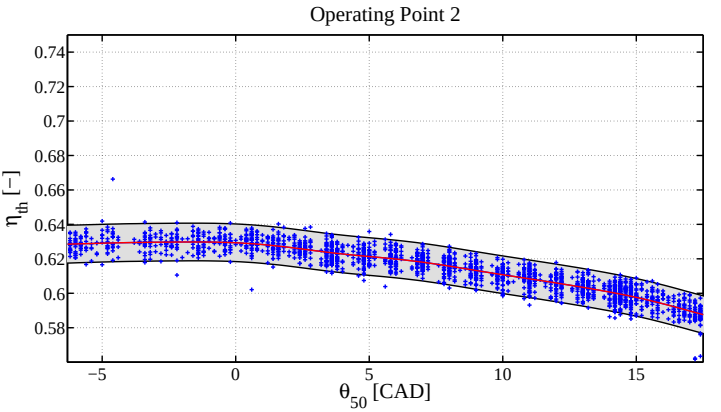

Figure 8.2 Estimated thermodynamic efficiency against combustion timing with 16 ms injection duration at 1200 rpm.

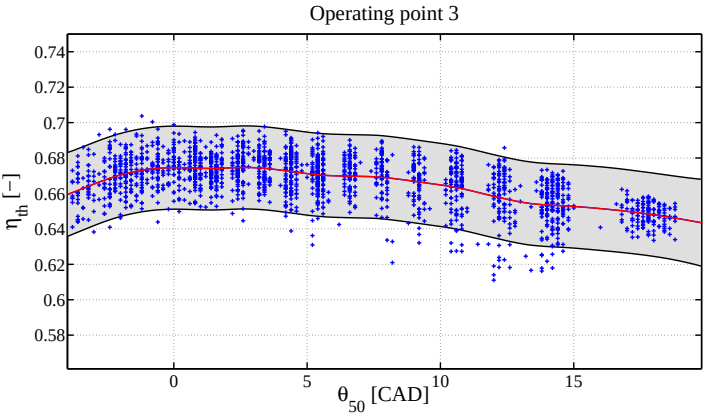

Figure 8.3 Estimated thermodynamic efficiency against combustion timing with 10 ms injection duration at 1500 rpm.

the peak occurred in the intervals $\theta_{50} \in [4,5]$ and $\theta_{50} \in [-1,4]$. In Fig. 8.2, the peak was not as evident but seemed to be before TDC. In Fig. 8.2 and 8.3 it can be seen that η_{th} peaks for slightly negative θ_{50} while it is known that the peak usually occurs for positive θ_{50}. This could be the result of an underestimated heat-transfer rate.

$\Delta\theta_{50}/\Delta\theta_{\mathrm{SOI}}$ In Fig. 8.4, θ_{50} is plotted as a function of θ_{SOI} for the three sweeps. The measured tangent $\Delta\theta_{50}/\Delta\theta_{\mathrm{SOI}}$ seems to be fairly constant for most θ_{SOI}. For the lower load operating points $\Delta\theta_{50}/\Delta\theta_{\mathrm{SOI}}$ was lower at early injection timings and higher at late injection timings.

Pressure Prediction The pressure-prediction performance was tested using the experimental data. In Fig. 8.5. The middle pressure curve in black is the mean cycle pressure p^0 for a specific injection timing, to the left and to the right of this curve, plotted as blue and red solid curves are the mean cycle pressures p^+, p^- for injection timings shifted ± 1 CAD relative to the injection timing of p^0. The blue and red dashed lines are the predicted pressure curves $\hat{p}^+$, $\hat{p}^-$ when the injection timing is shifted ± 1 CAD. In Fig. 8.6, the pressure differences $p^+ - p^0$ and $p^- - p^0$ from Fig. 8.5 are plotted in blue and red together with the corresponding prediction errors $p^+ - \hat{p}^+$(dashed, blue) and $p^- - \hat{p}^-$ (dashed, red). In Figs. 8.7-8.9, the changes of the mean cycle pressure due to injection timing changes $p^\pm - p^0$ are displayed together with the prediction errors $p^\pm - \hat{p}^\pm$ (as in Figure 8.6) for all injection timings in experiments 1, 2 and 3, blue (red) representing a delayed (advanced) injection timing pressure change $p^+ - p^0$ ($p^- - p^0$).

The prediction error is smaller when the injection timing is close to TDC for all operating points and is gradually increased when the combustion timing is

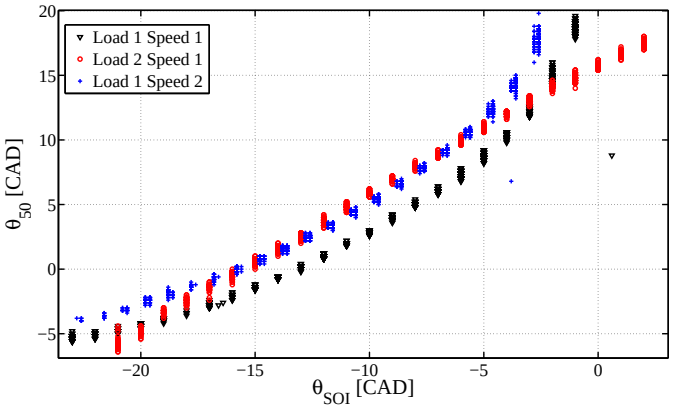

Figure 8.4 θ_{50} against θ_{SOI} for the θ_{SOI} sweeps in Figs. 8.1-8.3

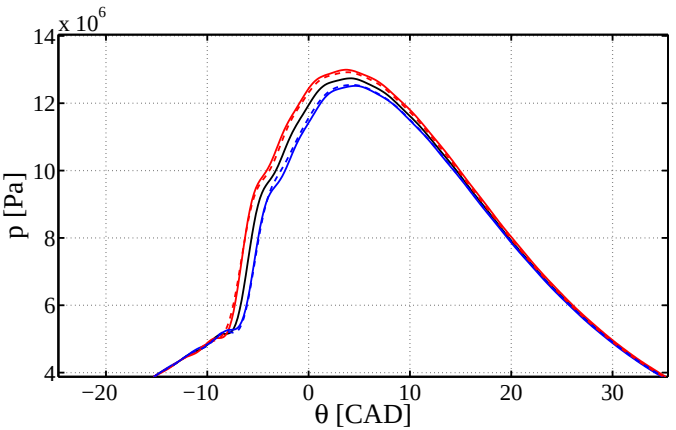

Figure 8.5 Mean cycle pressure p^0 (middle, black) for a specific injection timing from operating point 3. Mean cycle pressures p^+, p^- (solid blue, red) from adjacent injection timings and the predicted pressures $\hat{p}^+$, $\hat{p}^-$ (dashed blue, red) for the same injection timings.

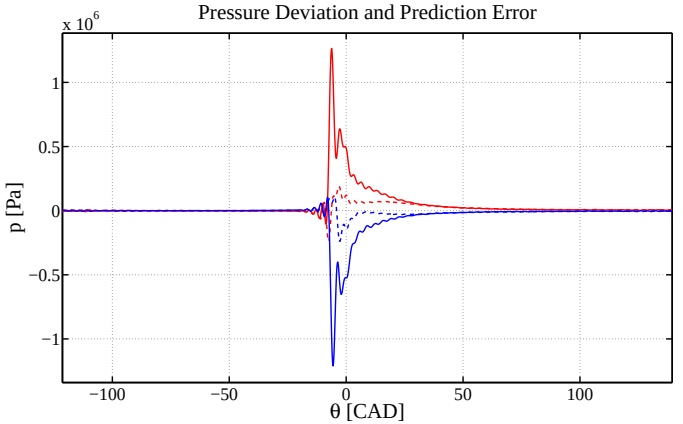

Figure 8.6 The pressure differences $p^+ - p^0$ (blue solid) and $p^- - p^0$ (red solid) together with the prediction errors $p^+ - \hat{p}^+$ (blue dashed), $p^- - \hat{p}^-$ (red dashed) for the pressure curves in Figure 8.5.

advanced or delayed. The prediction error also changes sign somewhere around TDC. For the red lines, this means that the prediction goes from being smaller than the true pressure change to being larger than the true pressure when the injection timing is advanced, the opposite goes for the blue lines. The pressure-prediction performance was evaluated using the R^2 statistic, see Chapter 2. In Figure 8.10, the R^2 prediction performance is displayed as a function of θ_{50}, R^2 was computed accordingly

$$R^2 = 1 - \frac{\sum_i (\hat{p}_i^+ - p_i^+)^2 + \sum_i (\hat{p}_i^- - p_i^-)^2}{\sum_i (p_i^0 - p_i^+)^2 + \sum_i (p_i^0 - p_i^-)^2}, \tag{8.16}$$

where p_i is the measured mean cycle pressure at the given θ_{50}, p_i^+ and p_i^- are the measured pressure mean when θ_{SOI} is shifted one crank angle forward and backward respectively. $\hat{p}_i^+$ and $\hat{p}_i^-$ are the predicted pressure changes, index i denotes the sample i of the pressure curve. The pressure-prediction method seemed to work fairly well in the interval $\theta_{50} \in [0,6]$ where $R^2 \geq 0.9$, but, R^2 started to decrease outside this interval and more steeply for the low-load operating points. The performance was in general better for the high-load operating point.

Closed-loop Experiments

This section demonstrates the previously presented controller-design concept, tuning for best performance was not carried out.

Convergence and β - Sensitivity The controller was run at each of the above investigated operating points, in order to test controller convergence, β was varied

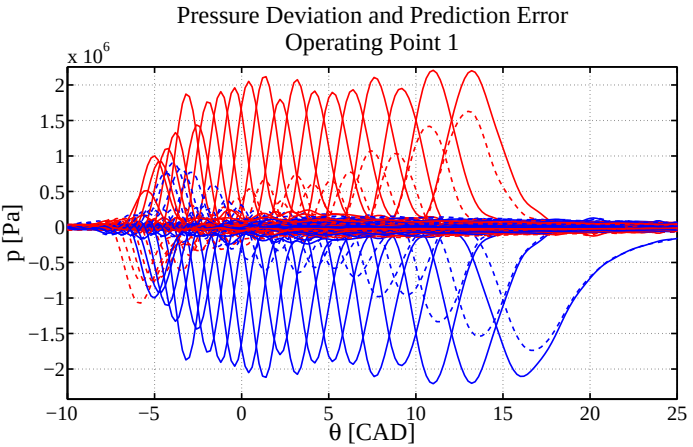

Figure 8.7 Operating point 1. The blue (red) pressures correspond to the measured mean cycle pressure change $p^+ - p^0$ ($p^- - p^0$) due to a positive (negative) injection timing change of magnitude 1, while the dashed blue (red) lines correspond to the mean pressure prediction error for the same injection timing change.

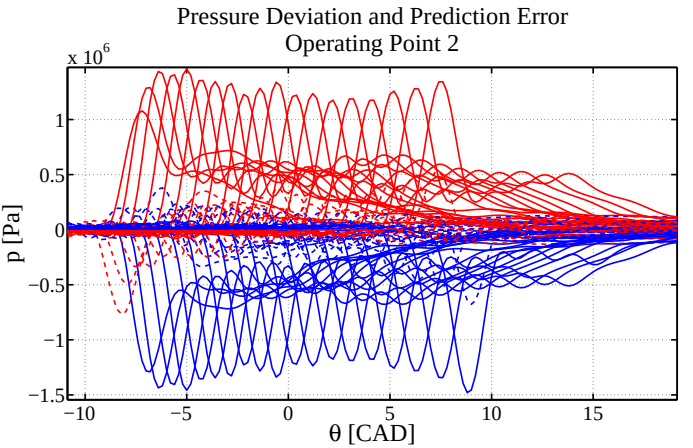

Figure 8.8 Same description as for Figure 8.7 but for operating point 2.

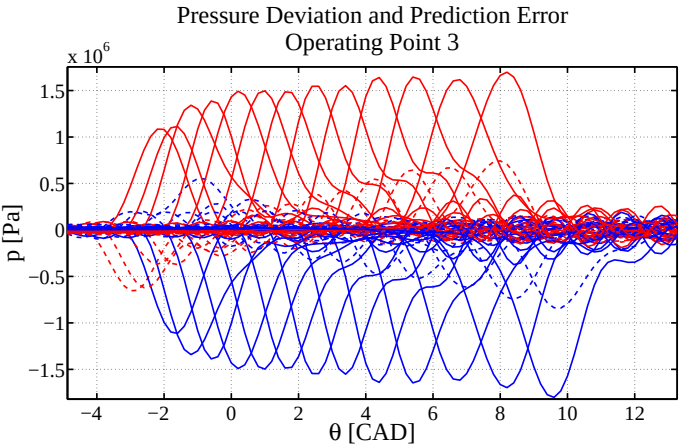

Figure 8.9 Same description as for Figure 8.7 but for operating point 3.

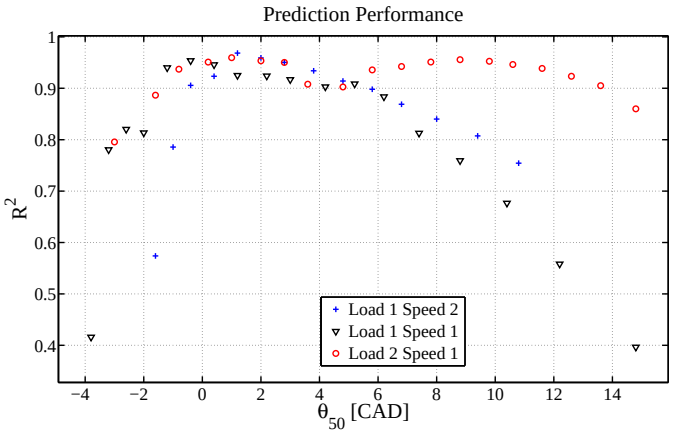

Figure 8.10 R^2 against θ_{50} for the three sweeps in Figs. 8.7-8.9. The pressure-prediction method seemed to work fairly well in the interval $\theta_{50} \in [0,6]$ where $R^2 \geq 0.9$, but, R^2 started to decrease outside this interval and more steeply for the low-load operating points.

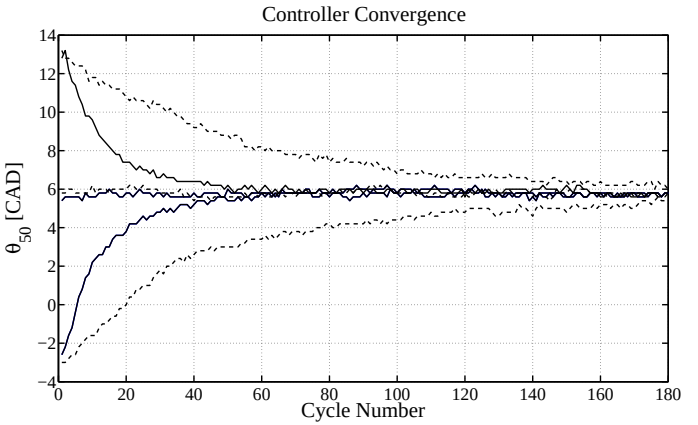

Figure 8.11 Controller convergence at operating point 1 where the solid lines correspond to $\beta = 0.05$ and the dashed lines to $\beta = 0.2$, here the point of convergence is $\theta^*_{50} = 5.8$, $\theta^*_{\mathrm{SOI}} = -7$.

together with different initial injection timings θ^0_{SOI}. The result can be viewed in Figs. 8.11-8.13, here $\theta^0_{\mathrm{SOI}} = \{20, 10, 0\}$ [BTDC] and $\beta = \{0.05, 0.2\}$. In Figs. 8.11-8.13, the controller consistently converges to the same θ_{50} independently of the starting point and the controller parameter β clearly influences the convergence rate of the controller where a larger β gives a slower convergence. In Fig. 8.12 the stationary behavior of the controller becomes oscillatory for $\beta = 0.05$. In the same figure it also seems as the controller converges fast for $\beta = 0.2$ and $\theta^0_{50} = -2$, this was caused by an unintended active $p_{\max}$ constraint, this did not affect the stationary behavior since the estimated $dp_{\mathrm{IMEP}}/d\Delta\theta$ was zero in the convergence point.

Model Parameter Sensitivity The point of convergence θ^*_{50} depends on the parameter values in Eq. (8.2) and especially the parameters of the heat-transfer model. In order to investigate the convergence-point sensitivity, model parameter α (see Eq. 8.3) and TDC offset were varied. The result can be viewed in Figs. 8.14 and 8.15 where α was varied stepwise from 1 to 6 and TDC offset was varied stepwise from 2 to -2 crank angle degrees. In Fig. 8.14, it is shown the magnitude of the heat-transfer rate clearly affected the convergence point of the controller, with increased heat-transfer rate, the controller chose a later convergence point and the converse was true for a decreased heat-transfer rate. A twice increased heat-transfer rate retarded the injection timing as much as 3 CAD. In Fig. 8.15, it can be seen that an offset in TDC of 2 degrees approximately gives a 2 degree offset in the point of convergence in any direction.

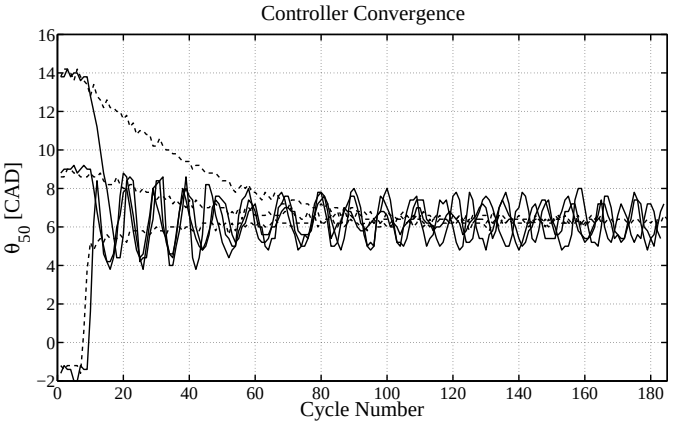

Figure 8.12 Controller convergence at operating point 2 where the solid lines correspond to $\beta = 0.05$ and the dashed lines to $\beta = 0.2$. Here the point of convergence is $\theta^*_{50} = 6.4, \theta^*_{\mathrm{SOI}} = -9.5$. (In the lower dashed θ_{50} trajectory, the fast convergence was due to an unintended active max pressure constraint, this however did not affect the point of convergence since the estimated $dp_{\mathrm{IMEP}}/d\Delta\theta$ was zero in the convergence point).

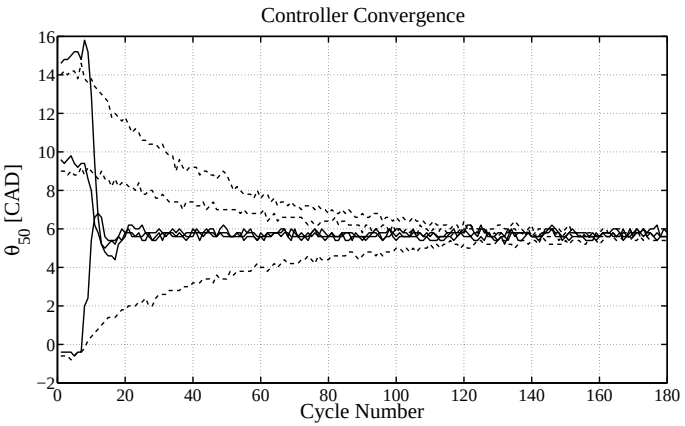

Figure 8.13 Controller convergence at operating point 3 where the solid lines correspond to $\beta = 0.05$ and the dashed lines to $\beta = 0.2$. Here the point of convergence is $\theta^*_{50} = 5.6$, $\theta^*_{\mathrm{SOI}} = -9.6$.

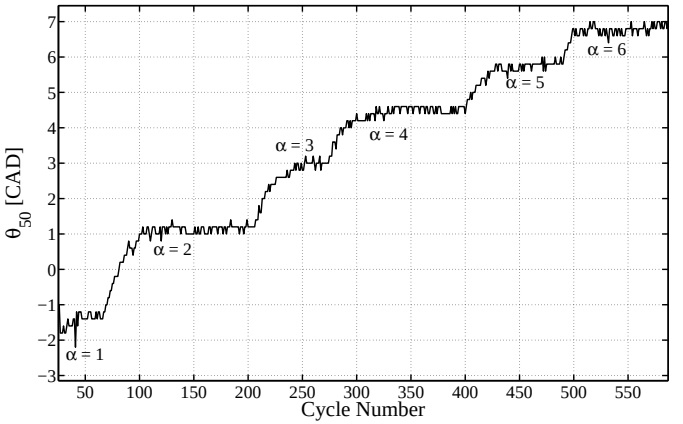

Figure 8.14 Heat-transfer sensitivity. Here the scaling factor α was varied stepwise from 1 to 6, which changes the point of convergence. This experiment was done at operating point 1.

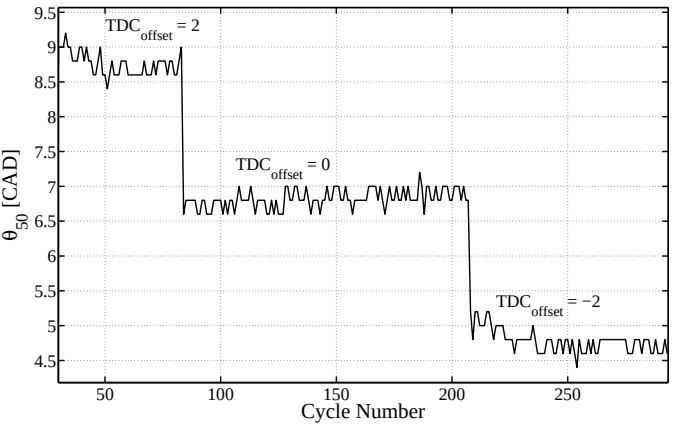

Figure 8.15 TDC-offset sensitivity. Here TDC offset is changed stepwise from 2 to -2 CAD. This experiment was done at operating point 1.

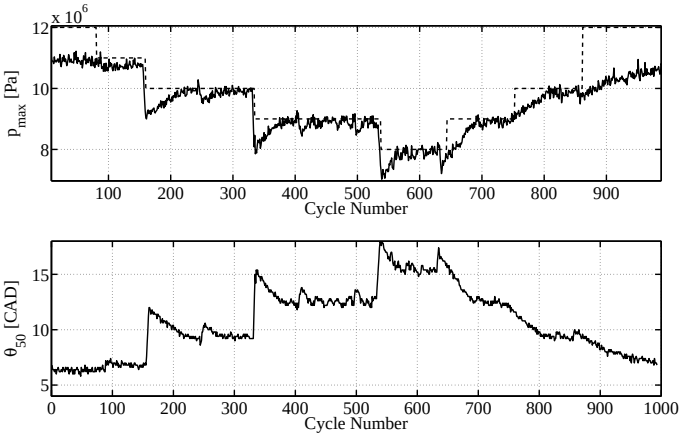

Figure 8.16 In the upper part of the figure, max pressure (solid) is displayed together with the max pressure constraint (dashed), the corresponding θ_{50} is displayed in the lower figure.

Pressure Constraint Tests

The controller performance subject to constraint variation was also investigated, the result can be viewed in Figs 8.16 and 8.17 where the upper bound on $p_{\max}$ was varied from 120 to 80 bar and back and the upper bound on $dp_{\max}$ was varied from 40 to 20 bar per crank-angle degree. The controller managed to fulfill the constraint by initially taking a larger positive step in θ_{SOI} and then slowly advancing θ_{50}, reaching the constraint level from below.

8.4 Discussion

Pressure Prediction Performance

The pressure-prediction method seemed to work fairly well in the interval $\theta_{50} \in [0,6]$ where $R^2 \geq 0.9$, however R^2 started to decrease outside this interval, one explanation for the decrease is the relation between Δ_{SOI} and θ_{50}. In the model it was assumed that $\Delta\theta/\Delta\theta_{\mathrm{SOI}} = 1$, but when the injection timing was early (≈ -25), the ignition delay started to increase which gave $\Delta\theta/\Delta\theta_{\mathrm{SOI}} < 1$. For late injection timings (≈ -5), the ignition delay also started to increase which gives $\Delta\theta/\Delta\theta_{\mathrm{SOI}} > 1$. This explains why the R^2 curve is more flat for the high load experiment in Fig. 8.10 where the ignition delay was not changing significantly and $\Delta\theta/\Delta\theta_{\mathrm{SOI}}$ was almost constant (see Fig. 8.4).

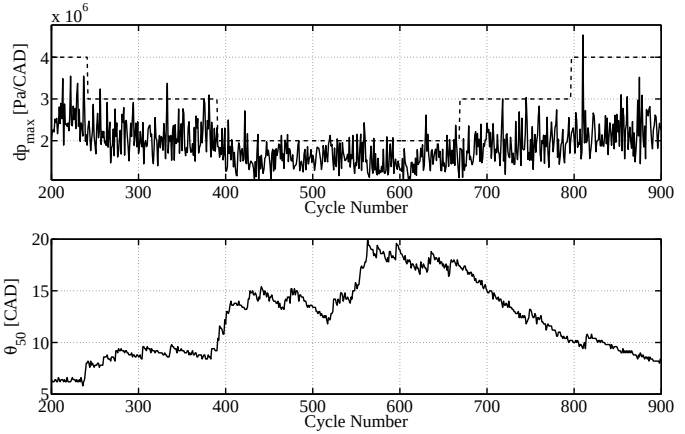

Figure 8.17 In the upper part of the figure, max pressure derivative (solid) is displayed together with the max pressure derivative constraint (dashed), the corresponding θ_{50} is displayed in the lower figure.

Closed-loop Operation

Convergence It was clear from Figs 8.11-8.13 that one can view $1/\beta$ as the controller gain and it was found by studying Fig. 8.12 that the choice of β is a trade-off between convergence speed and stationary cycle-to-cycle variation. If β is chosen too small, the p_{IMEP} term becomes much bigger than $\beta(\Delta\theta)^2$ in the cost function of Eq. (8.11), this then makes small derivatives $dp_{\mathrm{IMEP}}/d\Delta\theta$ to cause large controller steps $\Delta\theta_{\mathrm{SOI}}$ which then lead to the unwanted controller behavior. For best performance, β should be increased with load as $dp_{\mathrm{IMEP}}/d\Delta\theta$ will increase.

The points of convergence in Figs. 8.11-8.13 did not in all cases coincide with the experimentally found most efficient point which was the main goal of the controller, one could view α as a controller trade-off parameter that weighs the effects on efficiency from increased in-cylinder pressure against the increased heat-transfer rate caused by the increased in-cylinder temperature when the combustion timing is advanced, the point where these effects cancel out, gives be the convergence point of the controller.

Pressure Constraints The controller could also be used to fulfill constraints on $p_{\max}$ and $dp_{\max}$ which can be seen in Figs. 8.16 and 8.17. However, with active constraints the controller was found to be a bit more sensitive to the cycle-to-cycle variation of $p_{\max}$ and $dp_{\max}$. If this cycle-to-cycle variation caused any constraint to be violated when close to the constraint level, the controller delayed the injection timing in order to fulfill the constraint, this increased cycle-to-cycle variation. It could therefore be wise to increase β to decrease cycle-to-cycle variation if active constraints are expected. The controller also had a spe-

cific behavior when the constraint was violated as seen in Fig. 8.16 at cycle 340, the controller delays θ_{SOI} greatly and then slowly tries to find a more efficient combustion timing until it reaches the allowed $p_{\max}$ limit, this is happening because when the constraint is changed and the controller is forced to delay the injection timing, $dp_{\max}/d\Delta\theta$ is somewhat underestimated due to the increased ignition delay which explains why the controller takes a too large step in order to fulfill the constraint.

8.5 Conclusions

The controller was consistent in finding a convergence point independently of the initial condition and the controller parameter β, choosing β was found to be a trade-off between convergence speed and steady state cycle-to-cycle variation. The controller was also able to fulfill constraints on $p_{\max}$ and $dp_{\max}$, with active constraints the cycle-to-cycle variation was found to be increased.

The convergence point was sensitive to the modeled heat-transfer rate magnitude and did not coincide with the experimentally found most efficient point, this fact suggests that a fine-tuned heat-transfer model would allow the controller to converge closer to the true most efficient combustion-timing point, this would demand an extensive amount of model-calibration work. Another possibility would be to extend this controller with a data-based gradient method that uses measured p_{IMEP} to estimate $dp_{\mathrm{IMEP}}/d\Delta\theta$. It was also found that the pressure prediction performance was relying on the assumption of $\Delta\theta/\Delta\theta_{\mathrm{SOI}}$ which depend on θ_{SOI}. In this work it was set constant equal to 1. An adaptive method for estimation of this quantity, alternatively an ignition-delay model would thus probably improve the pressure-prediction performance.

9

Combustion Control Using Multiple Fuel Injections

9.1 Introduction

It was discovered in [Manente et al., 2009] that the long ignition delays in single-injection PPC give rise to very high pressure-rise rate due to violent HCCI-like combustion rates. High pressure-rise rates is an indicator for high audible-noise levels and could also cause mechanical engine damage, therefore, the pressure-rise rate has to be kept below certain levels in order to ensure silent and safe operation. Previous research by [Tsurushima, 2009] implies that pressure oscillations commonly resulting from violent combustion rates are able to break insulating thermal-boundary layers which increases heat-transfer flux to the cylinder walls. A remedy to the problem of high pressure-rise rates in PPC is to introduce a pilot-fuel injection, e.g. by having an early pilot injection with less than half of the fuel and a main injection containing the majority of the fuel amount. The pilot injection sets a lean mixture environment that decreases the ignition delay of the main injection and therefore decreases the combustion rates. This technique is also used in conventional diesel engines both to improve low-load performance [MacMillan et al., 2009; Osuka et al., 1994] and to decrease emissions and engine-noise levels [Eriksson and Nielsen, 2014; Kiencke and Nielsen, 2000].

Both optical OH-chemiluminescence experiments [Tanov et al., 2014] and computational fluid dynamics (CFD) simulation research [Solsjö, 2014] have been performed to better understand multiple-injections light-duty PPC, findings suggest that multiple injections can be used to create stratified mixtures with different air-fuel ratios where very lean mixtures created by pilot injections burns more slowly but assist the ignition of the fuel-richer mixtures created by the main injection.

With the increased amount of fuel-injection events, the amount of calibration work for optimized engine performance for different loads and speeds grows exponentially, [Meyer, 2011]. Therefore, it is of course very appealing to find fuel-

injection controllers that automatically find fuel-injection timings and fuel distribution among the multiple injections. Previous work on pilot-injection combustion control in low-temperature combustion concepts has been presented by [Ott et al., 2013; Eichmeier et al., 2012; Ekholm et al., 2008; Kokjohn et al., 2009].

This chapter presents experimental PPC results that reflects engine output characteristics w.r.t. double-injection parameters. The experimental results are then used for design of a model predictive controller that is able to track combustion phasing while guaranteeing an upper bound on the mean maximum pressure-rise rate. Controller implementation and experimental performance during engine load and speed variations are also presented.

Maximum Pressure-Rise Rate $dp_{\max}$

The maximum pressure rise rate $dp_{\max}$ is in this work defined as

$$dp_{\max} = \max_{\theta} \frac{dp}{d\theta}. \tag{9.1}$$

Due to the high cycle-to-cycle variation of $dp_{\max}$ it has to be filtered in order to be used as a feedback variable. The measured $dp^m_{\max}$ was therefore modelled as $dp_{\max}$, corrupted with additive Gaussian noise with standard deviation σ

$$dp^m_{\max} = dp_{\max} + e,\ e \sim N(0, \sigma^2). \tag{9.2}$$

A Kalman filter was then used to recover $dp_{\max}$ from $dp^m_{\max}$, a more detailed presentation of this procedure is given in Section 9.3.

Fuel-Injection Variables

The start of the main and pilot injection θ^m_{SOI}, θ^p_{SOI} are here defined as the crank-angle of the injector-current rising flanks. The fuel-injection durations θ^m_{DOI}, θ^p_{DOI} are defined as the difference in milliseconds between the injector-current pulse width and a threshold value τ_{th} that is the minimum current-pulse duration for which fuel flows into the cylinder, here it was assumed that $\tau_{th} = 0.25$ ms, see Fig. 9.1. Instead of studying θ^m_{SOI}, θ^p_{SOI}, θ^m_{DOI} and θ^p_{DOI} explicitly, the pilot ratio r_p

$$r_p = \frac{\theta^p_{\text{DOI}}}{\theta^p_{\text{DOI}} + \theta^m_{\text{DOI}}}, \tag{9.3}$$

the injection separation d_{SOI}

$$d_{\text{SOI}} = \theta^m_{\text{SOI}} - \theta^p_{\text{SOI}}, \tag{9.4}$$

the main injection timing θ^m_{SOI} and the total injection duration $\theta^{\text{tot}}_{\text{DOI}}$ were studied

$$\theta^{\text{tot}}_{\text{SOI}} = \theta^m_{\text{DOI}} + \theta^p_{\text{DOI}}. \tag{9.5}$$

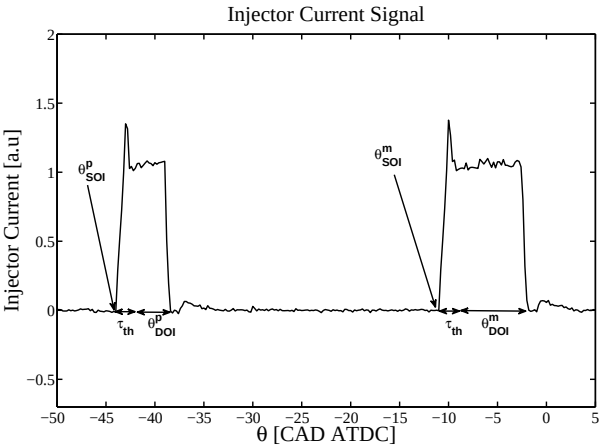

Figure 9.1 Injector-current signal with a pilot and a main injection together with the definitions of θ^x_{SOI}, θ^x_{DOI}, and τ_{th}.

This variable change was done because at a given operating point, $\theta^{\mathrm{tot}}_{\mathrm{SOI}}$ and θ^m_{SOI} would be determined by the desired load and combustion phasing, r_p and d_{SOI} are then free parameters whose influence on engine output parameters are studied in the following sections.

9.2 Experimental Characterization

In order to investigate the engine-output properties w.r.t. different double-injection configurations, r_p and d_{SOI} were varied while keeping θ_{50} and the indicated gross mean effective pressure p_{IMEPg} constant using θ^m_{SOI} and $\theta^{\mathrm{tot}}_{\mathrm{DOI}}$ at the operating points (OP) presented in Table 9.1. At each operating point $dp_{\max}$, the indicated thermal efficiency, η_{th}, NO_x, HC and soot emission levels were measured in steady state during 1000 cycles. The gains from θ^m_{SOI} and θ^p_{SOI} to θ_{50} were also investigated. The results of these experiments and its implications for controller design are presented and discussed in the following sections.

Maximum Pressure Rise Rate $dp_{\max}$

In Figs. 9.2 and 9.3 the measured $dp_{\max}$ is presented as level curves of a linear interpolations between the operation points in Table 9.1. It is clear that r_p can be used to control $dp_{\max}$ since $dp_{\max}$ decreases with r_p. The $dp_{\max}$ controllability is also shown to be higher for small d_{SOI}. A possible explanation for the observed trends is that the air-fuel mixture that is set up by the pilot injection decreases the ignition delay of the main-injection fuel charge, making the combustion of

Table 9.1 The investigated operating points. The notion $x : y : z$ means that the corresponding parameter was swept from x to z in steps of y, every combination of r_p and d_{SOI} were tested.

	OP 1	OP 2
p_{IMEPg} [bar]	5	10
N_{speed} [rpm]	1200	1200
λ [-]	2.5	1.8
r_{EGR} [rpm]	15	25
θ_{50} [CAD]	6	10
r_p [-]	$0 : 0.125 : 0.5$	$0 : 0.075 : 0.3$
d_{SOI} [CAD]	$0 : 12.5 : 50$	$0 : 12.5 : 50$

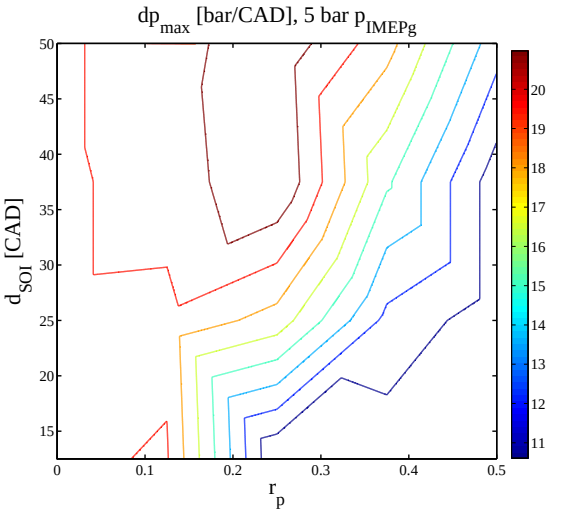

Figure 9.2 Maximum pressure-rise rate contour plot versus d_{SOI} and r_p at 5 bar p_{IMEPg}. It is clear that r_p can be used to control dp_{max} since dp_{max} decreases with r_p. The dp_{max} controllability is also shown to be higher for small d_{SOI}.

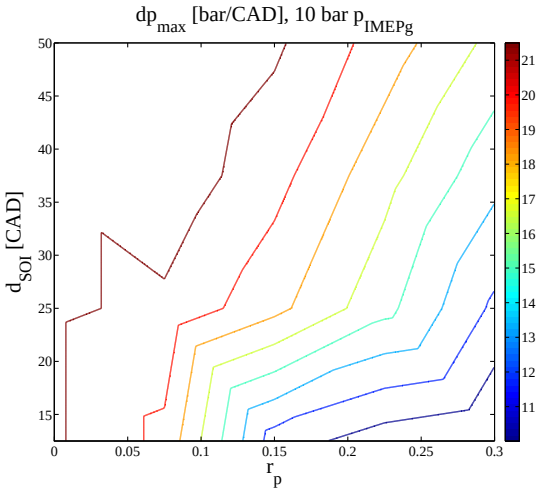

Figure 9.3 Maximum pressure-rise rate contour plot versus d_{SOI} and r_p at 10 bar p_{IMEPg}.

this charge less violent. This effect then becomes stronger for larger pilot-fuel amounts and weakens as the pilot charge is more dilute at θ^m_{SOI} as d_{SOI} increases. The ignition delay of the main injection, τ^m, is presented in Figs. 9.4 and 9.5, τ^m was computed accordingly

$$\tau_m = \theta_{10} - \theta^m_{\mathrm{SOI}} \text{ [ms]}. \tag{9.6}$$

It can be seen that τ^m and $dp_{\max}$ correlate in OP 1 and 2, however, the correlation is not as strong in OP 1 for large d_{SOI} where τ^m stays low with increasing $dp_{\max}$. A hypothetical explanation is that the increased $dp_{\max}$ is caused by the increased ignition delay of the pilot charge which creates a more violent burning rate.

Thermodynamic Efficiency

The thermodynamic efficiency η_{th} is here defined as the ratio between the indicated gross mean effective pressure p_{IMEPg} and the fuel mean effective pressure p_{FuelMEP}

$$\eta_{th} = \frac{p_{\mathrm{IMEPg}}}{p_{\mathrm{FuelMEP}}}, \tag{9.7}$$

$$p_{\mathrm{FuelMEP}} = \frac{Q_{LHV} m_f}{V_d}, \tag{9.8}$$

where m_f is the injected fuel amount and Q_{LHV} the lower heating value of the fuel. Note that this definition of η_{th} includes the combustion efficiency. The results presented in Figs. 9.6, 9.7 show that η_{th} has a slight maxima when having

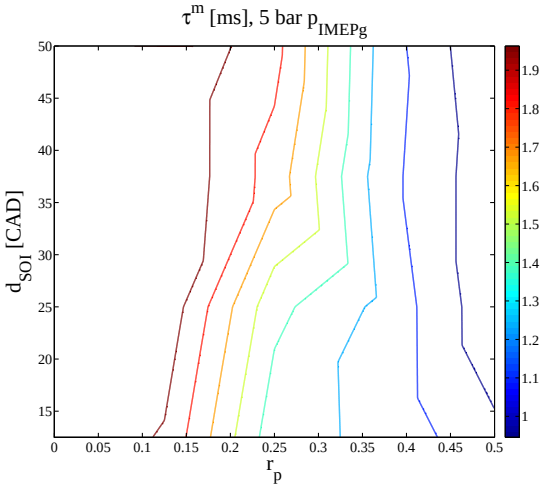

Figure 9.4 Main-injection ignition delay contour plot versus d_{SOI} and r_p at 5 bar p_{IMEPg}. The main-injection ignition delay correlates with $dp_{\max}$ presented in Figs. 9.2 and 9.3.

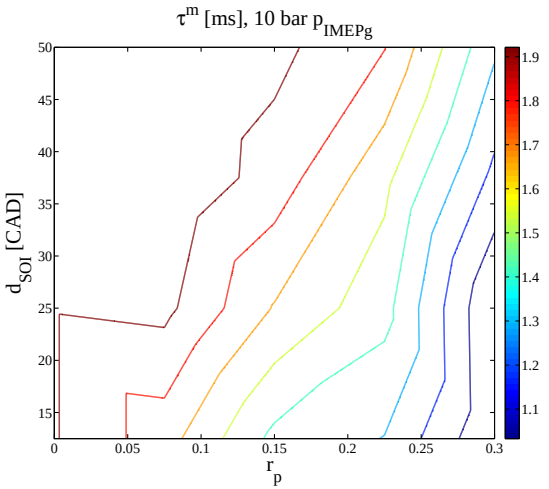

Figure 9.5 Main-injection ignition delay contour plot versus d_{SOI} and r_p at 10 bar p_{IMEPg}.

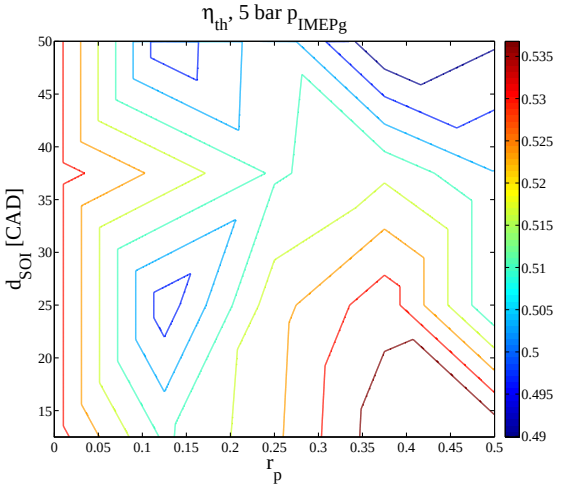

Figure 9.6 Thermodynamic efficiency contour plot versus d_{SOI} and r_p at 5 bar p_{IMEPg}. The results show that η_{th} has a slight increase when having a pilot injection close to the main injection, another visible trend is that η_{th} drops when d_{SOI} increases and that this effect is stronger when r_p is higher.

a pilot injection close to the main injection, this is more significant for OP 1 in Fig. 9.6. Another visible trend is that η_{th} drops when d_{SOI} increases and that this effect is stronger when r_p is higher. This indicates that it could be more efficient to have a pilot injection but that this effect is reversed when the pilot is advanced.

HC

The measured HC emission levels are presented in Figs. 9.8 and 9.9. The HC emission levels increase steeply as d_{SOI} and r_p are simultaneously increased, the explanation for this could be that the pilot fuel is injected into the crevice regions outside of the combustion chamber and does not burn completely, it could also be that the pilot-fuel mixture becomes too lean to burn due to the increased mixing period. The decrease in combustion efficiency indicated by the HC emission-level increase could also explain the efficiency drop seen in Figs. 9.6 and 9.7.

NO_x

The measured NO_x emission levels are presented in Figs. 9.10 and 9.11 where it can be seen that the NO_x level mainly depends on r_p and decreases with an increased r_p. A hypothetical explanation for this is the increase in τ_m with a decreased r_p. This gives more violent combustion with increased temperatures,

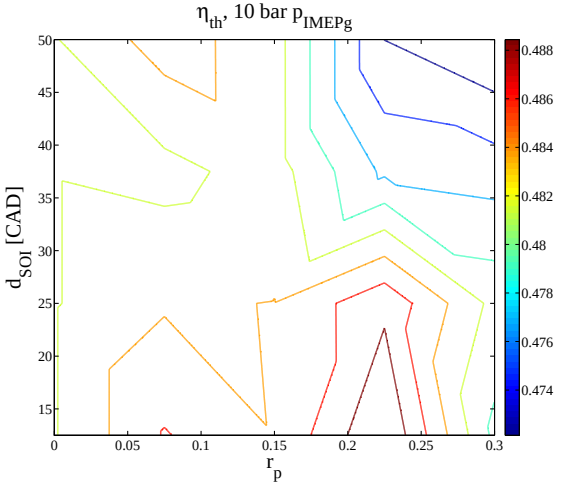

Figure 9.7 Thermodynamic efficiency contour plot versus d_{SOI} and r_p at 10 bar p_{IMEPg}.

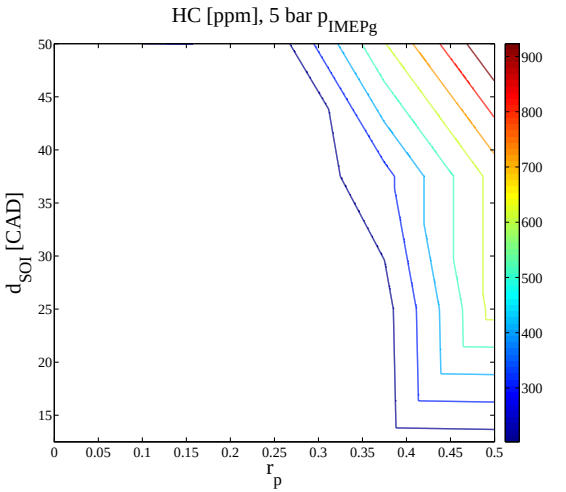

Figure 9.8 HC emission-level contour plot versus d_{SOI} and r_p at 5 bar p_{IMEPg}. The HC emission levels increase steeply as d_{SOI} and r_p are simultaneously increased, the explanation for this could be that the pilot fuel is injected into the crevice regions outside of the combustion chamber and does not burn completely, the decrease in combustion efficiency indicated by the HC emission increase could also explain the efficiency drop seen in Figs. 9.6 and 9.7

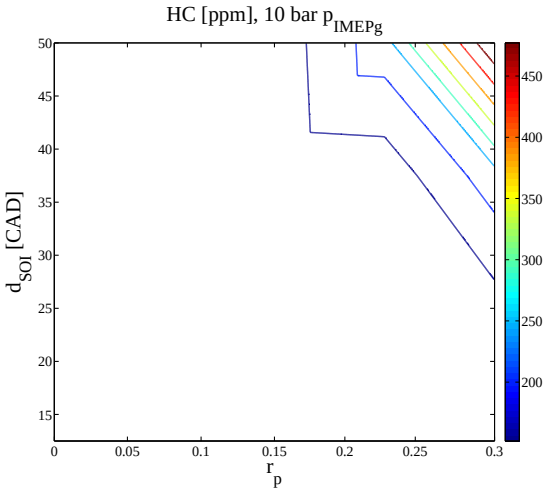

Figure 9.9 HC emission-level contour plot versus d_{SOI} and r_p at 10 bar p_{IMEPg}.

with leaner charge mixtures at the start of combustion it gives increased NO_x formation.

Soot

In Figs. 9.12 and 9.13 it is shown that the soot levels increase with r_p and more so when d_{SOI} is small, the reason for this is probably that the ignition delays for the fuel injections are minimized at these operating points which makes the charge burns more rich and this increases soot formation. Similar NO_x and Soot emission trends were presented by [Manente et al., 2010b, 2009].

Combustion-Phasing Controllability

The controllability of the combustion phasing θ_{50} was investigated by varying θ^m_{SOI} and θ^p_{SOI} for the operating points presented in Table 9.1. For each operating point and r_p and d_{SOI} combination, $\theta^{m,p}_{\mathrm{SOI}}$ was varied individually as square waves with amplitudes of 1 CAD and periods of 25 cycles during 500 cycles. The gains from $\theta^{m,p}_{\mathrm{SOI}}$ to θ_{50} were estimated from these experiments and are presented in Figs. 9.14, 9.15, 9.16 and 9.17.

It is clear from the results that it is θ^m_{SOI} that controls θ_{50} and that the controllability somewhat decreases with r_p, while the gain from θ^p_{SOI} is insignificant. A hypothetical explanation is that the stratification from the main injection that ignites the charge and that the pilot injection charge affects the combustion timing more when r_p is increased, the same trend was shown by [Hagesawa and Yanigihara, 2003; Manente et al., 2009].

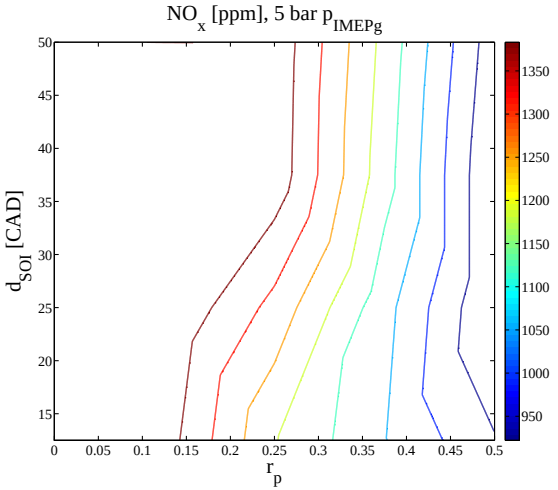

Figure 9.10 NO_x emission-level contour plot versus d_{SOI} and r_p at 5 bar p_{IMEPg}. It can be seen that NO_x mainly depends on r_p and decreases with an increased r_p. A hypothetical explanation for this is the increase in τ_m which gives more violent combustion with increased temperatures, with leaner charge mixtures at the start of combustion this gives increased NO_x formation.

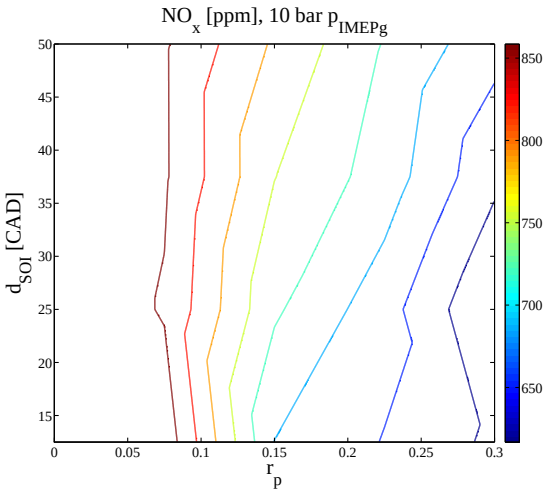

Figure 9.11 NO_x emission-level contour plot versus d_{SOI} and r_p at 10 bar p_{IMEPg}.

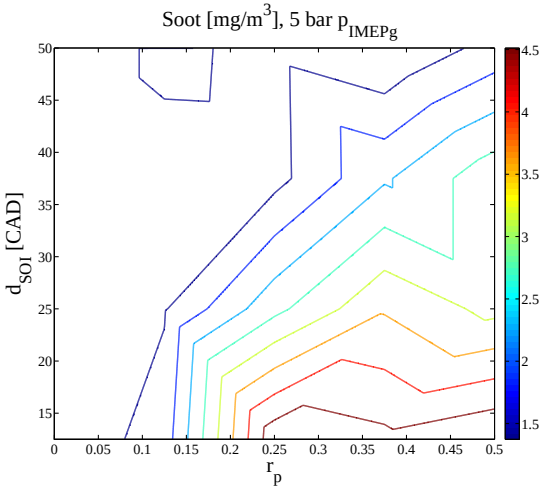

Figure 9.12 Soot emission-level contour plot versus d_{SOI} and r_p at 5 bar p_{IMEPg}. It is shown that the soot levels increase with r_p and more so when d_{SOI} is small, the reason for this is probably that the ignition delays for the fuel injections are minimized at these operating points which makes the charge burns more rich and this increases soot formation.

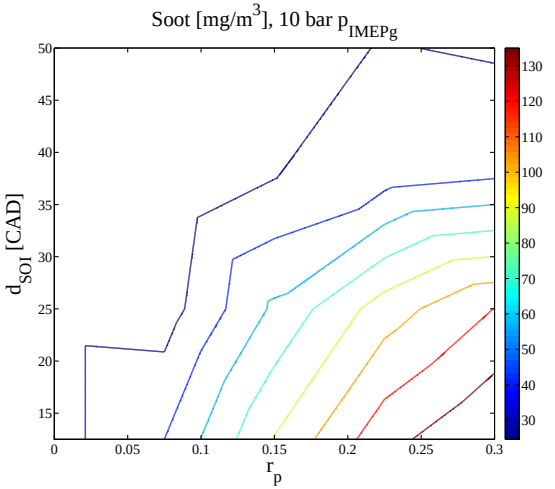

Figure 9.13 Soot emission-level contour plot versus d_{SOI} and r_p at 10 bar p_{IMEPg}.

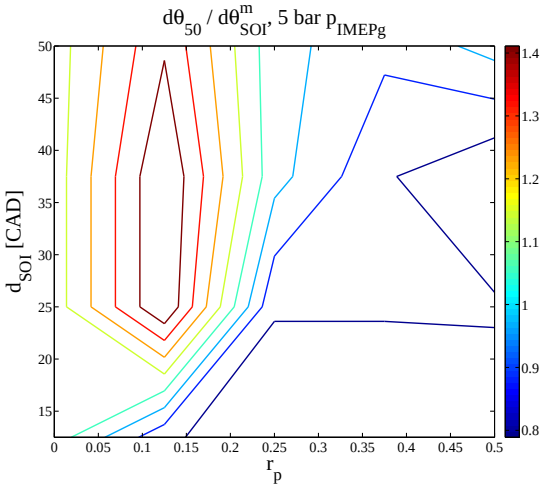

Figure 9.14 The estimated gain from θ^m_{SOI} contour plot versus d_{SOI} and r_p at 5 bar p_{IMEPg}. The gain from θ^m_{SOI} is high for all injection configuration but is significantly decreased as the pilot ratio is increased.

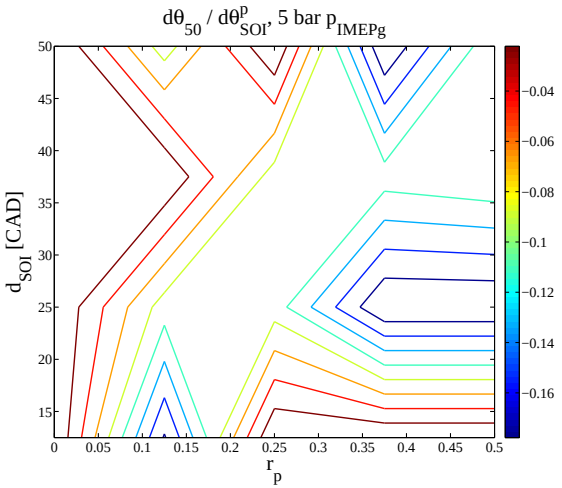

Figure 9.15 The estimated gain from θ^p_{SOI} contour plot versus d_{SOI} and r_p at 5 bar p_{IMEPg}. The gain from θ^m_{SOI} is essentially zero for all injection configurations, when comparing this result to Fig. 9.14, it is clear that it is θ^m_{SOI} that controls θ_{50}.

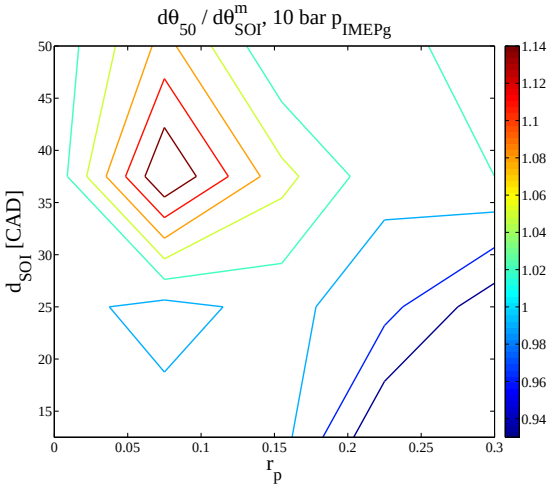

Figure 9.16 The estimated gain from θ^{m}_{SOI} contour plot versus d_{SOI} and r_p at 10 bar IMEPg.

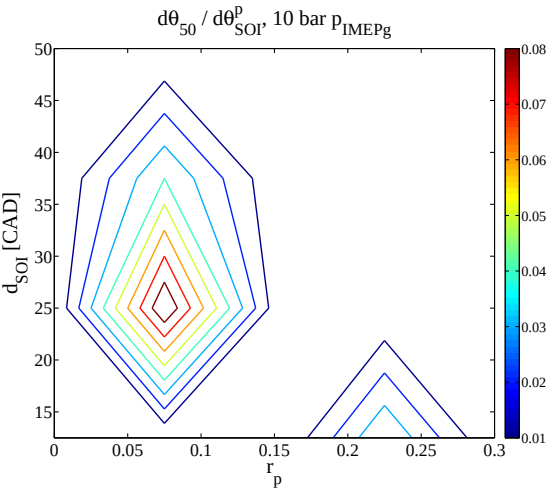

Figure 9.17 The estimated gain from θ^{p}_{SOI} contour plot versus d_{SOI} and r_p at 10 bar p_{IMEPg}.

Summary

The findings in the preceding experimental results are summarized accordingly

- r_p can be used to control $dp_{\max}$, the controllability decreases with d_{SOI}.
- η_{th} increases slightly with r_p, the opposite holds with large d_{SOI}, this is probably linked to the increased HC-emission levels.
- r_p is a trade-off between NO_x and soot emission levels.
- θ_{50} is controlled by θ^m_{SOI}.

9.3 Controller Design

The goal of the controller design is to find a controller that simultaneously keeps θ_{50} at a predefined value while $dp_{\max}$ is maintained below an upper bound. The experimental results above show that $dp_{\max}$ can be controlled with r_p while θ_{50} is controlled with θ^m_{SOI}. To maintain high controllability of $dp_{\max}$, d_{SOI} should be kept low, in this work d_{SOI} was therefore chosen constant, $d_{\mathrm{SOI}} = 20$. In order to maximize the ignition delay τ^m which is a key parameter in PPC it was also decided to try to keep r_p low while fulfilling the constraint on $dp_{\max}$. The engine load was then controlled with $\theta^{\mathrm{tot}}_{\mathrm{DOI}}$, in a separate closed loop. In order to build a state-space model and apply model-based controller design, the state vector x and input vector u are introduced accordingly

$$\begin{aligned} x(k) &= \left(\theta_{50}(k),\ dp_{\max}(k),\ r_p(k)\right)^T, \\ u(k) &= \left(\Delta\theta^m_{\mathrm{SOI}}(k),\ \Delta r_p(k)\right)^T, \end{aligned} \tag{9.9}$$

where k denotes the cycle index and Δ is the forward-difference operator, r_p is here introduced as a state in order to keep track of its absolute value. A simple linear cycle-to-cycle state-space model could then be formulated accordingly

$$\begin{aligned} x(k+1) &= Ax(k) + Bu(k) + v(k), \\ y(k) &= Cx(k) + e(k), \end{aligned} \tag{9.10}$$

the assumption of a static relation between u and x gives $A = I_{3x3}$, B contains the gains from $u(k)$ to $x(k)$

$$B = \begin{pmatrix} B_{11} & B_{12} \\ B_{21} & B_{22} \\ 0 & 1 \end{pmatrix}. \tag{9.11}$$

From the experimental results in Figs. 9.14, 9.15, 9.16 and 9.17 it was found that $B_{11} = 1$. The gain $B_{12} = -3$ was found by studying Figs. 9.4 and 9.5. When advancing θ_{50}, τ^m increases and θ_{50} is moved closed to TDC which gives more violent

combustion and an increased $dp_{\max}$, it was found that B_{21} was quite dependent on the operating point as well as θ_{50}, however, a constant value of -0.5 was chosen. The $dp_{\max}$ experiments presented in Figs. 9.2 and 9.3 gave $B_{22} = -25$. The observation matrix C is given by I_{3x3} since the first two states could be estimated directly using the pressure-sensor information. In order to incorporate model uncertainty and measurement noise, zero-mean white-noise processes ω_k and e_k were introduced with variance matrices Q_v and Q_e

$$\begin{aligned} Q_v &= E(v(k)v(k)^T), \\ Q_e &= E(e(k)e(k)^T). \end{aligned} \tag{9.12}$$

Model Predictive Control

Since the system (9.10) to be controlled has multiple inputs and outputs with interaction effects and constraints, the model predictive control (MPC) framework was chosen as a solution to the controller-design problem. For the control problem studied in this article the MPC optimization problem was formulated as

$$\begin{aligned} \underset{u}{\text{minimize}} \quad & J = \sum_{k=1}^{H_p} \omega_1 ||\theta_{50}(k) - r_{\theta_{50}}(k)||_2^2 + \omega_2 ||\theta_{\text{SOI}}^m(k)||_2^2 + \omega_3 ||r_p(k)||_2^2 \\ & \qquad + \sum_{k=1}^{H_c} \omega_4 ||\Delta\theta_{\text{SOI}}(k)||_2^2 + \omega_5 ||\Delta r_p(k)||_2^2 + \gamma\epsilon^2, \\ \text{subject to} \quad & x(k+1) = Ax(k) + Bu(k), \text{ for } k = 1,\ldots,H_c, \\ & x(k+1) = Ax(k), \text{ for } k = H_c+1,\ldots,H_p-1, \\ & x(k-1) = x_0, \\ & 0 \le r_p(k) \le r_p^b, \\ & dp_{\max}(k) \le dp_{\max}^b + \epsilon, \\ & \epsilon \ge 0, \end{aligned} \tag{9.13}$$

where $r_{\theta_{50}}(k)$ is the θ_{50} set point, r_p^b and $dp_{\max}^b$ are upper bounds for r_p and $dp_{\max}$ which was set to 0.3 and 8 bar/CAD. The variable ϵ is a cost-variable that penalizes violation of the state inequality constraint, it was introduced in order to ensure feasible solutions. The positive weights ω_i and γ sets the priority of the controller and were manually tuned in order to obtain adequate closed-loop response times subject to overshoot and actuator cycle-to-cycle variation, the weights used in the results section are presented in Table 9.2. The horizons were chosen according to $H_p = 16$ and $H_c = 8$. Average computational times for solving (9.13) were on average 1-5 ms for one cylinder. The computations were done every two engine revolutions after the pressure traces of the latest cycle for each cylinder was sampled.

Table 9.2 The chosen MPC weights.

ω_1	ω_2	ω_3	ω_4	ω_4	γ
100	0.01	25	6000	8000	1

Kalman Filter

This section only considers the first two state equations of Eq. (9.10), the system-matrices presented here are therefore truncated accordingly in the following equations.

In order to estimate x from y, u and the model (9.10), a stationary Kalman filter was used. The Kalman filter state estimate $\hat{x}$ was updated recursively according to

$$\hat{x}(k+1) = A\hat{x}(k) + Bu(k) + K(y(k) - C\hat{x}(k)) \tag{9.14}$$

where the Kalman K gain is given by the steady-state solution of Algorithm 1 in Chapter 3 and P is the positive-definite solution to the Riccati equation

$$\begin{aligned} K &= APC^T(Q_v + CPC^T)^{-1}, \\ P &= APA^T + Q_v - APC^T(Q_e + CPC^T)^{-1}CPA^T. \end{aligned} \tag{9.15}$$

The covariance matrices used

$$Q_e = \begin{pmatrix} 25 & 0 \\ 0 & 800 \end{pmatrix},\ Q_v = \begin{pmatrix} 10 & 0 \\ 0 & 50 \end{pmatrix}, \tag{9.16}$$

were chosen to get sufficient attenuation of measurement noise.

9.4 Controller Evaluation

With the controller design presented above, the controller performance was tested experimentally during set-point changes in θ_{50} and IMEPg, during changes in the $dp_{\max}$ upper bound and during changes in N_{speed}.

The load, p_{IMEPg}, was changed by varying $\theta_{\text{DOI}}^{\text{tot}}$ while keeping the common-rail pressure constant at 800 bar. During the load changes, p_{IMEPg} and the common-rail pressure level was controlled using manually tuned PI controllers and pre-calibrated feedforward signals. The N_{speed} changes were performed by changing the used engine-brake motor-speed set point.

Input and output data for one cylinder are presented during a sequence of θ_{50} set-point changes in Fig. 9.18. In the upper diagrams $\hat{x}$ is presented in black together with y which is presented in grey. As θ_{50} is advanced, r_p is forced to increase in order to fulfil the specified $dp_{\max}$ constraint of 8 bar/CAD, when θ_{50}

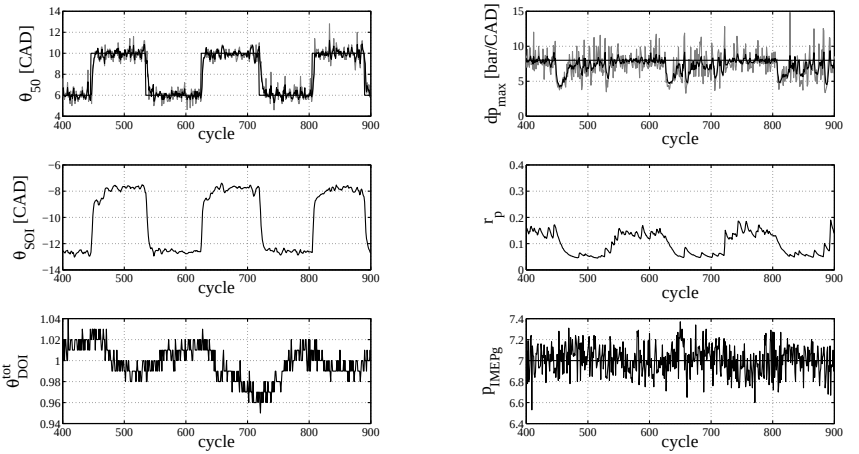

Figure 9.18 Input and output data during a sequence of θ_{50} set-point changes. In the upper diagrams $\hat{x}$ is presented in black together with y which is presented in grey. As θ_{50} is advanced, r_p is forced to increase in order to fulfil the specified $dp_{\max}$ constraint of 8 bar/CAD, when θ_{50} is retarded, r_p is decreased due to its absolute-value cost in order to maximize τ^m.

is delayed, r_p is decreased due to its absolute-value cost in order to maximize τ^m. The response time for θ_{50} is in the range of 3 cycles while the response time of the decrease in r_p is around 20 cycles. In Fig. 9.19, input and output data are presented during step changes in the $dp_{\max}$ upper bound. The response time of $dp_{\max}$ during a negative upper-bound step change is around 2 cycles while the response time of $dp_{\max}$ during an positive upper-bound step change is around 10 cycles, θ^m_{SOI} have to adjust for variations in θ_{50} caused by the changes in r_p. System response during p_{IMEPg} set-point changes are presented in Fig. 9.20, the response time for p_{IMEPg} is around 20 cycles, and as $\theta^{\text{tot}}_{\text{DOI}}$ varies, θ^m_{SOI} is adjusted in order keep θ_{50} constant, r_p is only doing minor adjustments in order to keep $dp_{\max}$ below the upper limit, the variation in r_p indicates that $dp_{\max}$ is not so sensitive to changes in $\theta^{\text{tot}}_{\text{DOI}}$ at this operating point. Input signal oscillations can be observed around cycles 200 and 500. In Fig 9.21, system response to N_{speed} transients are presented, here r_p has to increase and θ^m_{SOI} advance in order to fulfil the constraint and set-point level when N_{speed} increases. It can also be seen that the $dp_{\max}$ noise level decreases with speed.

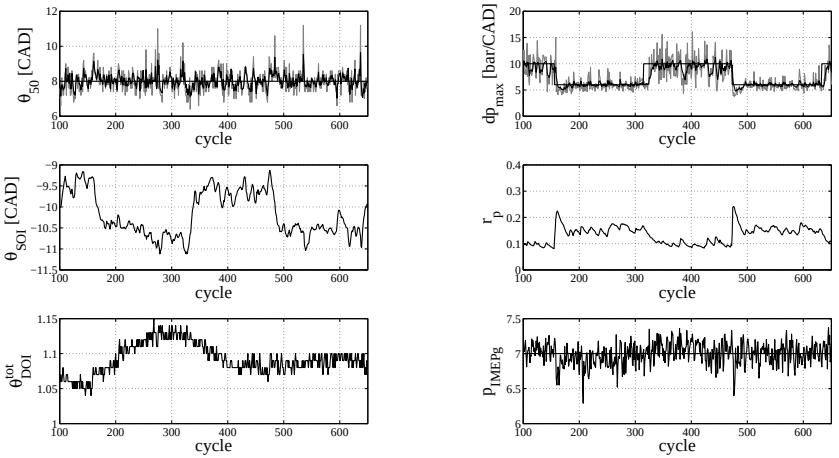

Figure 9.19 Input and output data during step changes in the $dp_{\max}$ upper bound. The response time of $dp_{\max}$ during a negative upper-bound step change is around 2 cycles while the response time of $dp_{\max}$ during an positive upper-bound step change is around 10 cycles, θ^m_{SOI} have to adjust for variations in θ_{50} caused by the changes in r_p.

9.5 Discussion and Conclusions

The results indicate that the designed controller was successful in maintaining an upper bound for $dp_{\max}$ using r_p while keeping θ_{50} at a predefined value, both in steady state and during load and speed transients. There are some significant cycle-to-cycle variation in the system inputs in steady state for some of the experiments, see Figs. 9.21, 9.20, this variation could be decreased by increasing the control-action weights in Eq. (9.13).

The pressure-rise rate $dp_{\max}$ is in this paper treated as a noisy signal whose mean value is to be controlled below a an upper bound, the validity of this treatment could of course be questioned since $dp_{\max}$ levels above the upper bound will occur even if the mean $dp_{\max}$ level is kept below. A more sophisticated design would be to choose the upper bound based on the statistical distribution of $dp_{\max}$ and in this way control the frequency or probability of the $dp_{\max}$ boundary violations, similar to what was presented by [Jones and Frey, 2015].

It is possible that comparable performance could be obtained with a simpler controller structure, for instance by formulating the $dp_{\max}$ boundary problem as a set-point problem as presented in [Ott et al., 2013], this would however demand more ad-hoc logic, and the framework would not be as general and easily expandable if more states and inputs were to be added to the control problem.

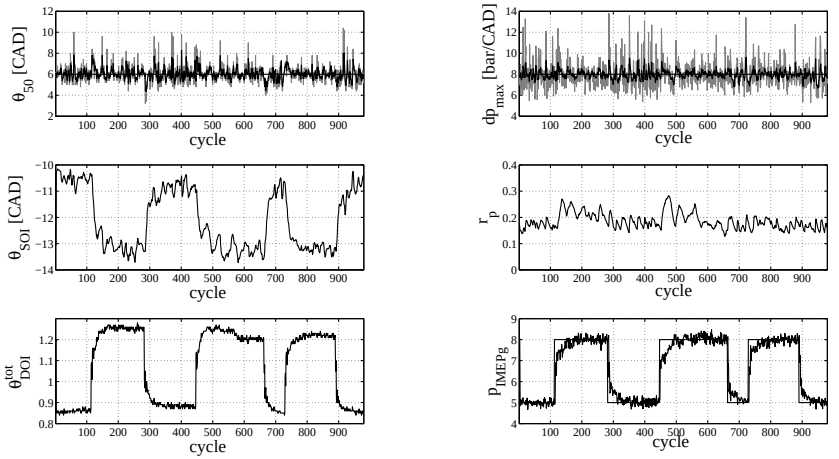

Figure 9.20 Input and output data during p_{IMEPg} set-point changes. The response time for p_{IMEPg} is around 20 cycles, and as $\theta^{\text{tot}}_{\text{DOI}}$ varies, θ^{m}_{SOI} is adjusted in order keep θ_{50} constant, r_p is only doing minor adjustments in order to keep dp_{max} below the upper limit, the variation in r_p indicates that dp_{max} is not so sensitive to changes in $\theta^{\text{tot}}_{\text{DOI}}$ at this operating point. Some input signal oscillations can be observed around cycles 200 and 500.

Future work consists of investigating higher engine loads and the controller compatibility with a gas system controller that sets the engine intake conditions and thus the ignition delay, it would also be interesting to generalize the control problem to incorporate more than two injections, triple-injection strategies has previously been used in PPC [Manente et al., 2010a].

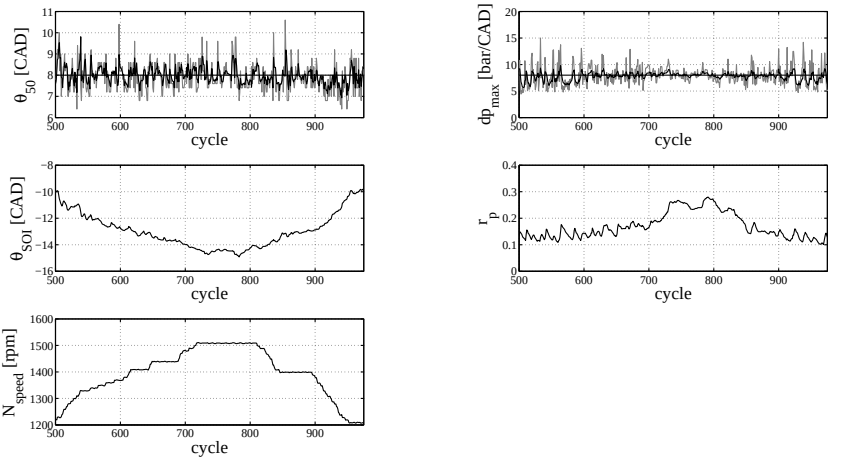

Figure 9.21 Input and output data during N_{speed} set-point changes, r_p has to increase and θ^m_{SOI} advance in order to fulfil the constraint and set-point level when N_{speed} increases. It can also be seen that the $dp_{\max}$ noise level decreases with speed.

10

Conclusions and Future Work

10.1 Conclusions

Pressure-sensor based closed-loop control seems to be a viable solution for PPC feedback control. Pressure-sensor information enables on-line heat-release analysis, an analysis method that could be calibrated online using nonlinear estimation methods as shown in Chapter 5. Heat-release analysis was also shown to be able to predict pressure variations due to injection timing shifts. The ignition-delay response to intake temperature and composition variations could be modelled using simple mathematical models. It was shown to be more difficult to model the relation between the start of combustion and ignition delay close to top-dead center. Ignition delay and combustion phasing could be controlled simultaneously by performing coordinated control action in the gas-exchange system and the fuel-injection system. Pressure-rise rate could be controlled in closed loop by configuring the pilot and main injection fuel distribution where combustion phasing was mainly affected by the main-injection timing which simplified the controller design. In general, MPC was found to be a handy framework for formulating the wanted engine behavior as an optimization problem.

10.2 Future Work

The following list contains possible future work that builds on the material presented in the thesis.

Chapter 5

- Make a deeper analysis of the PF performance w.r.t. particle number and restarting criteria.

- Find more realistic probability-distribution functions for Q_c by studying heat-release analysis data.

Chapter 7

- Include a more detailed gas-system model for additional online optimization of the gas-exchange efficiency.
- Include efficiency and emission levels in the MPC cost function instead of set-point tracking error.
- Compare performance with decentralized-control schemes.

Chapter 8

- A problem with the presented controller was that the convergence point was dependant on unknown heat-transfer model parameters. Evaluation of the controller performance together with the adaptive heat-release-analysis calibration methods in Chapter 5 could therefore be carried out.
- Combine the pressure-prediction method with an ignition-delay model for improved performance.

General

- High-resolution pressure sensors are not implemented on the heavy-duty production engines of today. Cheaper sensor alternatives, for example, ion-current sensors, could be compared to the currently used sensors for PPC closed-loop control.
- This thesis only studies a limited load region of the engine, in order to fully investigate the PPC control problem, this load range have to be broadened to also cover low- and high load operating points and transient operation between the two.

Bibliography

A, B Kempinski, and J. Rife (1981). *Knock in spark ignition engines*. 810147. SAE Technical Paper.

Agrell, F., H.-E. Ångström, B. Eriksson, J. Wikander, and J. Linderyd (2003). *Integrated simulation and engine test of closed loop HCCI control by aid of variable valve timings*. 2003-01-0748. SAE Technical Paper.

Akihama, K., Y. Takatori, K. Inagaki, S. Sasaki, and A. M. Dean (2001). *Mechanism of the smokeless rich diesel combustion by reducing temperature*. 2001-01-0655. SAE Technical Paper.

Amann, C. A. (1985). *Cylinder-pressure measurement and its use in engine research*. 852067. SAE Technical Paper.

Annand, W. et al. (1963). "Heat transfer in the cylinders of reciprocating internal combustion engines". *Proceedings of the Institution of Mechanical Engineers* **177**:1, pp. 973–996.

Bengtsson, J., P. Strandh, R. Johansson, P. Tunestål, and B. Johansson (2004). "Closed-loop combustion control of homogeneous charge compression ignition (HCCI) engine dynamics". *International journal of adaptive control and signal processing* **18**:2, pp. 167–179.

Bengtsson, J., P. Strandh, R. Johansson, P. Tunestål, and B. Johansson (2006a). "Hybrid control of homogeneous charge compression ignition (HCCI) engine dynamics". *International journal of control* **79**:05, pp. 422–448.

Bengtsson, J., P. Strandh, R. Johansson, P. Tunestål, and B. Johansson (2006b). "Model predictive control of homogeneous charge compression ignition (HCCI) engine dynamics". In: *IEEE Int. Conf. on Control Applications, (CCA 2006)*. IEEE. Munich, Germany, pp. 1675–1680.

Bengtsson, J., P. Strandh, R. Johansson, P. Tunestål, and B. Johansson (2006c). *Multi-output control of a heavy duty HCCI engine using variable valve actuation and model predictive control*. 2006-01-0873. SAE Technical Paper.

Bengtsson, J., P. Strandh, R. Johansson, P. Tunestål, and B. Johansson (2007). "Hybrid modelling of homogeneous charge compression ignition (HCCI) engine dynamics—a survey". *International journal of control* **80**:11, pp. 1814–1847.

Blom, D., M. Karlsson, K. Ekholm, P. Tunestål, and R. Johansson (2008). *HCCI engine modeling and control using conservation principles*. 2008-01-0789. SAE Technical Paper.

Brunt, M. F. and C. R. Pond (1997). *Evaluation of techniques for absolute cylinder pressure correction*. 970036. SAE Technical Paper.

Casella, G. and R. L. Berger (2002). *Statistical inference*. Vol. 2. Duxbury Pacific Grove, CA: Duxbury.

Chmela, F. G., G. H. Pirker, and A. Wimmer (2007). "Zero-dimensional ROHR simulation for DI diesel engines–a generic approach". *Energy Conversion and Management* **48**:11, pp. 2942–2950.

Cho, E. G., K. A. Thoney, T. J. Hodgson, and R. E. King (2003). "Supply chain planning: rolling horizon scheduling of multi-factory supply chains". *Proc. 35th Conf. Winter Simulation: Driving Innovation, New Orleans, Louisiana, USA, December 7-10*, 1409–1416.

Coleman, T. F. and Y. Li (1996). "An interior trust region approach for nonlinear minimization subject to bounds". *SIAM Journal on optimization* **6**:2, pp. 418–445.

Commission, E.-E. et al. (2009). "Regulation (EC) no 443/2009 of the European and of the council". *Official Journal of the European Union* **140**.

Dawid, H. (2005). "Long horizon versus short horizon planning in dynamic optimization problems with incomplete information". *Economic Theory* **25**:3, pp. 575–597.

Douaud, A. and P Eyzat (1978). *Four-octane-number method for predicting the anti-knock behavior of fuels and engines*. 780080.

Eichmeier, J., U. Wagner, and U. Spicher (2012). "Controlling gasoline low temperature combustion by diesel micro pilot injection". *Journal of Engineering for Gas Turbines and Power* **134**:7, p. 072802.

Ekholm, K., M. Karlsson, P. Tunestål, R. Johansson, B. Johansson, and P. Strandh (2008). "Ethanol-diesel fumigation in a multi-cylinder engine". *SAE Int. J. Fuels Lubr.* **1**, pp. 26–36.

Epping, K., S. Aceves, R. Bechtold, and J. E. Dec (2002). *The potential of HCCI combustion for high efficiency and low emissions*. 2002-01-1923. SAE Technical Paper.

Eriksson, L. (1998). *Requirements for and a systematic method for identifying heat-release model parameters*. 980626. SAE Technical Paper.

Eriksson, L. and L. Nielsen (2014). *Modeling and control of engines and drivelines*. John Wiley & Sons, Chichester, West Sussex, United Kingdom.

EU (2007). “Cleaner trucks and buses: tighter limits for nitrogen oxides and particulate matter (Euro VI).” *Press release, IP/07/1989*.

Fridriksson, H., B. Sundén, S. Hajireza, and M. Tuner (2011). *CFD Investigation of Heat Transfer in a Diesel Engine with Diesel and PPC Combustion Modes*. 2011-01-1838. SAE Technical Paper.

Gatowski, J., E. N. Balles, K. Chun, F. Nelson, J. Ekchian, and J. B. Heywood (1984). *Heat release analysis of engine pressure data*. 841359. SAE Technical Paper.

Geisser, S. (1993). *Predictive inference*. Chapman & Hall, New York.

Gordon, N. J., D. J. Salmond, and A. F. Smith (1993). “Novel approach to nonlinear/non-gaussian Bayesian state estimation”. In: *IEE Proceedings F (Radar and Signal Processing)*. Vol. 140. 2. IET, pp. 107–113.

Guzzella, L. and C. Onder (2009). *Introduction to modeling and control of internal combustion engine systems*. Springer-Verlag, Berlin.

Haagen-Smit, A. (1952). “Chemistry and physiology of Los Angeles smog”. *Industrial & Engineering Chemistry* **44**:6, pp. 1342–1346.

Halstead, M., L. Kirsch, A Prothero, and C. Quinn (1975). “A mathematical model for hydrocarbon autoignition at high pressures”. In: *Proceedings of the Royal Society of London A: Mathematical, Physical and Engineering Sciences*. Vol. 346. 1647. The Royal Society, pp. 515–538.

Halstead, M., L. Kirsch, and C. Quinn (1977). “The autoignition of hydrocarbon fuels at high temperatures and pressures—fitting of a mathematical model”. *Combustion and flame* **30**, pp. 45–60.

Haraldsson, G., P. Tunestål, B. Johansson, and J. Hyvönen (2002). *HCCI combustion phasing in a multi cylinder engine using variable compression ratio*. 2002-01-2858. SAE Technical Paper.

Hasegawa, R. and H. Yanagihara (2003). *HCCI Combustion in DI Diesel Engine*. 2003-01-0745. SAE Technical Paper.

Hellstrom, E., D. Lee, L. Jiang, A. G. Stefanopoulou, and H. Yilmaz (2013). “On-board calibration of spark timing by extremum seeking for flex-fuel engines”. *Control Systems Technology, IEEE Transactions on* **21**:6, pp. 2273–2279.

Heywood, J. B. (1988). *Internal combustion engine fundamentals*. Vol. 930. Mcgraw-hill, New York.

Hildingsson, L., G. Kalghatgi, N. Tait, B. Johansson, and A. Harrison (2009). *Fuel octane effects in the partially premixed combustion regime in compression ignition engines*. 2009-01-2648. SAE Technical Paper.

Hohenberg, G. F. (1979). *Advanced approaches for heat transfer calculations*. 790825. SAE Technical Paper.

IPCC (2007). “Climate change 2014, synthesis report”. *IPCC Fifth Assessment Report*.

Johansson, B. (2006). *Förbränningsmotorer*. Institutionen för värme-och kraftteknik, Lunds Tekniska Högskola, Lund, Sweden.

Johansson, R (1993). *System modeling and identification*. Prentice Hall, Englewood Cliffs, NJ, USA.

Jones, J. C. P. and J. Frey (2015). "Threshold optimization and performance evaluation of a classical knock controller". *SAE Int. J. Engines* **8**, pp. 1021–1028.

Julier, S. J. and J. K. Uhlmann (2004). "Unscented filtering and nonlinear estimation". *Proceedings of the IEEE* **92**:3, pp. 401–422.

Kalman, R. (1959). "On the general theory of control systems". *IRE Transactions on Automatic Control* **4**:3, pp. 110–110.

Kalman, R. E. (1960). "A new approach to linear filtering and prediction problems". *Journal of Fluids Engineering* **82**:1, pp. 35–45.

Karlsson, M., K. Ekholm, P. Strandh, R. Johansson, and P. Tunestål (2008). "LQG control for minimization of emissions in a diesel engine". In: *Control Applications, 2008. CCA 2008. IEEE International Conference on*. IEEE. San Antonio, Texas, pp. 245–250.

Karlsson, M., K. Ekholm, P. Strandh, R. Johansson, and P. Tunestal (2010). "Multiple-input multiple-output model predictive control of a diesel engine". *Advances in Automotive Control*, pp. 131–136.

Kiencke, U and L Nielsen (2000). *Automotive Control Systems. For Engine, Driveline, and Vehicle*. Springer-Verlag, Berlin.

Killingsworth, N. J., S. M. Aceves, D. L. Flowers, F. Espinosa-Loza, and M. Krstić (2009). "Hcci engine combustion-timing control: optimizing gains and fuel consumption via extremum seeking". *Control Systems Technology, IEEE Transactions on* **17**:6, pp. 1350–1361.

Kimura, S., O. Aoki, H. Ogawa, S. Muranaka, and Y. Enomoto (1999). *New combustion concept for ultra-clean and high-efficiency small DI diesel engines*. 1999-01-3681.

Klein, M. and L. Eriksson (2004). *A specific heat ratio model for single-zone heat release models*. 2004-01-1464. SAE Technical Paper.

Klein, M. (2007). *Single-zone cylinder pressure modeling and estimation for heat release analysis of SI engines*. Dissertation No. 1124, Department of Electrical Engineering. PhD thesis. Linköping University, Linköping, Sweden.

Kokjohn, S. L., R. M. Hanson, D. A. Splitter, and R. D. Reitz (2009). *Experiments and modeling of dual-fuel HCCI and PCCI combustion using in-cylinder fuel blending*. 2009-01-2647. SAE Technical Paper.

Lee, H., Y. Park, S. Hong, M. Lee, and M. Sunwoo (2013). *EGR Rate Estimation for Cylinder Air Charge in a Turbocharged Diesel Engine using an Adaptive Observer*. 2013-01-0246. SAE Technical Paper.

Lewander, M., B. Johansson, P. Tunestål, N Keeler, N Milovanovic, and P Bergstrand (2008). "Closed loop control of a partially premixed combustion engine using model predictive control strategies". In: *Proceedings of AVEC*. Vol. 8. Kobe, Japan.

Lewander, M., A. Widd, B. Johansson, and P. Tunestal (2012). "Steady state fuel consumption optimization through feedback control of estimated cylinder individual efficiency". In: IEEE. American Control Conference (ACC 2012, Fairmont Queen Elizabeth, Montréal, Canada, pp. 4210–4214.

Lu, T. and C. K. Law (2009). "Toward accommodating realistic fuel chemistry in large-scale computations". *Progress in Energy and Combustion Science* **35**:2, pp. 192–215.

Maciejowski, J. M. (2002). *Predictive control: with constraints*. Pearson education, Essex, England.

MacMillan, D, A La Rocca, P. Shayler, T Morris, M Murphy, and I Pegg (2009). "Investigating the effects of multiple injections on stability at cold idle for DI diesel engines". *SAE International Journal of Engines* 2009-01-0612.

Manente, V., A. Vressner, P. Tunestal, and B. Johansson (2008). *Validation of a Self Tuning Gross Heat Release Algorithm*. 2008-01-1672. SAE Technical Paper.

Manente, V., B. Johansson, and P. Tunestal (2009). *Partially Premixed Combustion at High Load using Gasoline and Ethanol, a Comparison with Diesel*. 2009-01-0944. SAE Technical Paper.

Manente, V., C.-G. Zander, B. Johansson, P. Tunestal, and W. Cannella (2010a). *An advanced internal combustion engine concept for low emissions and high efficiency from idle to max load using gasoline partially premixed combustion*. 2010-01-2198.

Manente, V., B. Johansson, and P. Tunestål (2010b). "Characterization of partially premixed combustion with ethanol: EGR sweeps, low and maximum loads". eng. *Journal of Engineering for Gas Turbines and Power-Transactions of the ASME* **132**:8.

Manente, V., P. Tunestal, B. Johansson, and W. J. Cannella (2010c). *Effects of ethanol and different type of gasoline fuels on partially premixed combustion from low to high load*. SAE Technical Paper.

Meyer, J. (2011). *Calibration reduction in internal combustion engine fueling control: modeling, estimation and stability robustness*. (Electronic Thesis or Dissertation). Retrieved from https://etd.ohiolink.edu/, The Ohio State University.

Musculus, M. P. (2006). *Multiple simultaneous optical diagnostic imaging of early-injection low-temperature combustion in a heavy-duty diesel engine*. 2006-01-0079. SAE Technical Paper.

Nakayama, S., T. Ibuki, H. Hosaki, and H. Tominaga (2008). *An application of model based combustion control to transient cycle-by-cycle diesel combustion*. 2008-01-1311. SAE Technical Paper.

Olsson, J.-O., P. Tunestål, G. Haraldsson, and B. Johansson (2001). "A turbocharged dual-fuel HCCI engine". *SAE Special Publications* **2001**:1627.

Olsson, J.-O., P. Tunestål, B. Johansson, S. Fiveland, R. Agama, M. Willi, and D. N. Assanis (2002). *Compression ratio influence on maximum load of a natural gas fueled HCCI engine*. 2002-01-0111. SAE Technical Paper.

Olsson, J.-O., P. Tunestål, and B. Johansson (2004). *Boosting for high load HCCI*. 2004-01-0940. SAE Technical Paper.

Osuka, I., M. Nishimura, Y. Tanaka, and M. Miyaki (1994). *Benefits of new fuel injection system technology on cold startability of diesel engines-improvement of cold startability and white smoke reduction by means of multi injection with common rail fuel system ECD-U2*. 940586. SAE Technical Paper.

Ott, T., F. Zurbriggen, C. H. Onder, and L. Guzzella (2013). "Cylinder individual feedback control of combustion in a dual fuel engine". In: *Advances in Automotive Control*. Vol. 7. 1. Tokyo, Japan, pp. 600–605.

Randolph, A. L. (1990). *Methods of processing cylinder-pressure transducer signals to maximize data accuracy*. 900170. SAE Technical Paper.

Rasmussen, C. E. (2006). *Gaussian processes for machine learning*. MIT Press, Cambridge, Massachusetts, USA.

Rassweiler, G. M. and L. Withrow (1938). *Motion pictures of engine flames correlated with pressure cards*. 380139. SAE Technical Paper.

Roelle, M. J., N. Ravi, A. F. Jungkunz, and J. C. Gerdes (2006). "A dynamic model of recompression hcci combustion including cylinder wall temperature". In: *Proc. IMECE*. Chicago, Illinois, USA, pp. 415–424.

Sellnau, M. C., F. A. Matekunas, P. A. Battiston, C.-F. Chang, and D. R. Lancaster (2000). *Cylinder-pressure-based engine control using pressure-ratio-management and low-cost non-intrusive cylinder pressure sensors*. 2000-01-0932. SAE Technical paper.

Shaver, G. M., J. C. Gerdes, and M. Roelle (2004). "Physics-based closed-loop control of phasing, peak pressure and work output in HCCI engines utilizing variable valve actuation". In: *American Control Conference, 2004. Proceedings of the 2004, Boston, MA, USA, June 30-July 2*. Vol. 1. IEEE, pp. 150–155.

Solsjö, R. (2014). *Large Eddy Simulation of Turbulent Combustion in PPC and Diesel Engines*. Department of Energy Sciences. PhD thesis. Lund University, Lund, Sweden.

Sperling, D. and D. Gordon (2009). *Two billion cars: driving toward sustainability*. Oxford University Press, New York.

Stas, M. J. (1996). *Thermodynamic determination of TDC in piston combustion engines*. 960610. SAE Technical Paper.

Takeda, Y. and N. Keiichi (1996). *Emission characteristics of premixed lean diesel combustion with extremely early staged fuel injection*. 961163. SAE Technical Paper.

Tanov, S., R. Collin, B. Johansson, and M. Tuner (2014). "Combustion stratification with partially premixed combustion, PPC, using NVO and split injection in a LD-diesel engine". *SAE International Journal of Engines* **7**:2014-01-2677, pp. 1911–1919.

Tsurushima, T., E. Kunishima, Y. Asaumi, Y. Aoyagi, and Y. Enomoto (2002). *The effect of knock on heat loss in homogeneous charge compression ignition engines*. 2002-01-0108. SAE Technical Paper.

Tunestål, P. (2011). "TDC offset estimation from motored cylinder pressure data based on heat release shaping". *Oil & Gas Science and Technology–Revue d'IFP Energies nouvelles* **66**:4, pp. 705–716.

Tunestål, P., J. K. Hedrick, and R. Johansson (2001). "Model-based estimation of cylinder pressure sensor offset using least-squares methods". In: *Proceedings of the 40th IEEE Conference on Decision and Control*. Vol. 4. IEEE. Orlando, Florida, USA, pp. 3740–3745.

Turns, S. R. et al. (1996). *An introduction to combustion*. Vol. 287. McGraw-hill, New York.

Wang, Y. and S. Boyd (2010). "Fast model predictive control using online optimization". *Control Systems Technology, IEEE Transactions on* **18**:2, pp. 267–278.

Westbrook, C. K. and F. L. Dryer (1981). "Simplified reaction mechanisms for the oxidation of hydrocarbon fuels in flames". *Combustion science and technology* **27**:1-2, pp. 31–43.

Widd, A., P. Tunestål, and R. Johansson (2008). "Physical modeling and control of homogeneous charge compression ignition HCCI engines". In: *Proceedings of the 47th IEEE Conference on Decision and Control*, pp. 5615–5620.

Widd, A., K. Ekholm, P. Tunestal, and R. Johansson (2009). "Experimental evaluation of predictive combustion phasing control in an HCCI engine using fast thermal management and VVA". In: *Control Applications, (CCA) & Intelligent Control, (ISIC)*. IEEE. Saint Petersburg, pp. 334–339.

Widd, A., K. Ekholm, P. Tunestål, and R. Johansson (2012). "Physics-based model predictive control of HCCI combustion phasing using fast thermal management and VVA". *Control Systems Technology, IEEE Transactions on* **20**:3, pp. 688–699.

Willems, F., E. Doosje, F. Engels, and X. Seykens (2010). *Cylinder pressure-based control in heavy-duty EGR diesel engines using a virtual heat release and emission sensor*. 2010-01-0564. SAE Technical Paper.

Woshni, G (1967). *A Universally Applicable Equation for the Instantaneous Heat Transfer Coefficient in the Internal Combustion Engine*. 670931. SAE Technical Paper.